Experimental analysis of a kite system's dynamics

Author:
Arthur ROULLIER

Supervisor:
Dr. Peter OTT
Dr. Roland SCHMEHL

A thesis submitted in fulfillment of the requirements for the degree of Master

March 13, 2020

Acknowledgements

I would like to thank both of my supervisors, Dr. Peter Ott and Dr. Schmehl as well as Mark Schelblergen for their guidance and support and Kitepower for providing me with experimental data.

Contents

List of Figures

List of Tables

List of Abbreviations

β, θ	Elevation angles
ϕ	Azimuth angle
ϕ_Y	Yaw angle of the wing
θ_P	Pitch angle of the wing
ψ_R	Roll angle of the wing
θ_R, θ_L	Right or left roll angles in KCU inertial model
α, AOA	angle of attack of the wing
Θ	Vector of forces for the system identification of aerodynamic parameters
Φ	Matrix of speeds for the system identification of aerodynamic parameters
KCU	Kite control unit
IMU	Inertial measurement unit
EG	Earth ground reference frame
L	Local reference frame
B	Body reference frame
W	Wing reference frame
C_L	Lift coefficient
C_D	Drag coefficient
$\mathbf{F}_a$	Aerodynamic force
$\mathbf{F}_t$	Tether force
$A_{k,t}$	top projected surface area of the wing
$A_{k,s}$	side projected surface area of the wing
h_k	height of the wing
w_k	width of the wing
J_k	Inertial tensor of the wing
D_T	Tether diameter
$C_{D,T}$	Tether drag coefficient
ρ_T	Tether density
$\mathbf{r}$	Kite's position
$\mathbf{b}_T$	Vector for the estimation of the tension in discrete tether model
$\mathbf{A}_T$	Matrix for the estimation of the tension in discrete tether model
$\mathbf{S}_T$	State vector of the discrete tether model

Chapter 1

Introduction to AWE

The need for the expansion of renewable energy is a known fact, and wind is one of them. This introduction aims at giving an insight on why airborne wind energy are a relevant option and the various approach taken to extract energy from the wind with airborne systems.

1.1 Wind Energy

Knowing the amount of energy available to a system for energy production is key to understand the opportunities of such an energy and draw predictions about the energy production.

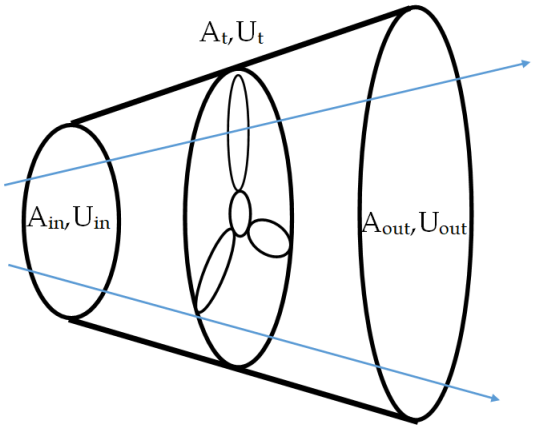

FIGURE 1.1: Betz's hypothesis of expansion of a stream through a wind turbine

The wind energy production is based on a simple principle: the transformation of the kinetic energy withheld by the wind into electrical energy. The amount of kinetic energy contained by the wind can be estimated by computing the kinetic energy flux going through a control surface A. Since the power of the stream scales like $\frac{1}{2}\dot{m}v_w^2$ with $\dot{m} = \rho A v_w$ the mass flow rate, the wind power can be written [24]:

$$P_{wind} = \frac{1}{2}\rho A v_w^3 \tag{1.1}$$

where P_{wind} stands for the available power in the stream, ρ is the density of the air, A is the control surface through which the wind blows, and v_w is the wind velocity. Unfortunately all this energy is not available for power extraction. The momentum theory provides us with a theoretical upper bound for the amount of energy that can be extracted from a wind stream and is known as the

Betz limit. The reasoning Albert Betz adopted in 1919, was the following: supposing that the stream expands through a wind turbine as in Figure:1.1, applying the mass conservation equation to the system: $\dot{m} = \rho A(U_in + U_out)/2$ and Bernoulli's equation along a streamline to find the power extracted by the wind turbine: $P_{turbine} = \frac{1}{2}\dot{m}(U_{in}^2 - U_{out}^2)$ gives the efficiency of the wind turbine:

$$\eta = \frac{P_{turbine}}{P_{wind}} = \frac{1}{2}(1 - \frac{U_{out}^2}{U_{in}^2})(1 + \frac{U_{out}}{U_{in}}) \tag{1.2}$$

After differentiating this equation with respect to $\frac{U_{out}}{U_{in}}$ and equalizing it to zero the maximum value of the efficiency is found and is equal to 59.3% and is known as Betz's limit for power extraction. Therefore the

1.2 AWE Energy

One way to capture the available energy is by using tethered wing devices to convert it to electricity. The ideas are not missing, some concepts combine onboard wind turbines and transmit the electrical energy through the tether, while others convert the pulling power of the flying devices on the ground as shown in figure 1.2. Using a light weight tether instead of a conventional tower for wind turbines and in some cases kite wings instead of rigid wings reduces the material consumption and allows for the adjustment of the location and of height of harvesting. Indeed for some concepts the ground station can be moved to better environment to optimize the energy production. This technology offers then lower installation cost and an increase in capacity factor which is full of promises since it has the potential of cutting the cost of wind energy. This technology presents itself as a real opportunity in the actual context when considering "square cube law". This law states that as a wind turbine rotor increases in size, its energy output increases as the area swept by the rotor so he square of the diameter, while the cost of material increases as the cube of the diameter. Therefore an increase in wind turbine size will at some point not result in an economical benefit. Even if AWE system still have to catch up in terms of nominal production with the state of the art wind turbine, they offer a serious alternative to wind turbine.

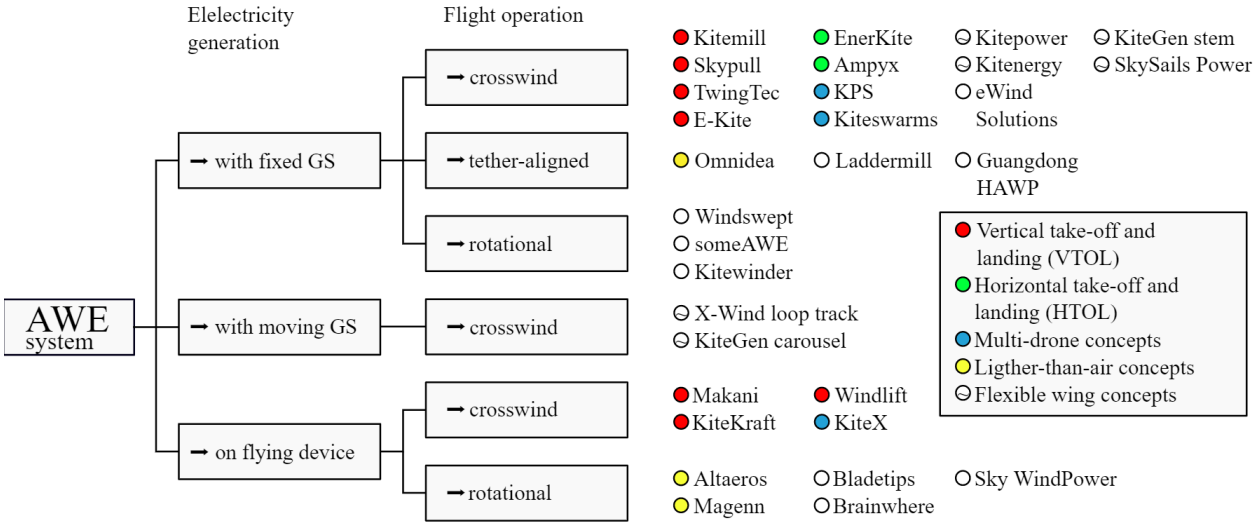

FIGURE 1.2: Airborne wind energy classification

For the crosswind kite, Loyd computes the maximum harvesting factor as:

$$\zeta_{\text{opt}} = \frac{4}{27}\frac{C_{\text{L}}^3}{C_{\text{D}}^2} \tag{1.3}$$

Therefore to quantify the performance of a system information about its aerodynamic performance is necessary. This is one of the aim of this work, which focusing on soft wing kites, will hopefully give some methods to understand the efficiency and draw the efficiency of such systems.

Chapter 2

State of the Art: Dynamic behaviour of kites

This section aims at giving a context and a summary of the main important characteristics of a kite's flight that have been previously discovered and studied and that will prove to be necessary for this thesis and give the right tools for understanding the collected data.

2.1 Existing methods and work on the estimation of aerodynamic parameters

Wind tunnel testing of large deformable soft kites for wind energy conversion is expensive and, in many cases, practically not feasible. Computational simulation of the coupled fluid–structure interaction problem is scientifically challenging and of limited practical use for aerodynamic characterization. Therefore, experimental method for aerodynamic characterization of flexible membrane kites by in situ measurement of the relative flow, while performing figures of eight is needed to have an insight on the aerodynamic characteristic of a wing.
Oehler et al. [20] determined the aerodynamic parameters of the kite by using in situ measurement of the flow with a pitot tube and wind vanes. The model he used for evaluating these coefficients was based on a static approach. What also makes his work stand out is that he distinguishes three different fundamental contributions to the angle of attack:

1. the tether angle of attack.
2. the line angle which characterizes the pitch of the wing relative to the the tether due to the weight and aerodynamic forces acting on each component.
3. the angle sue to a change of the power setting.

It was found that not only does the aerodynamic parameters depend on the angle of attack but also on the steering and power settings. Indeed the author observed that the increasing loading of the wing causes it to flatten and increase the projected area which would amplify the estimated value of lift. He also found that the aerodynamic performance drops during a turn. However his results are limited due to very noisy experimental data and the fact that the kite was flown for a constant tether force. Other authors have gotten around the noise problem and measurement error by developing more complex models for identification and coupling them to a Kalman filter. For example Schmidt et al. [26] adopted such an approach using a dynamic point mass model, but only considering the force balance whilst Borobia et al. [4] also accounted for the moments acting of the kite. Schmidt et al. [26] also introduced a novelty in their Kalman filter, they add in their measurement an orthogonality constraint between the lift force and the apparent wind which is shown to increase the efficiency of the filter. There are also some differences in the measurement process between [4] and [26] which are summarized in table 2.1.

	Oehler et al. [20]	Schmidt et al. [26]	Borobia et al. [4]
Model	Static model with force balance	Static model with force balance	Static model with force and moment balance
Kalman Filter	×	✓ with orthogonality constraint	✓
Meaurements	-Kite position and orientation(IMU) -Tether force -Apparent wind speed measured at the kite (Pitot tube) -Angle of attack (wind vane)	-Kite position, orientation and acceleration -Tether force -Line angles and rates at the ground station -Wind speed and direction at the ground	-Kite position, orientation and acceleration -Tether force -Tension force at every line -Apparent wind speed and angle of attack measured at the kite(Pitot tube) -Heading angle and wind velocity at the ground
Output	Lift and drag coefficients	Lift and drag coefficients	Lift, drag and aerodynamic moments coefficients

TABLE 2.1: Comparison of the different methods implemented for the estimation of the aerodynamic parameters

Another out of the box way of estimating the parameters of the kites' wing was also done by Jann et al. [18], who in his work measured the properties not in a AWE system but in a gliding parachute.

2.2 Turning of kites

How a C shaped soft kite really turns is a question to which an answer has already been looked for. Several attempts have been made with relative success and a short summary and explanation of what is thought to be the most relevant ones for the continuation of this project will be made. The question of how a kite turns can be tackled from different angles. Either through a thorough simulation of the system or through simplified modelling and experimental verification of semi-empirical laws which in the end gives turn rate laws for the kite. These correspond to a high fidelity approach or a black box approach neglecting complex effects after some justifications. Very basic experimental observations with the help of video footage can also lead to some explanations. In this section the link between the kite's deformation and its turning behaviour will be drawn from previous studies. The obtained laws for turning are compared and verified with experimental data of the flight path and the resulting forces. However some doubts still remain if certain major behaviours and explanations have been omitted or if the ones described are entirely valid since there are some contradictions in the literature.

2.2.1 Turn rate law

A simple way to describe the link between the dynamics of the kite and the steering input is through the use of a turn rate law. The turn rate law is in general a semi empirical law verified through experimentations, in a way that the system is modeled with simplifying assumptions and tries to capture the behaviour of the kite with respect to the kite's properties, the flight conditions and the user inputs. Two turn rate that were thought relevant are presented here. The first one is a thorough investigation of the effect of steering on soft kites done by Fagiano et al [19]. The kite system is modelled as a mass point and two main assumptions are made regarding the behaviour of the kite:

1. The velocity and heading vectors of the kite are taken to be colinear, therefore the effective wind projected onto the tangential plane to the wind window at the wing's location is equal to the wing's velocity. Also, as a consequence all the forces in the direction of the velocity vector are negligible as compared to lift and drag.

2. The roll is sufficiently small to linearise its trigonometric functions.

Using both these hypotheses, the author finds the following turn rate law which was verified with experimental data for three different kites:

$$\dot{\gamma} = \frac{C_L \rho A}{2md}(1 + \frac{1}{E_q^2})^2 |\vec{V_a}|\delta + \frac{g \cos\beta \sin\gamma}{|\vec{V_a}|} + sin(\beta)\dot{\phi} \tag{2.1}$$

with $\dot{\gamma}$ the yawing turn rate, C_L the coefficient of the kite, $\rho[kg/m^3]$ the density f the air, $A[m^2]$ the projected surface area of the kite, $m[kg]$ the mass, d the wing span of the kite, $E_{eq} = \frac{L}{D}$ the equivalent aerodynamic efficiency, $\vec{V_a}[m/s]$ the apparent velocity of the kite, $\delta[-]$ the steering input of the kite and finally $g[m/s^2]$

A simpler turn rate law was found by Erhard and Strauch [10] but uses stronger modelling assumptions such as:

1. The influence of the weight can be neglected
2. The effect of the tether and the Kite's inertia are not important
3. Steady state aerodynamic is assumed and the steering deflections can be described by a single parameter
4. The wind field is assumed as constant and homogeneous

Through a model implementing these hypothesis both of the author extract the following turning rate law:

$$\dot{\gamma} = K_{\dot{\gamma}}\delta + M\frac{\cos\beta \sin\phi}{|\vec{V_a}|} \tag{2.2}$$

with $\dot{\gamma}$ the turn rate, $K_{\dot{\gamma}} = g|\vec{V_a}|$ the gain between linking turn rate and deflection , β the elevation angle, ϕ the azimuth angle and δ the deflection which corresponds to the difference of length between the right and the left bridle lines.

2.2.2 A thorough theoretical study of the deformations during turning of kites

The alternative to a steering law to understand how a C shape wing turns is to try to study a realistic model of the system. In a real tour de force, Jeroen Breukels [7] achieved such a feat by modeling the entire structural system of the kite (wing, bridle line and tether) with spring connections using a multibody approach and coupling this structural system to an aerodynamic model built on CFD (Figure:2.1). The result of this thesis is a thorough theoretical explanation of the turning of a kite.

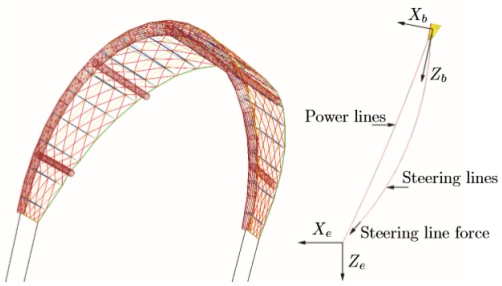

FIGURE 2.1: Multibody model of the kite as found in Breukel's thesis [7]

It was found that when initiating a right turn by tensioning the right steering line an asymmetrical loading of the kite is created which ends up deforming the kite. This deformation causes the right

side of the kite to generate more lift and drag than the left side. Indeed, the deformation not only increases the effective surface area of the right ear with respect to the left ear it also increases the angle of attack of the right side. Both of these changes are responsible for an increase in the aerodynamic forces. The difference in tip surfaces and angles of attack lead to a larger lift force on the right, pulling the kite to the right. However, the difference in the drag between the right and left side are not sufficient to explain why the kite yaws during a turn. The asymmetric loading causes the kite to deform in a distinct manner, the right tip is bent forward and the left tip backward (Figure: 2.2). Because of this skewing the resulting lift and drag component of the right side are shifted forward with respect to the kite's center and end up generating a yawing moment (Figure: 2.3).

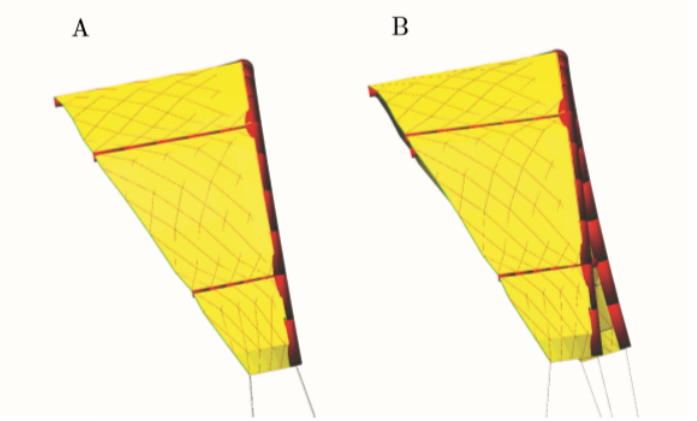

FIGURE 2.2: The deformations of the kite under asymmetrical loading due to a steering input [7]

Therefore, the flexibility of the kite is key in a kite's turning behaviour. As shown by the author a stiffer kite is less prone to fast turning than a soft kite. To increase the steering performance, one should therefore be looking at a more flexible kite. The author also assesses the design parameters which are influencing the kite's turning performance. It was found that since the skewing deformation of the kite's structure is one of the main drives in a kite's turn and that the main forces responsible for turning come from the aerodynamic forces exerted on the tips of the kite, an increase of the surface area of the kite's tip should then not only increase the aerodynamic forces and turning moment but also the moment arm of the applied force on the wing. More rotational forces would then be generated with less input force.

2.2.3 An experimental investigation of the turning of kites

In his thesis Marc van Reijen [22] tried to capture with an experimental setup the deformations of the kite during maneuvers. Three IMUs where placed on the wing, two at the tips and one in the center. The goal was to capture the deformations of the wing tips with respect to the center part of the wing and try to verify and/or complete the findings of Jeoren Breukels. This was partially done as the main pillar of theory of Jeoren Breukels in which the kite skews for yawing was contradicted by the measurements. The author claimed and justified that this was due to a measurement setup

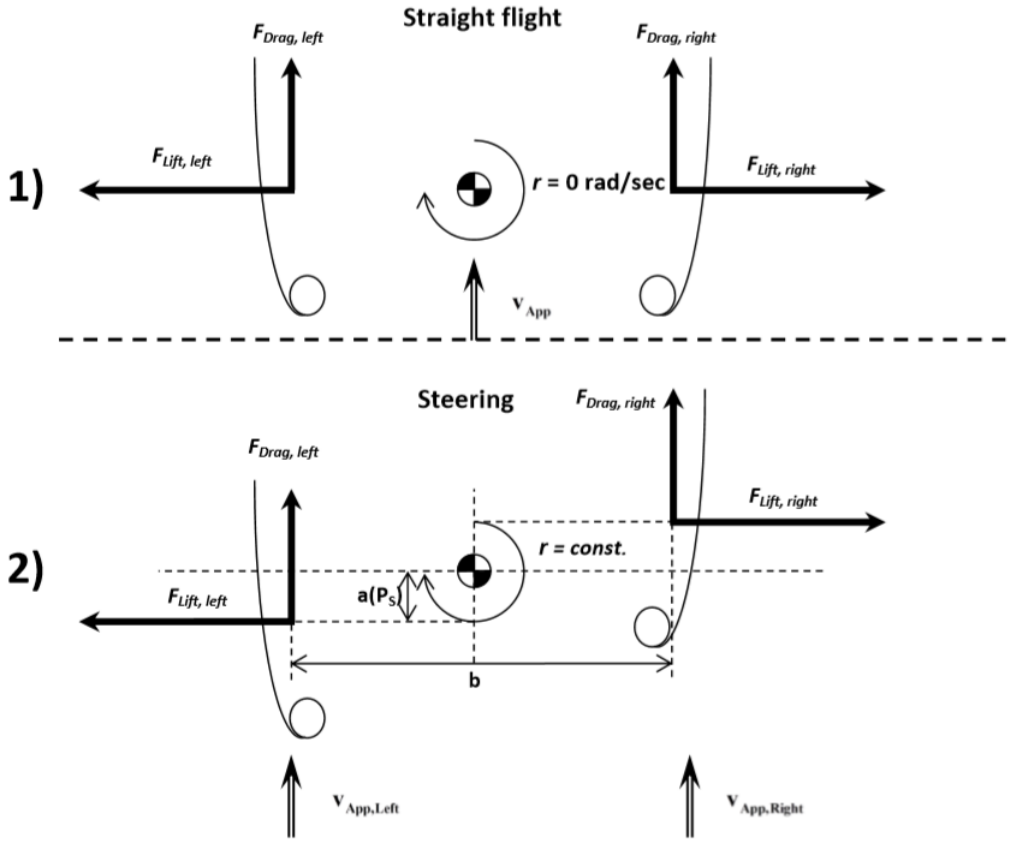

FIGURE 2.3: Shifting of the tips aerodynamic forces due to the skewing deformation of the kite [23]

error. Still, interesting behaviours were found during this thesis. The main one is the "jellyfish" deformation the wing goes periodically through during power and depower phases (Figure:2.4). Indeed when powering up the kite "unrolls itself" and increases the effective area that can produce lift, hence its lift. Therefore the projected surface area changes during powering which creates a problem for comparing different kites as the no dimensionality based on a single projected surface area is no longer valid. However one needs to be careful with such an assumption since it is also highly dependent on how the bridle system and wing are built and transmit the effort. Indeed Another feature of the deformation that was found was uneven modification of the angle of attack span wise: it is greater at the tips than in the middle of the wing as the center is “stiffer” since it is the main supplier of lift forces as it has the largest surface area. The author claims that a this change creates a net centripetal force moving the kite into a circular path, and is then the main reason of why a kite turns. The added lift forces go alongside an increase in drag forces that make the kite turn into the direction of the movement. The roll angle also changes but seems to be a secondary effect due to an increase in lift forces on one side and decrease on the other side.

In [23] the author also drew a thorough inventory of the different yawing moments acting on the kite. The author claims that three main types of moments exist, one due to steering and warping of the kite, another one due to gravity and causing side slip and the last one is a damping moment which opposes itself to the yawing motion of the kite.

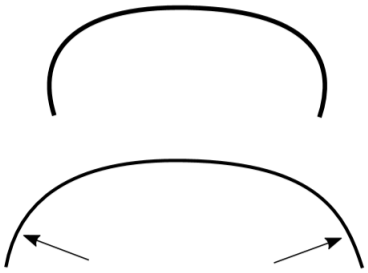

FIGURE 2.4: Unrolling deformation of the kite during power and depower phases [23]

2.3 Tether and KCU effects

Nedeleg et al. [3] derived a three-dimensional analytical model for the tether deformation due to gravity and aerodynamic loading. The effect of the wind velocity gradient was considered for the tether as well as for the kite aerodynamics. The main idea in this paper was to develop a method for determining a low wind speed limit for kite flight. This method allowed for a comparative study between the influence of tether design, in terms of length and mass per unit length, and kite design, in terms of lift-to-drag ratio angle, lift coefficient and mass. However, it only considers static flights and the interpretation of the results for crosswind flights are hence limited. Argatov et al. [1], Houska et al. Houska and Fagiano [19] all considered a straight rod tether model, but the difference between all of these models lies in the model of the drag coefficient and whether they consider only normal wind velocity or also tangential wind velocity for the drag efforts. A model considering the tether as a straight elastic spring to account for material stiffness has been used to study the stability of the kite during a dynamic flight by Terink et al. [27]. Argatov et al. [1] also accounted for tether sag due to wind load and gravity, if the tension along the tether is constant. They proposed a method to calculate wind load by neglecting the tangential wind component relatively to the line and showed how tether effects decrease the power production for a dynamic flight.

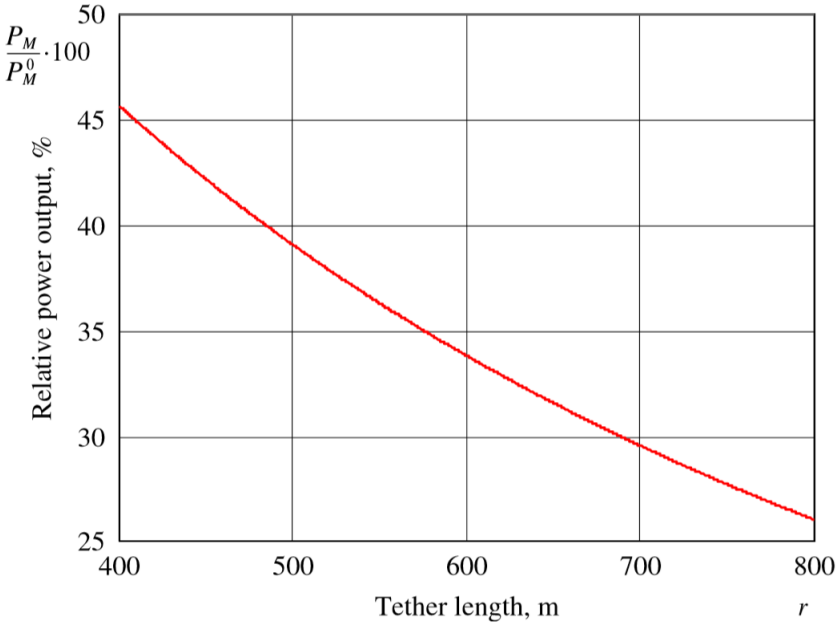

FIGURE 2.5: Tether losses function of tether length [1]

They also considered the influence of the tether sag on the kite angle of attack. They found out that since higher wind speeds lead to higher tether tensions, the tether sag angle did not substantially depend on the wind speed. The author admitted that the use of a straight line tether model in evaluating the equivalent air resistance was a simplification of the true geometry, but it would only cause small error because in the kite's crosswind motion, only the upper part of the tether contributes to the equivalent tether drag. Discrete tether models were also developed but mainly as part of an entire kite system's model. For example [13] developed a discrete tether, in which he divides the tether in elastically damped rods to account for the length variation and to compute the tension easily. A similar model was developed by [8]. However this model might be unstable and shows some oscillations [29]. Williams et al. [29] tried to overcome this problem by developing a so-called lumped mass model for dynamic flight. The mass of each element is concentrated on each node and the distance between each node remains constant. The variation in length due to reel in and reel out was implemented by adding or retrieving elements.
The studied system has its on particularity, indeed the KCU ads a suspended weight to the entire system and its effect on the kite's flights was shortly studied and still asks for explanation and verification with flight data as its influence is not entirely understood. An early identification of the outward swing of the KCU is noticeable in [12] as shown in figure 2.6. However the author was not entirely sure about this effect, since the wide angle of the camera that was used could influence the interpretation.

FIGURE 2.6: Illustration of a KCU's shift

The effect of the KCU on a kite's flight was also studied theoretically by Xander Gerrman [14]. The author implemented both Fechner and Ruppert's models to study the effects. However no experimental study was done on this subject.

2.4 Research Objectives

The literature review brought up several questions to which this work will try to provide an answer. First of all very little data relating the efforts applying on the kite and how they scale with respect to each other were found hence the first research question:

From the experimental data, how do the different efforts applying on the kite scale with respect to each other?

The effect of the KCU has been noticed and studied theoretically through simulation so experimental confirmation of this effect is needed, hence:

What is the effect of the KCU on the kite's system dynamic behaviour and performance?

Then it was shown that to quantify the performance of a kite one needs to have access to aerodynamic coefficients. It was thought of interest to also study the effect of powering and depowering of the kite as well as turn on the performance of the kite. A more complex model than Oehler's model relating these effect will have to be drawn:

How does the identification of aerodynamic parameter change with the degree of complexity of a model? How does the result compare to CFD? What is the measurable impact of turning and power setting on the performance of the kite?

Finally during the literature review there was no real measurable way to know how the tether behaves during crosswind flights, and how models with different degrees of complexity behave with respect to one another. Therefore when making for example the hypothesis of a straight tether there is a lack of information on how much error is made or how different the results will be. It is also difficult to directly measure the deformation of the tether since measurement system will create disturbances. Therefore this work will attempt to give an answer to the following questions:

What are the dynamic characteristic of a tether during figures of eight manoeuvres? How does the model influence this behaviour? How does it affect the evaluation of the aerodynamic parameters?

In the end this project will also try to use the experimental data to give a certain hindsight on which hypothesis are valid and which are not with respect to real system, when building a model of the kite system.

Chapter 3

Model development

This chapter is aimed at capturing the system's behaviour and get some knowledge about it. The goal is to get a crucial understanding of the kite's flight properties and try to see if it is possible to roughly get a glimpse of the kite's deformation through an indirect method by carefully selecting aerodynamic models and its parameters. The entire system will be broken down into modelling blocks. These blocks will include different tether models, aerodynamic models with increasing complexity and all resulting models will be linked by a constrained rigid body model. The final idea hidden behind the creation of this model is to then use it for system identification of the aerodynamic parameters with real experimental data. The goal is to get an analytical model as close as possible to experimental data and the real system and also try to draw conclusions on the aerodynamic and flight behaviour of the kite from the extracted parameters. An analytical approach was chosen since it is based on the governing equations of motion and has therefore limited degrees of freedom (in the order of 10^1) making it less complex for system identification. This is a compromise with respect to numerical models which are more precise but more expensive computationally.

3.1 System's description

This section shall give an overview over the various components that are used in the current system setup. In principle, an ordinary kite used in kite surfing is attached via one strong cable (hereafter referred to as tether) to a ground-fixed winch. An electrical motor is attached to the winch, providing both the ability to wind up the tether and unwind it in the power generation phase.

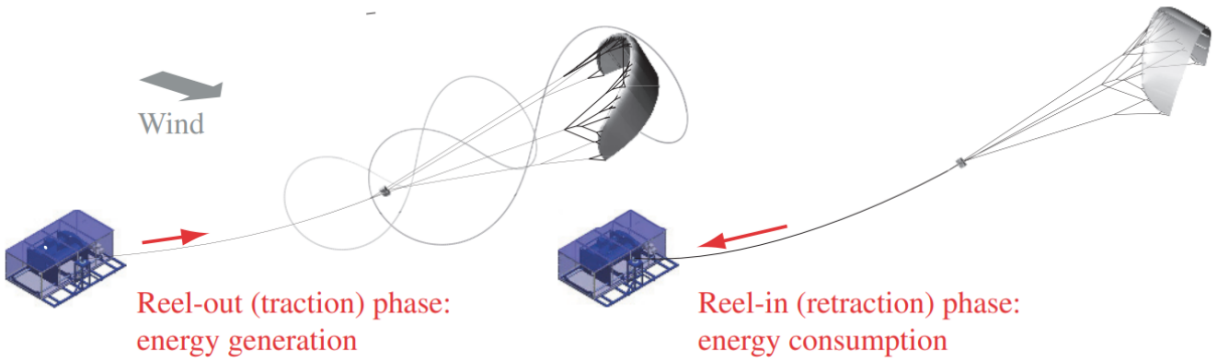

FIGURE 3.1: Illustration of the system [28]

As shown in 3.1, the angle of attack is maximised during reel out phases and the kite flies crosswind figures of eight to extract the maximum amount energy from the wind. At the end

of the production cycle the kite must be brought down by hauling it down with the winch at the ground station. To minimise the energy needed the kite is depowered by reducing the angle of attack and the crosswind flights are stopped. Both of these phases are called pumping cycles.

3.1.0.1 System Layout

3.1.0.1.1 Wing The wings used are mostly directly derived from ordinary kite surfing kite wings. For the experimental set-up a Leading Edge Inflatable wing (LEI) is used. The leading edge beam an strats are inflated using pressurized air to give the wing its shape and rigidity. The kite used here was one of kite power's V3.B (2012 design) with its main physical properties summarized in 3.1

TABLE 3.1: Wing's properties

Property	***Value***	Description
m_k	12 [kg]	Kite's mass
$A_{k,t}$	19.75 $[m^2]$	Projected area of the kite on the xy-plane
$A_{k,s}$	5.65 $[m^2]$	Projected area of the kite on the xz-plane
h_k	2.8 $[m]$	Height of the kite
w_k	8.3 $[m]$	Width of the kite

FIGURE 3.2: Airborne LEI kite with KCU [25]

3.1.0.1.2 Kite Control Unit (KCU) and bridle system A surfing kite is usually controlled using a handle bar from which steering lines are attached to both sides and lead up to the tips of the kite. This enables the surfer to control both the angle of attack (by moving the handle straight down, pulling down both wingtips symmetrically) and to steer the kite in a certain direction (by tilting the bar and thus applying an unsymmetrical load to the wingtips). Pulling down the right

wingtip (i.e. lowering the right side of the bar) will result in a right-turn of surfer and kite. The same technique is adopted and implemented in the control pod or KCU and is attached between the bridle line system and the tether 3.3 . The control pod contains two motors one for steering the kite and one for controlling the power setting. Only one winch is connected to the power motor which when winded up applies a symmetrical load to the wingtips, leading to an increase in the angle of attack. One winch controls both the end of of the steering line, so that a revolution of the steering motor releases one end, while pulling on the other, resulting in an asymmetric wingtip load and so a turn. One of the singularity of Kitepower's setup is that the KCU is not kept at the ground station but is carried around by the wing. This has some effects as the KCU adds additional drag, weight and inertia. However is brings several benefits compared to a control station kept on the ground. Indeed the steering lines will add some extra drag and their flexibility and sagging will result in longer signal travelling time which will harm the system's response time and control performance. Also having the KCU on board of the kite gets rid of the complexity of reeling in and out the steering lines.

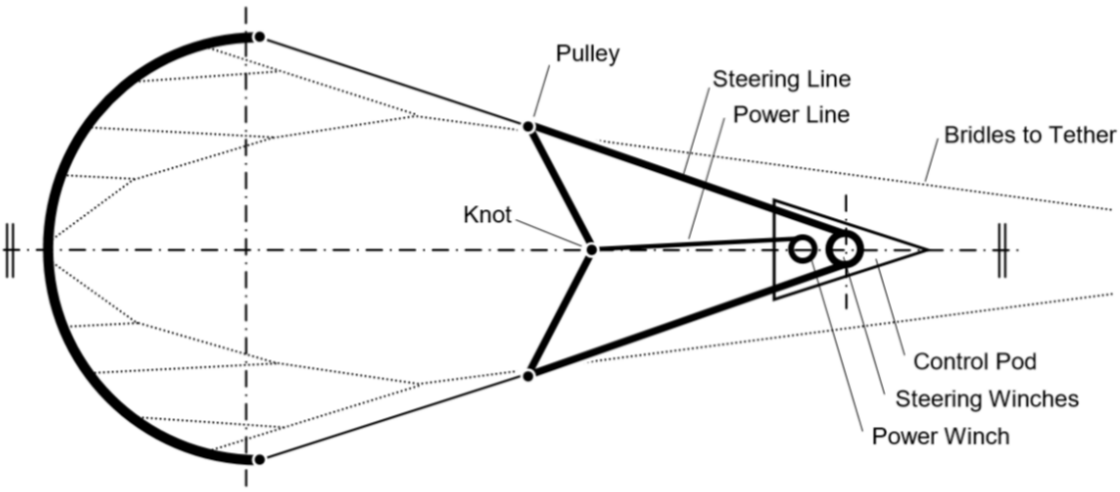

FIGURE 3.3: Bridle line illustration

3.1.0.1.3 Ground station The ground station contains the winch and the generator as well as an antenna fro transmitting the data from the KCU.

3.2 Reference frame definition

3.2.1 Frame definition

The relative complex kinematic movement of the whole kite system calls for the definition of several reference frames. The description of the motion of the kite should not only capture the complex trajectory followed by the kite's center of gravity, but it should also account for the kite's rolling, pitching and yawing behaviour around its main axis as well as for the apparent wind orientation with respect to the kite, meaning that the apparent wind is not directly facing the kite but is shifted with an angle of attack α and a side-slip angle β with respect to the kite's direction. Therefore four different reference frames will be defined and used across this work. As a side note, the

reference frames in this work for a matter of consistency will always have an East-North-Up orientation (notation: ENU). The four reference frame enlisted as follow are represented in Figure: 3.4.

1. The first reference frame defined is the earth ground reference frame (EG), which is by its name the reference frame in which and observer would watch the kite fly. The origin of this reference frame will be taken as the ground station. It figures in black in Figure: 3.4.

2. The second reference frame is the local reference frame (L) or small earth reference frame, and is defined as the reference frame in spherical coordinate attached to the tether's end. It figures in red in Figure: 3.4.

3. The second to last reference frame is the body reference frame (B) which goes a step further than the local reference frame because it takes into account the orientation of the kite (pitch, yaw and roll). It is therefore no more than an earth ground reference frame rotated around the pitch, yaw and roll axis. The resulting reference frame has the x-axis is pointing where the kite is pointing, the y-axis is oriented in such a way that the kite is pitching down for a positive pitch angle and finally the z-axis is pointing upwards from the kite. It figures in green in Figure: 3.4.

4. The last reference frame defined in this study is the body wind reference frame (WB). As it will be shown later in the description of the experimental setup the apparent wind is measured on-board of the kite, hence the need for a reference frame attached to the kite and shifted with the measured angle of attack. This reference frame is therefore no more than the body reference frame shifted with the measured angle of attack. Therefore the apparent wind will be aligned with the x-axis but in the opposite direction. It figures in blue in Figure: 3.4.

Finally a summary of all he characteristics of each reference frame is made in table 3.2.

3.2.2 Transition matrices

The orientation of the kite system in space is in this work considered to be given by the Euler angles. Several permutations are available but for a question of consistency with the measurement made the Yaw-Pitch-Roll sequence order is used. Therefore using the following matrices enables to transition from the earth ground reference frame into the body reference frame when combining them $R_{EG-B}(\phi_Y, \theta_P, \psi_R) = R_{ROLL}(\psi_R).R_{PITCH}(\theta_P).R_{YAW}(\phi_Y)$:

$$R_{YAW}(\phi_Y) = \begin{pmatrix} \cos(\phi_Y) & \sin(\phi_Y) & 0 \\ -\sin(\phi_Y) & \cos(\phi_Y) & 0 \\ 0 & 0 & 1 \end{pmatrix}; \tag{3.1}$$

$$R_{PITCH}(\theta_P) = \begin{pmatrix} \cos(\theta_P) & 0 & -\sin(\theta_P) \\ 0 & 1 & 0 \\ \sin(\theta_P) & 0 & \cos(\theta_P) \end{pmatrix} \tag{3.2}$$

$$R_{ROLL}(\psi_R) = \begin{pmatrix} 1 & 0 & 0 \\ 0 & \cos(\psi_R) & \sin(\psi_R) \\ 0 & -\sin(\psi_R) & \cos(\psi_R) \end{pmatrix} \tag{3.3}$$

with ϕ_Y, θ_P and ψ_R respectively the yaw, pitch and roll angles. The code for the computation of such matrices and the total transformation is given in the code appendix.

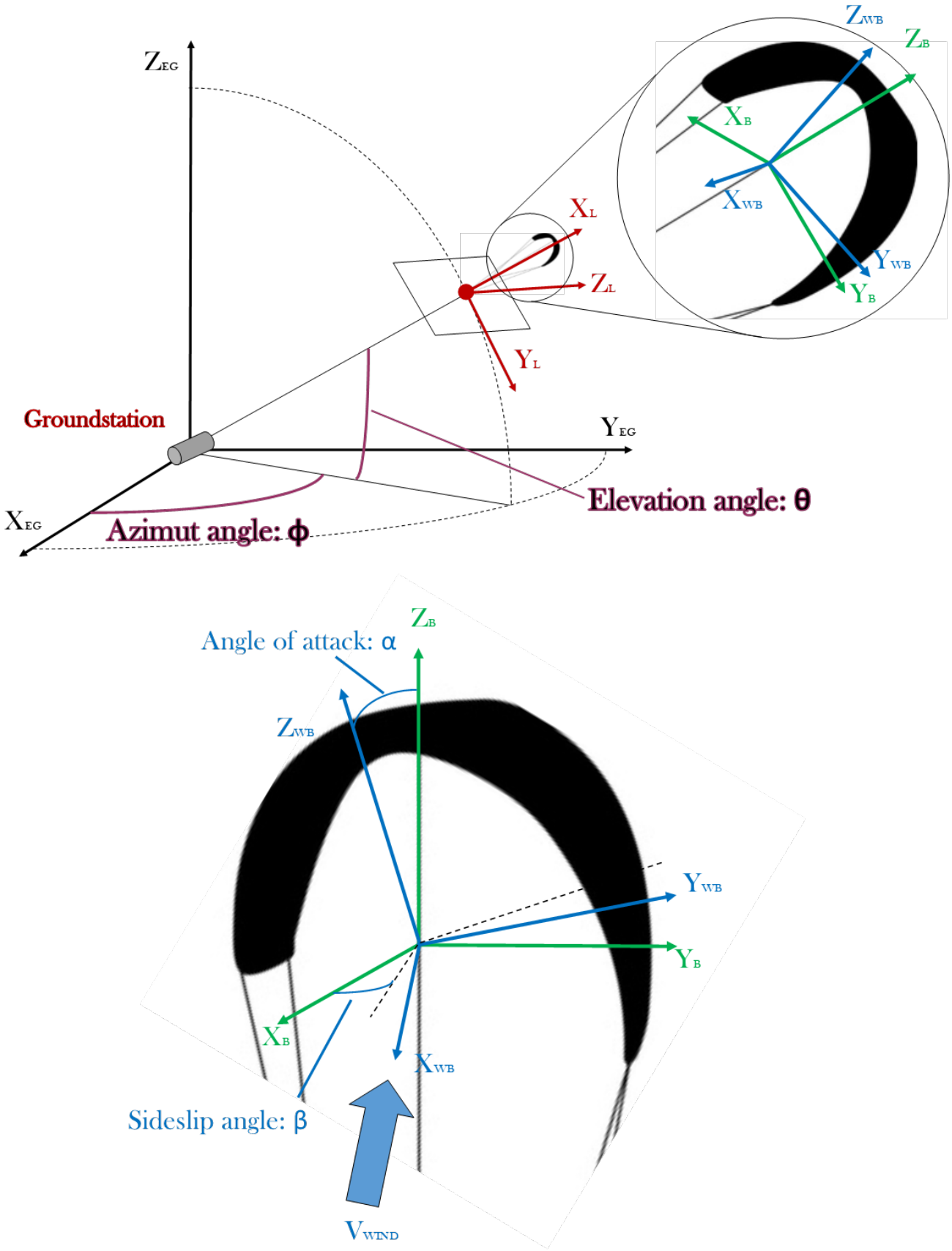

FIGURE 3.4: Reference frame definition

Reference Frame	*Notation*	*Origin*	*X-axis*	*Y-axis*	*Z-axis*	*Use*
Earth Ground	EG	Ground Station	East	North	Up	Used for the description of the kite's trajectory
Local	L	End of the tether	Aligned with tether	Tangential sphere pointing down	Tangential sphere pointing left	Comes handy for the description of the tether's force
Body	B	Center of gravity of the kite	Heading vector of the kite	Points towards the left side of the kite	Points upwards	Comes handy for the sum of force and moments
Wind Body	WB	Center of gravity of the kite	Points upwind and is aligned with the apparent wind	Points to the left side of the kite	Points upwards	Comes handy for the description of the apparent wind

TABLE 3.2: Description of each reference frame

3.3 Equations of motion of the tethered wing

The model chosen to describe the kite system is based on rigid body motion, therefore the linear and rotational movement of the whole kite will be considered and the deformations will either be set aside or studied indirectly with the use of turning law definitions in the aerodynamic model that will be presented later on. It should also be mentioned that when the notion of the "kite system" is mentioned, it refers to the the wing, the bridle line system and the KCU as a whole. The following simplifying assumptions will then have to be made in order to use such a model:

1. The wing's deformations are neglected.
2. The bridle line system is considered to be under enough tension to remain taut and rigid.
3. As a consequence of the previous hypothesis the wing, KCU and bridle lines are considered as one rigid body and is characterized by its mass and tensor of inertia.

Taking into account these hypothesis the equations of motion of the system can be drawn using the Lagrangian framework. Since a verification of the system based on the extracted tether force is wanted further on for the verification of the identified parameters, the equations of the system will be extracted with a constraint motion imposed by the tether, similar to what was done in [15]

3.3.1 Lagrangian estimation

The Lagrangian for the tethered kite system will be computed based on the potential and kinetic equation of the kite system as well as tether. The contribution of the tether to the Lagrangian will have to be neglected when already considering a tether model that already accounts for the weight of the tether into the tether's force that will be applied to the kite's system. Supposing that the kite's center of mass position vector in the earth ground reference frame

is $\mathbf{r(t)} = [x, y, z]$, with t the time and that the kite's orientation is given by a rotation matrix $R(t) = X_B(t), Y_B(t), Z_B(t)$ which corresponds to the transition matrix from the body reference frame into the earth ground reference frame. This matrix is computed from the Euler angles in the following manner :$R^T(t) = R_{YAW}.R_{PITCH}.R_{ROLL}$ as illustrated before and gives the transition from the body reference frame (B) into the earth ground reference frame (EG). Given that the angular velocity vector $\boldsymbol{\omega}(t)$ of the kite in the body reference frame is known. Supposing that the kite's wing, bridle and KCU mass are known and taken as $m_{Kite} = m_{wing} + m_{KCU} + m_{bridle}$, and that the tensor of inertia of the whole assembly is known J_{kite}. Therefore the kinetic T and potential V energy of the whole system can be written:

$$T = \frac{1}{2}\boldsymbol{\omega}^T J_{kite}\boldsymbol{\omega} + \frac{1}{2}m\dot{\mathbf{r}}^T\dot{\mathbf{r}} \; ; \; V = \bar{m}\vec{g}z \tag{3.4}$$

with h the kite's center of gravity height and $\vec{g}$ the gravity and $m = m_{kite} + \frac{1}{3}m_{tether}$ and $\bar{m} = m_{kite} + \frac{1}{2}m_t ether$. Indeed considering that the crosswind component is down rating and decreasing when coming closer to the ground the kinetic energy of the tether can be written as:

$$T_{tether} = \int_0^1 \frac{1}{2}\rho_{tether}A_Q r_0 ||s\dot{\mathbf{r}}||^2 ds = \frac{1}{6}m_{tether}||\dot{\mathbf{r}}||^2 \tag{3.5}$$

and the potential energy of the tether:

$$V_{tether} = \int_0^1 \frac{1}{2}\rho_{tether}A_Q r_0 z s ds = \frac{1}{2}m_{tether}z \tag{3.6}$$

with z the height of the kite and $A_Q = \frac{\pi}{4}d_t^2$. Taking into account that the kite system is under the tether constraint and the rotation constraint imposed by the rotation matrix the following constraints equations can be drawn:

$$c(\mathbf{r}, R, l) = \frac{1}{2}((\mathbf{r} + R\mathbf{r}_T)^T(\mathbf{r} + R\mathbf{r}_T) - l^2) = 0 \tag{3.7}$$

as the constrain imposed by the tether which is considered as a rigid link of varying length l, and $\mathbf{r_T}$ the vector in the body reference frame giving the attachment point of the tether to the wing. The constraint imposed by the rotation matrix is given by:

$$R^T R - I = 0 \tag{3.8}$$

Therefore the Lagrangian reads:

$$L = T - V - \nu T c(\mathbf{r}, R) - tr(Z^T(R^T R - I)) \tag{3.9}$$

where Z is the symmetric matrix of the Lagrange multipliers associated to the orthonormality constraint $R^T R = I$ and ν is the Lagrange multiplier associated to the constraint imposed by the tether and tr is the trace operator.

3.3.2 Extraction of the equations of motion

The equations of motion can be extracted from the Lagrangian and the constraint equations as follow:

$$\frac{d}{dt}\Delta_{\dot{\mathbf{r}}}L - \Delta_{\mathbf{r}}L = \mathbf{F_r}, \;\; c(\mathbf{r}, R) = 0 \tag{3.10}$$

for the momentum equation and for the moment equation:

$$\frac{d}{dt}\Delta_{\dot{R}}L - \Delta_R L = F_R, \;\; R^T R - I = 0 \tag{3.11}$$

The equations for the moment balance are 3×3 differential equations, and make the problem more complex to solve. However a simplification of these equations can be performed using the link between the rotation matrix and the rate of change of the rotation matrix with the angular velocity vector. Indeed it can be shown that $[\boldsymbol{\omega}] = \dot{R}R^T$ with $[.]$ the skew operator defined as follow:

$$[w] = \begin{bmatrix} 0 & -\omega_z & \omega_y \\ \omega_z & 0 & -\omega_x \\ -\omega_y & \omega_x & 0 \end{bmatrix} \tag{3.12}$$

This equation basically says that the time change of the axis of the body reference frame or velocity is equal to the cross product of these axis with the angular velocity. Hence each time variant transformation matrix results in a single angular velocity vector, and the previous equation enables just to do so by going from the angular velocity to the rate of change of the rotation matrix. Now lets define the inverse transformation of the skew operator, the unskew operator U that enables us to go from the rotational matrix to the angular velocity:

$$U \begin{pmatrix} a_{11} & a_{12} & a_{13} \\ a_{21} & a_{22} & a_{23} \\ a_{31} & a_{32} & a_{33} \end{pmatrix} = \begin{pmatrix} a_{32} - a_{23} \\ a_{13} - a_{31} \\ a_{21} - a_{12} \end{pmatrix} \tag{3.13}$$

With this unskew operator the following linear operator can be defined:

$$P_R(A) = U(R^T A) \tag{3.14}$$

with R he rotation matrix from the body reference frame into the local reference frame. As shown in [15] when applying the linear operator P_R to the balance equation for moments (3.11) the following equalities hold:

$$\begin{cases} P_R(\Delta_R tr(Z(R^T R - I))) = 0 \\ 2P_R(\frac{d}{dt}\Delta_{\dot{R}} L - \Delta_R L) = J_{kite}\dot{\boldsymbol{\omega}} + \boldsymbol{\omega} \wedge J_{kite}\boldsymbol{\omega} \\ 2P_R(F_R) = \mathbf{M} \end{cases}$$

where $\mathbf{M}$ is the torque vector applied to the kite in the body reference frame. However to write the system in standard form in order to integrate the equations, that is to write every member of the system as a function of the derivative of the position $\mathbf{r}$, angular velocity $\boldsymbol{\omega}$ and ν the Lagrange multipliers associated to the constraint imposed by the tether, the constraint equations have to be derived twice with respect to time. According to [15] the second derivation of the constraint is $\ddot{c} = \Delta_{\mathbf{r}} c^T \ddot{\mathbf{r}} + 2P_R(\Delta_R c)^T \dot{w} + \Delta_{\dot{\mathbf{r}}} \dot{c}^T \dot{\mathbf{r}} + 2P_R(\Delta_R \dot{c})^T \omega$ Therefore the following system of equation is found:

$$\begin{bmatrix} m & 0 & \Delta_{\mathbf{r}} c \\ 0 & J_{kite} & 2P_R(\Delta_R c) \\ \Delta_{\mathbf{r}} c^T & 2P_R(\Delta_R c)^T & 0 \end{bmatrix} \begin{bmatrix} \ddot{r} \\ \dot{\omega} \\ \nu \end{bmatrix} = \begin{bmatrix} \mathbf{F} + \bar{m}\mathbf{g} \\ \mathbf{M} - \omega \wedge J_{kite}\omega \\ -\Delta_{\mathbf{r}} \dot{c}^T \dot{\mathbf{r}} - 2P_R(\Delta_R \dot{c})^T \omega \end{bmatrix} \tag{3.15}$$

Using the constraint equation 3.7 the system of equation becomes:

$$\begin{bmatrix} m & 0 & \mathbf{r} + R\mathbf{r}_T \\ 0 & J_{kite} & \mathbf{r}_T \wedge R^T \mathbf{r} \\ (\mathbf{r} + R\mathbf{r}_\mathbf{T})^T & (\mathbf{r}_T \wedge R^T \mathbf{r})^T & 0 \end{bmatrix} \begin{bmatrix} \ddot{r} \\ \dot{\omega} \\ \nu \end{bmatrix} = \begin{bmatrix} \mathbf{F} + \bar{m}\mathbf{g} \\ \mathbf{M} - \omega \wedge J_{kite}\omega \\ -\Delta_{\mathbf{r}} \dot{c}^T \dot{\mathbf{r}} - 2P_R(\Delta_R \dot{c})^T \omega + \dot{l}^2 + l\ddot{l} \end{bmatrix} \tag{3.16}$$

where $\Delta_{\mathbf{r}} \dot{c} = \dot{\mathbf{r}} + R(\omega \wedge \mathbf{r_T})$ and $2P_R(\Delta_R \dot{c}) = -(R^T \mathbf{r}) \wedge (\omega \wedge \mathbf{r_T}) - (R^T \dot{\mathbf{r}}) \wedge \mathbf{r_T}$. This system will correspond to the system that will be used for verifying the identified aerodynamic model. One should notice that the terms $(\mathbf{r} + R\mathbf{r}_T)\nu$ scales like a force and $(\mathbf{r}_T \wedge R^T \mathbf{r})\nu$ scales like a

moment. These terms actually correspond to the force and moment imposed by the tether on the kite system. But for system identification these values are measured or can be estimated with measurements. Therefore the system of equations used for system identification can be simplified into:

$$\begin{bmatrix} m & 0 \\ 0 & J_{kite} \end{bmatrix} \begin{bmatrix} \ddot{r} \\ \dot{\omega} \end{bmatrix} = \begin{bmatrix} \mathbf{F} + \bar{m}\mathbf{g} \\ \mathbf{M} - \omega \wedge J_{kite}\omega \end{bmatrix} \tag{3.17}$$

It should again be mentioned that the first line corresponding to the force equation is formulated for the earth ground reference frame while the moment equation corresponding to the second line is formulated in the body reference frame.

3.4 Angular velocity extraction from Euler's angles

The only physical quantity about the kite's orientation that is measured in the experimental setup are the yaw, pitch and roll angles and their respected time rate of change. Therefore a link if it exists has to be found between these values and the instantaneous angular velocity, which are not the same. The angular velocity in the body reference frame can be expressed as $\boldsymbol{\omega} = \omega_{xB}\mathbf{x_B} + \omega_{yB}\mathbf{y_B} + \omega_{zB}\mathbf{z_B}$ while the angular velocity as a function of Euler's angle rate of change is expressed as $\boldsymbol{\omega} = \dot{\phi}_Y \mathbf{x_{EG}} + \dot{\theta}_P \mathbf{y_I} + \dot{\psi}_R \mathbf{x_B}$, with $\mathbf{y_I}$ an intermediate vector as shown in Figure 3.5

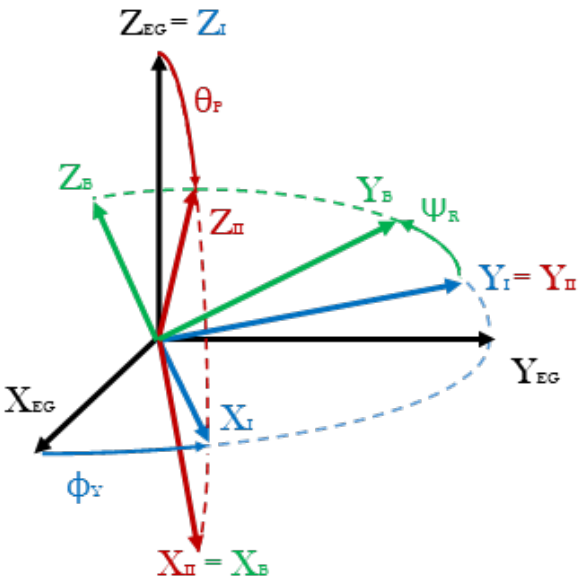

FIGURE 3.5: Euler Angles definition

Therefore using the previously defined rotation matrices it is possible to express $\mathbf{x_{EG}}$ and $\mathbf{y_I}$ as functions of the body reference frame unit vectors $\mathbf{x_B}$, $\mathbf{y_B}$ and $\mathbf{z_B}$. After some manipulations the following expressions are found: $\mathbf{x_{EG}} = -sin(\theta_P)\mathbf{x_B} + cos(\theta_P)sin(\psi_R)\mathbf{y_B} + cos(\theta_P)cos(\psi_R)\mathbf{z_B}$ and $\mathbf{y_I} = cos(\psi_R)\mathbf{y_B} - sin(\psi_R)\mathbf{z_B}$. Therefore the following equalities hold:

$$\begin{cases} \omega_{xB} = sin(\theta_P)\dot{\phi_Y} + \dot{\psi_R} \\ \omega_{yB} = \dot{\phi_Y} sin(\psi_R) + \dot{\theta} cos(\psi_R) \\ \omega_{zB} = \dot{\phi_Y} cos(\theta_P) cos(\psi_R) - \dot{\theta_P} sin(\psi_R) \end{cases}$$

or in matrix form:

$$\boldsymbol{\omega_B} = \begin{pmatrix} \omega_{xB} \\ \omega_{yB} \\ \omega_{zB} \end{pmatrix} = \begin{pmatrix} -sin(\theta_P) & 0 & 1 \\ cos(\theta_P)sin(\psi_R) & cos(\psi_R) & 0 \\ cos(\theta_P)sin(\psi_R) & -sin(\psi_R) & 0 \end{pmatrix} \begin{pmatrix} \dot{\phi_Y} \\ \dot{\theta_P} \\ \dot{\psi_R} \end{pmatrix} \tag{3.18}$$

The corresponding code for calculation is given in the code appendix: A.

3.5 Tether models

One of the main contribution by far to the final force balance used for the evaluation of the aerodynamic force is the tether force (this will be shown further on in the dimensional analysis). Therefore the angle at which the tether tension is delivered at the kite is critical in the evaluation of the aerodynamic forces. This section is then dedicated to the different approaches that can be used in order to estimate the orientation of the tether at its anchor point with the kite as well as the effects of the drag and the weight on the final value of the tension. The goal is to then compare the results of different model with an increasing degree of complexity and fidelity and see whether a high degree of fidelity is worth it. As mentioned in [(]Bigi2018)the tether shape is highly dependent on aerodynamic loading acting on the tether surface and tether gravity acting on the tether volume, therefore different approaches to evaluate this shape will be investigated. For all models the material of the tether is assumed to be made of fibre material such as Dyneema. The properties of the tether are summarized in the following table 3.3:

Table 3.3: Tether properties

Property	***Value***	***Description***
D_T	0.01[m]	Tether diameter
C_{D_T}	0.96	Tether drag coefficient
ρ_T	1034.5[kg/m^3]	Tether density

3.5.1 Straight rod modelling

This is the most simple model studied, proven in Houska[16], Fagiano[11] and [1] that glosses over the flexibility of the tether. Indeed it considers that during powered flights the tensile force is high enough to assume the tether as a rigid rod. This model then enables for a low fidelity estimation of inertial, weight and drag forces but does not allow for the estimation of the shape of the tether. Therefore the tether orientation is directly given by the elevation angle θ and azimuth angle ϕ and the speed distribution due to the motion of the kite and the tether is assumed to vary linearly giving:

$$\dot{\mathbf{r}}(s) = \dot{\mathbf{r}}_{KITE}\frac{s}{r} \tag{3.19}$$

with s the position on the tether. The wind is assumed to follow a power law: $\mathbf{v}^w(z) = \mathbf{v}^w(z_ref)(\frac{z}{z_{ref}})^\alpha$, where $\mathbf{v}^w(z_{ref})$ is the wind speed measured at the ground station, $z_{ref} = 6[m]$ the height at which the wind is measured and finally $\alpha = 0.15$.

3.5.1.0.1 Drag Force Concerning the drag force, it is assumed that only the apparent wind speed at position s (s curvilinear position defined as in figure: 3.6) is contributing to the drag of

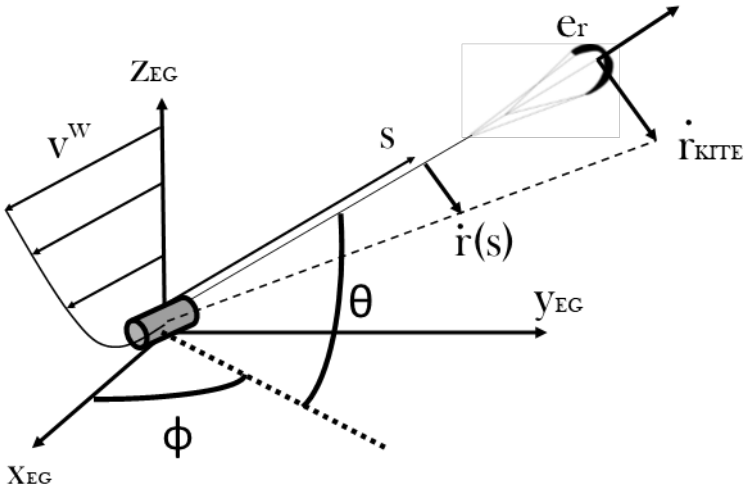

FIGURE 3.6: Straight rod tether model definition

the tether. The final expression for the drag is found by first integrating the moments created by the drag over the tether:

$$\begin{aligned}\mathbf{M}_D &= \int_0^R (s\mathbf{e_r}) \wedge \frac{\rho_{air} C_{D_T} D_T}{2} \left(\frac{s||\mathbf{v}_{a,\perp}||}{r}\right)^2 \frac{\mathbf{v}_{a,\perp}}{||\mathbf{v}_{a,\perp}||} \\ &= (r\mathbf{e_r}) \wedge \frac{\rho_{air} C_{D_T} D_T r}{8} ||\mathbf{v}_{a,\perp}||\mathbf{v}_{a,\perp}\end{aligned} \tag{3.20}$$

where $\mathbf{v}_{a,\perp} = \mathbf{v}_\perp^W(r) - \dot{\mathbf{r}}_{KITE}$ is the apparent wind speed normal to the tether which finally gives by identification the final drag force:

$$\mathbf{F}_D = \frac{\rho_{air} C_{D_T} D_T r}{8} ||\mathbf{v}_{a,\perp}||\mathbf{v}_{a,\perp} \tag{3.21}$$

3.5.1.0.2 Inertial Forces Considering equation 3.19 and deriving it with respect to time once will give the acceleration. Therefore the inertial forces for the tether are:

$$F_I = \int_0^R \mathbf{a}(s)dm = \int_0^R \mathbf{a}_k \frac{x}{R} \rho_T A dx = \frac{1}{2}\rho_T A R \mathbf{a}_k \tag{3.22}$$

3.5.2 2D approach using Benoît Python's model

Benoit Python developed a 2D tether model in his thesis based on the catenary model which accounts for the effect of the drag and of the weight. His work will be used to have an element of comparison in terms of tether shape for the multi mass model. His model then writes:

$$\begin{cases} \frac{d\beta}{dz} = \frac{g\rho_t'}{\tan\beta F_t} + \frac{\rho_{\text{air}} d_t V_a^2}{2F_t}\left(\frac{C_{L,t}}{\tan\beta} + C_{D,t}\right) \\ \frac{dF_t}{dz} = g\rho_t' + \frac{1}{2}\rho_{air} d_t V_a^2 \left(C_{L,t} - \frac{C_{D,t}}{\tan\beta}\right) \\ \frac{dx}{dz} = \frac{1}{\tan\beta} \end{cases} \tag{3.23}$$

where $\rho_t\prime$ is the density of the tether with the following boundary conditions:

$$\begin{cases} V_a(z) = V_{car} + V_w\left(z_{ref}\right)\left(\frac{z}{z_{ref}}\right)^{\alpha} \\ \beta(z=0) = \beta_{\text{ground}} \\ F_t(z=0) = F_{tground} \\ x(z=0) = 0 \end{cases} \tag{3.24}$$

where $\alpha = 0.15$ and $z_{ref} = 6[m]$

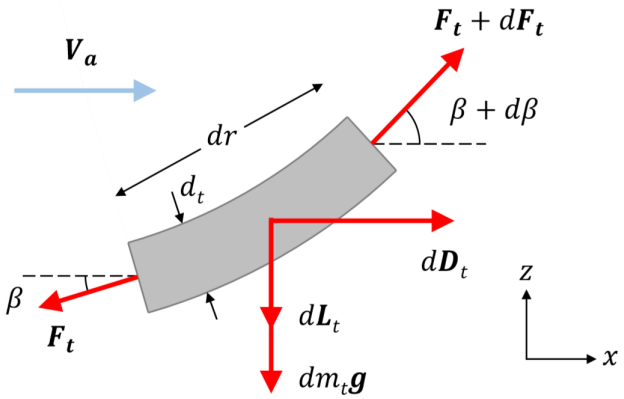

FIGURE 3.7: Tension validation and study of the inlfuence of the number of initial mass [21]

This model was then implemented in python, however when integrating such a model only the z variable is controlled and the x variable is then a result of the integration. Therefore if one does not chose carefully the initial sagging angle at the ground station β_{ground}, the final position of the kite in the x direction might end up being false. Therefore an extra implementation was done to find the initial angle by minimizing the difference between the measured x position and the estimated x position. Also this model was modified for the comparison between the discrete multi mass model. Indeed the wind effect was only considered in the 2D plane defined by the apparent wind whilst the weight effect was only considered in the xz plane.

3.5.3 Discrete mass modelling

The most complete and complex model used in this work for the estimation of the tether's shape and tension is a model based on [29]. In this model the tether is physically divided into a series of point masses connected by inelastic rods representing the tether. The mass and inertial effect and drag forces applied on these rods are then "lumped" to the discrete masses. As mentioned in [29] the advantage of modelling the rods as inelastic links is that it results in a dramatic reduction of the simulation time due to the removal of high frequency content from the cable dynamics. The reel out of the cable is accounted for by adding or retrieving masses. The final idea behind this implementation is to move the end point of the tether along the measured trajectory of the kite to then find the final efforts in the tether as well as its orientation. This means that this model considers that compression, transverse shear, bending and torsional stiffness of the tether can be neglected compared to its tensile stiffness. The entire model was implemented using Python and the resulting code can be found in the code Appendix **[CodeAppendix]**.

3.5.3.1 Dynamic equations of the model

The system model is represented as shown in Figure: 3.8. The final modelled tether consists of n masses connected via n rigid rods, the first one starting at the kite and the last one at the ground station.

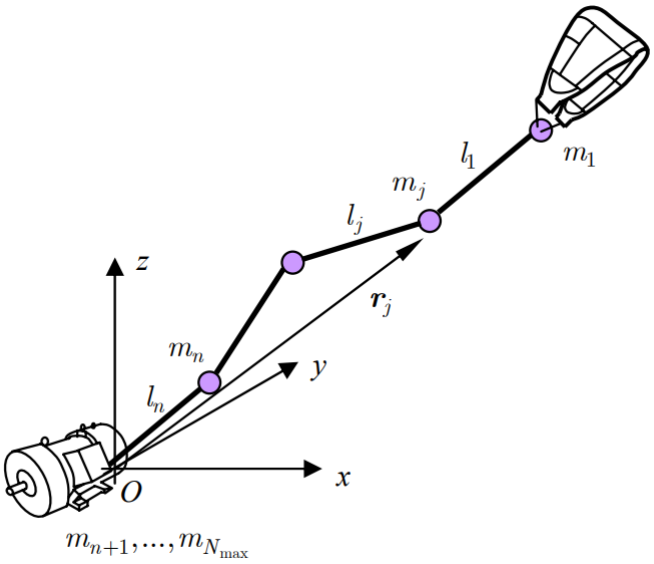

FIGURE 3.8: Description of the entire system [29]

The masses are distributed as follow:

$$m_j = \begin{cases} \frac{1}{2}\rho_T A_1 l_1, \ j = 1 \\ \frac{1}{2}\rho_T (A_j l_j + A_{j-1} l_{j-1}), \ j = 2, ..., n \end{cases}$$

where ρ_T is the density of the material used for the tether, A_j is the cross-sectional area of the j^{th} element and l_j is the length of the j^{th} element. Note that the mass number decreases as one gets closer to the kite. The movement of each mass is then described not with respect to the global earth reference frame but with respect to the reference frame attached to the rod between

the mass in question and the next one as shown in Figure: 3.9. As mentioned in ??, such a description of the movement makes the estimation of the tension in the rods much easier. Indeed when transforming the acceleration of one mass into the rod reference frame, the third term of the acceleration becomes independent of the second order time derivative of the independent coordinates, making the estimation of the tension with a Gaussian elimination method possible.

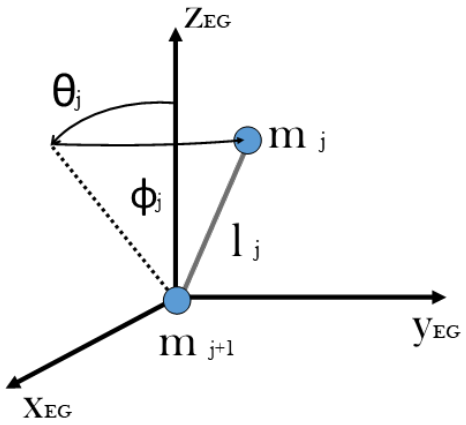

FIGURE 3.9: Definition of the motion of the masses with respect to each other

using the previous figure the position of the j^{th} mass with respect to the $(j+1)^{th}$ mass writes:

$$\mathbf{r}_j = \mathbf{R}_j - \mathbf{R}_{j+1} = [l_j \cos(\phi_j) \sin(\theta_j)\,, l_j \sin(\phi)\,, l_j \cos(\phi_j) cos(\theta_j)]^T \tag{3.25}$$

where $\mathbf{R_j}$ stands for the position of the j^{th} mass in the earth ground reference frame, l_j is the length of the j^{th} segment . Since $m_j \ddot{\mathbf{R}}_j = \mathbf{F}_j$ with $\mathbf{F}_j$ the force applied on the j^{th} mass, the acceleration of one mass with respect to the previous one writes:

$$\ddot{\mathbf{r}}_j = \frac{\mathbf{F}_j}{m_j} - \frac{\mathbf{F}_{j+1}}{m_{j+1}} \tag{3.26}$$

with:

$$\mathbf{F}_j = [F_{xj}, F_{yj}, F_{zj}] + \mathbf{T}_{j-1} - \mathbf{T}_j \tag{3.27}$$

where $[F_{x_j}, F_{y_j}, F_{z_j}]$ is the sum of all external forces acting on the cable (weight and drag), and:

$$\mathbf{T}_j = T_j[\cos(\phi_j) \sin(\theta_j), sin(\phi_j), cos(\phi_j) cos(\theta_j)] \tag{3.28}$$

the tension vector originating from the j^{th} mass, which is supposed to have the same orientation as the rod it belongs to. However all these forces and accelerations are until now defined in the earth ground reference frame and need to be converted to the rod reference frame. As shown in Figure: 3.9, it is obtained by rotating the global earth reference frame by θ_j along its y-axis and then by ϕ_j along its x axis. Therefore the transformation matrix from the global earth reference frame into the rod reference frame then writes:

$$R_j^{EG-ROD} = R_{ROLL}(\phi_j).R_{PTICH}(\theta_j) = \begin{pmatrix} \cos(\theta_j) & 0 & -\sin(\theta_j) \\ -\sin(\theta_j)\sin(\phi_j) & \cos(\phi_j) & -\cos(\theta_j)\sin(\phi_j) \\ \sin(\theta_j)\cos(\phi_j) & \sin(\phi_j) & \cos(\theta_j)\cos(\phi_j) \end{pmatrix} \tag{3.29}$$

From now onwards the tether reference frame attached to the rod between the current and the next mass will be referred using the notation ROD. The product of the double time derivative of 3.25 and the transformation matrix 3.29 gives:

$$\ddot{\mathbf{r}}_{\mathbf{j}}^{ROD} = [l_j\ddot{\theta}_j\cos(\phi_j) - 2l_j\dot{\theta}_j\dot{\phi}_j\sin(\phi_j), l_j\ddot{\phi}_j + l_j\dot{\theta}_j^2\sin(\phi_j)\cos(\phi_j), -l_j\cos^2(\phi_j)\dot{\theta}_j^2 - l_j\dot{\phi}_j^2] \quad (3.30)$$

and combining equations 3.27 and 3.29 consequently gives for the force balance:

$$\begin{aligned} F_{x_j}^{ROD} = {} & \frac{1}{m_j}(F_{x_j}\cos\theta_j - F_{z_j}\sin\theta_j + T_{j-1}\cos\theta_j\cos\phi_{j-1}\sin\theta_{j-1} \\ & - T_{j-1}\sin\theta_j\cos\phi_j\cos\phi_{j-1}\cos\theta_{j-1}) \\ & + \frac{1}{m_{j+1}}((F_{z_{j+1}}\sin\theta_j - F_{x_{j+1}}\cos\theta_j + T_{j+1}\cos\theta_j\cos\phi_{j+1}\sin\theta_{j+1} \\ & - T_{j+1}\sin\theta_j\cos\phi_{j+1}\cos\theta_{j+1}) \end{aligned} \quad (3.31)$$

$$\begin{aligned} F_{y_j}^{ROD} = {} & \frac{1}{m_j}(-\sin\theta_j\sin\phi_j F_{x_j} - T_{j-1}\sin\theta_j\sin\phi_j\cos\phi_{j-1}\sin\theta_{j-1} + T_j\sin^2\theta_j\sin\phi_j\cos\phi_j \\ & + F_{y_j}\cos\phi_j + T_{j-1}\cos\phi_j\sin\phi_{j-1} - T_j\cos\phi_j\sin\phi_j - F_{z_j}\cos\theta_j\sin\phi_j \\ & - T_{j-1}\cos\theta_j\sin\phi_j\cos\phi_{j-1}\cos\theta_{j-1} + T_j\cos^2\theta_j\sin\phi_j\cos\phi_j) \\ & + \frac{1}{m_{j+1}}(F_{x_{j+1}}\sin\theta_j\sin\phi_j + T_j\sin^2\theta_j\sin\phi_j\cos\phi_j - T_{j+1}\sin\theta_j\sin\phi_j\cos\phi_{j+1}\sin\theta_{j+1} \\ & - F_{y_{j+1}}\cos\phi_j - T_j\cos\phi_j\sin\phi_j + T_{j+1}\cos\phi_j\sin\phi_{j+1} + F_{z_{j+1}}\cos\theta_j\sin\phi_j \\ & + T_j\cos^2\theta_j\sin\phi_j\cos\phi_j - T_{j+1}\cos\theta_j\sin\phi_j\cos\phi_{j+1}\cos\theta_{j+1}) \end{aligned} \quad (3.32)$$

$$\begin{aligned} F_{z_j}^{ROD} = {} & \frac{1}{m_j}(\sin\theta_j\cos\phi_j F_{x_j} + T_{j-1}\sin\theta_j\cos\phi_j\cos\phi_{j-1}\sin\theta_{j-1} - T_j\sin^2\theta_j\cos^2\phi_j + F_{y_j}\sin\phi_j \\ & + T_{j-1}\sin\phi_j\sin\phi_{j-1} - T_j\sin^2\phi_j + F_{z_j}\cos\theta_j\cos\phi_j + T_{j-1}\cos\theta_j\cos\phi_j\cos\phi_{j-1}\cos\theta_{j-1} \\ & - T_j\cos^2\theta_j\cos^2\phi_j) \\ & + \frac{1}{m_{j+1}}(-F_{x_{j+1}}\sin\theta_j\cos\phi_j - T_j\sin^2\theta_j\cos^2\phi_j + T_{j+1}\sin\theta_j\cos\phi_j\cos\phi_{j+1}\sin\theta_{j+1} \\ & - F_{y_{j+1}}\sin\phi_j - T_j\sin^2\phi_j + T_{j+1}\sin\phi_j\sin\phi_{j+1} - F_{z_{j+1}}\cos\theta_j\cos\phi_j - T_j\cos^2\theta_j\cos^2\phi_j \\ & + T_{j+1}\cos\theta_j\cos\phi_j\cos\phi_{j+1}\cos\theta_{j+1}) \end{aligned} \quad (3.33)$$

Therefore the movement of the j^{th} mass m_j, is determined by three variables: θ_j, ϕ_j and T_j hence the following definition of the state vector for the j^{th} mass is:

$$S_{vect}^j = [\phi_j, \theta_j, \dot{\phi}_j, \dot{\theta}_j, T_j] \quad (3.34)$$

Right away one can notice in 3.30 that as mentioned before, the third term includes only first

order derivative of the state vector, making the estimation of the tension possible for each mass with the use of a Gaussian elimination algorithm.

3.5.3.2 External forces

Two main external forces are acting on the tether during crosswind flights, the drag and the weight of the KCU. One should also point out that the forces are expressed in the earth ground global reference frame and not in the local reference rod reference frame, since the transformation is already taken into account in 3.31, 3.32 and 3.33.

3.5.3.2.1 Tether drag The drag forces acting on the tether is due to the relative velocity of the wind flowing over its sections. This velocity is computed at the center of each segment and accounts for the apparent wind speed seen by the center of the rod:

$$\mathbf{v}_j = \sum_{i=j+1}^{n} \dot{\mathbf{r}}_i + \frac{\dot{\mathbf{r}}_j}{2} - \mathbf{v}_j^w \tag{3.35}$$

where $\mathbf{v}_j^w$ is the wind velocity vector at the center of the j^{th} cable. It is computed using a power law: $\mathbf{v}_j^w = \mathbf{v}^w(z_ref)(\frac{z_j}{z_{ref}})^\alpha$, where $\mathbf{v}^w(z_{ref})$ is the wind speed measured at the ground station, $z_j = (\sum_{i=j+1}^{n} \mathbf{r}_i + \frac{\mathbf{r}_j}{2}).\mathbf{z_{EG}}$ the height of the center of the j^{th} rod, $z_{ref} = 6[m]$ the height at which the wind is measured and finally $alpha = 0.15$. The value of the exponent was checked with measured data. Since the drag component can be split into a tangential and normal component the tangential and normal speed at the center of the j^{th} rod are computed as:

$$\begin{cases} \mathbf{v}_j^t = \left(\mathbf{v}_j . \frac{\mathbf{r_j}}{|\mathbf{r_j}|}\right) \frac{\mathbf{r_j}}{|\mathbf{r_j}|} \\ \mathbf{v}_j^n = \mathbf{v}_j - \mathbf{v}_j^t \end{cases} \tag{3.36}$$

Then the total drag force of the j^{th} segment is expressed:

$$\mathbf{F}_j^{D-CENTER} = -\frac{1}{2}\rho_{air} C_d l_j d |\mathbf{v}_j|^2 \left(f_n \frac{\mathbf{v}_j^n}{|\mathbf{v}_j^n|} + f_t \frac{\mathbf{v}_j^t}{|\mathbf{v}_j^t|} \right) \tag{3.37}$$

where C_D is the drag coefficient and f_n and f_t are the normal and tangential loading given by:

$$\begin{cases} f_n = 0.5 - 0.1\cos\eta + 0.1\sin\eta - 0.4\cos 2\eta - 0.011\sin 2\eta \\ f_t = 0.01(2.008 - 0.3858\eta + 1.9159\eta^2 - 4.16147\eta^3 + 3.5064\eta^4 - 1.187299\eta^5) \end{cases} \tag{3.38}$$

where $\eta = \arctan\left(\frac{\mathbf{v}_j^n}{\mathbf{v}_j^t}\right)$ is the angle of attack. Finally the resulting drag force is split onto the the two masses at each extremity of the rod:

$$\mathbf{F}_j^D = \begin{cases} \mathbf{F}_j^{D-CENTER}/2, \ j = 1 \\ (\mathbf{F}_j^{D-CENTER} + \mathbf{F}_{j-1}^{D-CENTER})/2, \ j = 2, ..., n \end{cases} \tag{3.39}$$

3.5.3.2.2 Weight The gravitational forces on each mass using the previously defined mass distribution are defined by:

$$\mathbf{F}_j^W = [0, 0, -m_j g] \tag{3.40}$$

3.5.3.3 Incorporating reeling in and out of the tether

Since the rods are inelastic and the tether is subject to a change of length due to its reeling in or out, some method must be implemented to account for this property. A procedure implementing retrieval and additions of masses with a constant reference length is then adopted and described further on. When initializing the system, a reference length for the rod is chosen and set fixed, let's call it L_0. It is computed by taking the initial length of the tether and dividing it by the initial number of masses N_0. The goal is then to describe the variation of the length using this reference length. When the length changes, only the length of the first element is changed and the length of the other elements is kept constant. Once the length of the first element reaches respectively either the reference length or 0, a mass is then added or retrieved. The actual number of masses required N_t changes as well and it is evaluated by taking the upper bound of the result of the division of the actual length L_t by the reference length L_0, giving $N_t = \lceil L_t/L_0 \rceil$. The introduction of a new mass occurs such that it is placed along the same line as the already existing final element. During retrieval the element is removed.

3.5.3.4 Boundary conditions

As mentioned previously the final goal of this model is to move the end of the tether along the measured trajectory of the kite to then retrieve the final efforts and orientation of the tether. To enforce the trajectory specific boundary conditions must be given, one fixing the bottom end of the tether to the ground station and the other one enforcing the acceleration of the last element of the tether. Also since the tether force at the ground station is available in the measurements, a constraint will be set on the tether force of the first element. The boundary conditions must also account for the geometry of the system meaning, namely that there is no element coming after the last tether element. This then translates to the following equations:

$$\begin{cases} T_0 = 0,\ \phi_0 = 0,\ \theta_0 = 0 \\ T_{n+1} = 0,\ \phi_{n+1} = 0,\ \theta_{n+1} = 0 \\ T_n = T_{MEASURED} \\ \ddot{\mathbf{R}}_1 = \mathbf{a}_{MEASURED} \end{cases} \tag{3.41}$$

where $T_{MEASURED}$ and $\mathbf{a}_{MEASURED}$ are respectively the measured tension and acceleration.

3.5.3.5 Implementation of the estimation of tension

Gaussian elimination Using equation 3.33 a standardised form of the tension equation is drawn to fit for a Gaussian elimination algorithm. The equation should be set as:

$$b_T = A_T \mathbf{T} \tag{3.42}$$

where $\mathbf{T} = [T_1, T_2, ..., T_n]$ is a vector of length n that contains the norm of the tension in each rod. Both A_T matrix and b_T vector or defined as follow using equation 3.33.

$$b_T = [b_{T,1}, b_{T,2}, ..., b_{T,n}] \tag{3.43}$$

with:

$$\begin{aligned} b_{T,j} = \ddot{r_z}^{ROD} &- \frac{1}{m_j}(F_{x_j} \sin\theta_j \cos\phi_j + F_{y_j} \sin\phi_j + F_{z_j} \cos\theta_j \cos\phi_j) \\ &+ \frac{1}{m_{j+1}}(F_{x_{j+1}} \sin\theta_j \cos\phi_j + F_{y_{j+1}} \sin\phi_j + F_{z_{j+1}} \cos\theta_j \cos\phi_j) \end{aligned} \tag{3.44}$$

and

$$A_T = \begin{pmatrix} A_{T,(1,1)} & A_{T,(1,2)} & 0 & 0 & ... & 0 & 0 & 0 \\ A_{T,(2,1)} & A_{T,(2,2)} & A_{T,(2,3)} & 0 & ... & 0 & 0 & 0 \\ 0 & A_{T,(3,2)} & A_{T,(3,3)} & A_{T,(3,4)} & ... & 0 & 0 & 0 \\ ... & ... & ... & ... & ... & ... & ... & ... \\ 0 & 0 & 0 & 0 & ... & A_{T,(n-1,n-2)} & A_{T,(n-1,n-1)} & A_{T,(n-1,n)} \\ 0 & 0 & 0 & 0 & ... & 0 & A_{T,(n,n-1)} & A_{T,(n,n)} \end{pmatrix} \tag{3.45}$$

with:

$$\begin{cases} A_{T,(j,j-1)} = \frac{1}{m_j}(\sin\theta_j \cos\phi_j \cos\phi_{j-1} \sin\theta_{j-1} + \sin\phi_j \sin\phi_{j-1} - \cos\theta_j \cos\phi_j \cos\phi_{j-1} \cos\theta_{j-1}) \\ A_{T,(j,j)} = \left(\frac{1}{m_j} + \frac{1}{m_{j+1}}\right)(-\sin^2\theta_j \cos^2\phi_j - \sin^2\phi_j - \cos^2\theta_j \cos^2\phi_j) \\ A_{T,(j,j+1)} = \frac{1}{m_{j+1}}(\sin\theta_j \cos\phi_j \cos\phi_{j+1} \cos\theta_{j+1} + \sin\phi_j \sin\phi_{j+1} + \cos\theta_j \cos\phi_j \cos\phi_{j+1} \cos\theta_{j+1}) \end{cases} \tag{3.46}$$

Including the boundary conditions Since the tether tension is known at the ground station some modification must be brought to both the A_T matrix and b_T vector. Indeed the problem has now $n-1$ unknowns instead of n, therefore the first line and last columns of A_T are no longer needed or can be used as a verification tool. The first element of b_T is also no longer necessary and its two final elements must account for the extra effort generated by the tether tension at the ground station. These modified matrix $A_T\prime$ and vector $b_T\prime$ accounting for the boundary conditions then write:

$$b_T\prime = [b_{T,2}, ..., b_{T,n-1} - A_{T,(n-1,n)}T_n, b_{T,n} - A_{T,(n,n)}T_n] \tag{3.47}$$

and:

$$A_T\prime = \begin{pmatrix} A_{T,(2,1)} & A_{T,(2,2)} & A_{T,(2,3)} & 0 & ... & 0 & 0 \\ 0 & A_{T,(3,2)} & A_{T,(3,3)} & A_{T,(3,4)} & ... & 0 & 0 \\ ... & ... & ... & ... & ... & ... & ... \\ 0 & 0 & 0 & 0 & ... & A_{T,(n-1,n-2)} & A_{T,(n-1,n-1)} \\ 0 & 0 & 0 & 0 & ... & 0 & A_{T,(n,n-1)} \end{pmatrix} \tag{3.48}$$

This formulation is then integrated into Python code by looping over the state vector of each mass and concatenating the lines generated for each mass. For further details the reader is referred to A.

3.5.3.6 Building the entire state vector time variation

The actual state vector implemented in Python only contains the positional argument for each mass and no tension and writes $S_j\prime = [\phi_j, \theta_j, \dot{\phi}, \dot{\theta}]$. Combining equation 3.30,3.31 and 3.32 together enables to write the time variation of the state vector for each mass:

$$\frac{d}{dt}S_j\prime = \frac{d}{dt}\begin{bmatrix}\phi_j \\ \theta_j \\ \dot{\phi}_j \\ \dot{\theta}_j\end{bmatrix} = \begin{bmatrix} \dot{\phi}_j \\ \dot{\theta}_j \\ \frac{1}{l_j}(F_y^{ROD} - l_j\dot{\theta_j}^2 \sin\phi_j \cos\phi_j) \\ \frac{1}{l_j \cos\phi_j}(F_x^{ROD} + 2l_j\dot{\theta}_j\dot{\phi}_j \sin\phi_j) \end{bmatrix} \tag{3.49}$$

with the final state vector for a certain time step: $S\prime = [S_1\prime, S_2\prime, ..., S_n\prime]$.This expression is then implemented into python and solved using a Runge Kutta method.

3.5.3.6.1 Boundary conditions The boundary conditions must account for the fact that the trajectory of the tether's end point is enforced by setting the acceleration of this element $\ddot{\mathbf{R}}_1$ as the one that is measured. This then means that intrinsically the sum of forces applied on the last mass of the tether is known and using equation 3.26 the time variation of the first order derivative of the position angles would then write:

$$\begin{aligned}\frac{d}{dt}\dot{\phi}_1 = \ddot{\mathbf{R}}_{\mathbf{1,y}} + \frac{1}{m_2}(&F_{x_2}\sin\theta_1\sin\phi_1 + T_1\sin^2\theta_1\sin\phi_1\cos\phi_1 - T_2\sin\theta_1\sin\phi_1\cos\phi_2\sin\theta_2\\ &- F_{y_2}\cos\phi_1 - T_1\cos\phi_1\sin\phi_1 + T_2\cos\phi_1\sin\phi_2 + F_{z_2}\cos\theta_1\sin\phi_1\\ &+ T_1\cos^2\theta\sin\phi_1\cos\phi_1 - T_2\cos\theta_1\sin\phi_1\cos\phi_2\cos\theta_2)\end{aligned} \tag{3.50}$$

$$\begin{aligned}\frac{d}{dt}\dot{\theta}_1 = \ddot{\mathbf{R}}_{\mathbf{1,x}} + \frac{1}{m_2}(&F_{z_2}\sin\theta_1 - F_{x_2}\cos\theta_1 + T_2\cos\theta_1\cos\phi_2\sin\theta_2\\ &- T_2\sin\theta_1\cos\phi_2\cos\theta_2)\end{aligned} \tag{3.51}$$

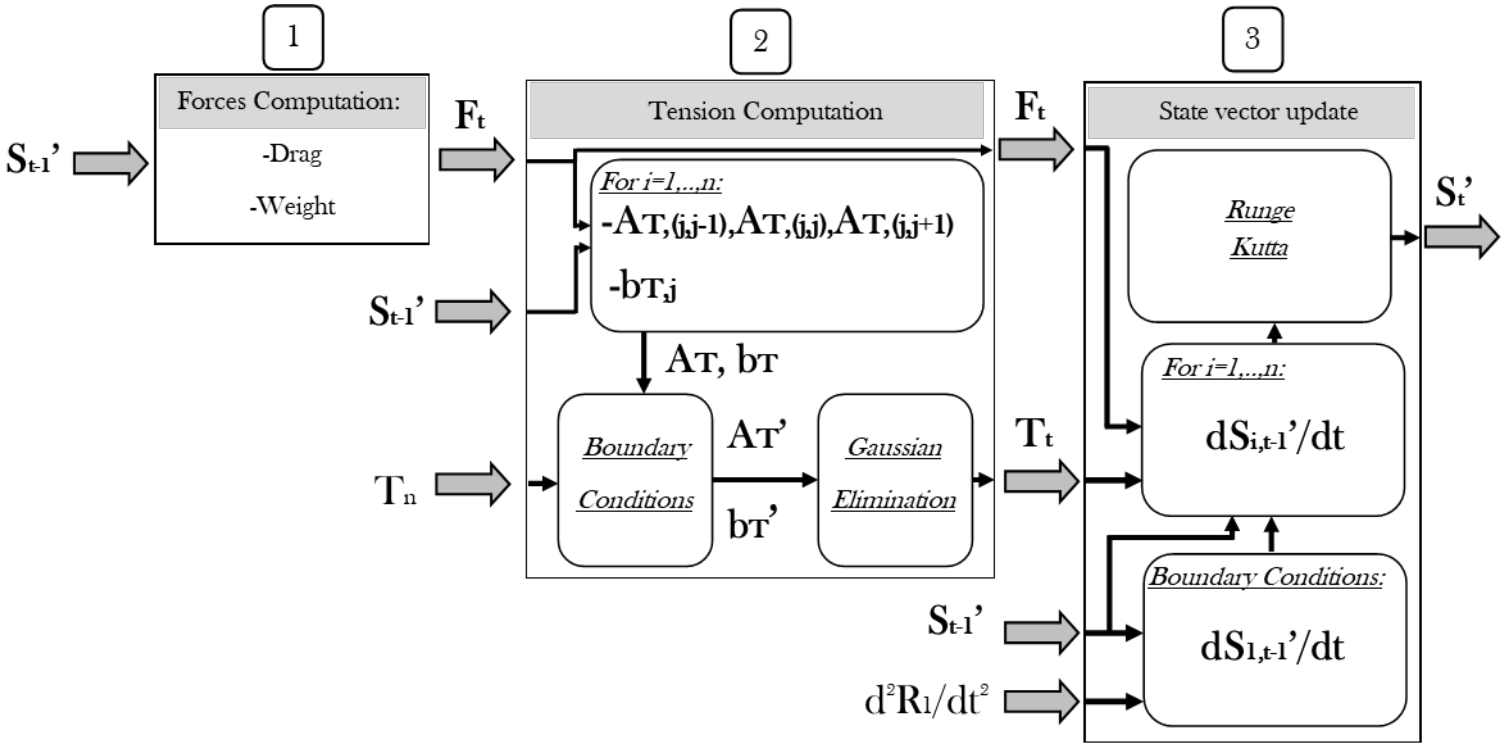

FIGURE 3.10: Algorithm summary

3.5.3.7 Model Validation

The discrete multi mass model needs a validation of some sort, to first of all ensure no mistakes were made, but also have confidence that the model will give sound and coherent physical results. Two simple cases were studied for validation, the first one being the drop of a chain subject to its own weight and the second where a crosswind will be blowing over the tether. For the second case no experimental results nor validated model are available so the outcome of the simulation will be compared to results from other models. For each validation the initial number of mass was 50.

3.5.3.7.1 Catenary validation For the case where the tether is falling because of its own weight, once the fall of the cable is stabilised it will be compared to the largely validated centenary equation result given by:

$$y(x) = a\cosh\left(\frac{x - D/2}{a}\right) - a\cosh\left(\frac{D/2}{a}\right) \tag{3.52}$$

where $a = \frac{T_0}{g\rho_T A_T}$, with T_0 is the tension at the ground station, A_T is the cross sectional area of the tether and D is the distance between the two anchor points of the tether. Further investigation of the tension in the tether will also be done. For this study a distance of $300[m]$ between the two ends of the tether is chosen because it is representative of the average tether length. The implementation of the discrete mass model for this case is done by initializing the tether length at $300[m]$ and reeling it out until its length reaches the one from the catenary equation. As shown in Figure: 3.11 the discrete multi mass model is in the end comparable to the catenary equation. Notice also the dynamic fall and stabilization of the discrete mass model, which in the end nearly matches the catenary equation results.

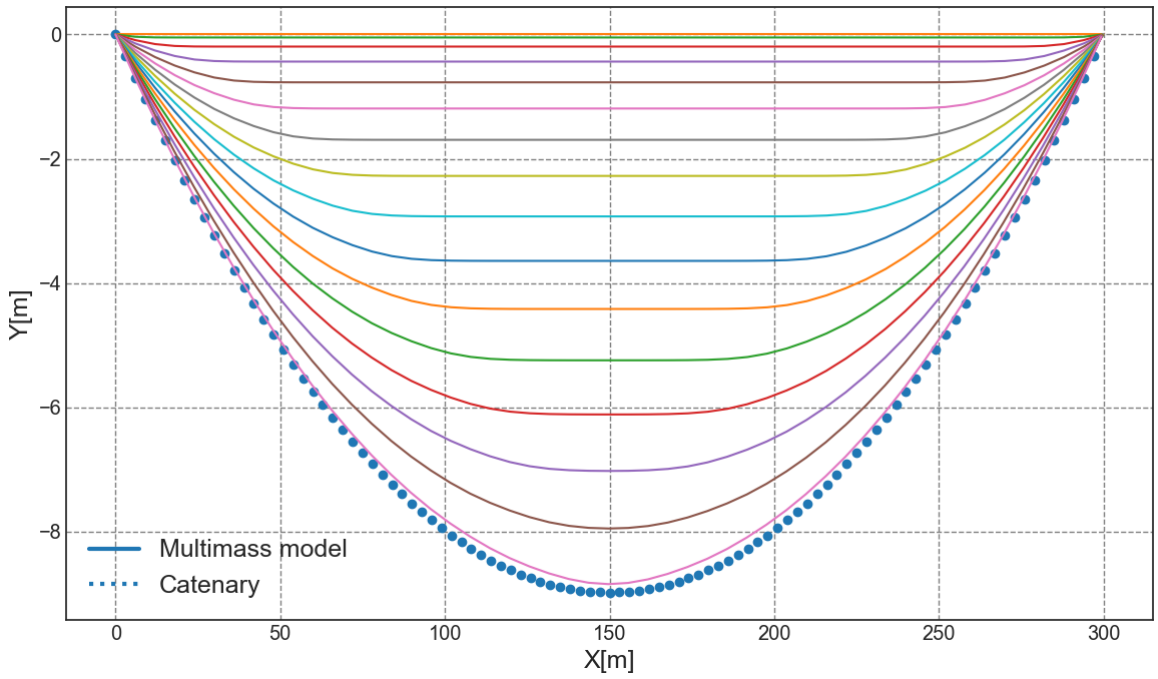

FIGURE 3.11: Catenary equation validation

The tension found by the discrete mass model was also compared to the one found with the catenary model, as a verification for the implementation of the estimation of the tension values. As shown in figure: 3.12 the tensions are similar. The opportunity to study the influence of the number of initial masses on the tension value was also taken. The outcome is that the amount of mass changes very slightly the final value of the tension and that an initialisation with $25 masses$ is sufficient.

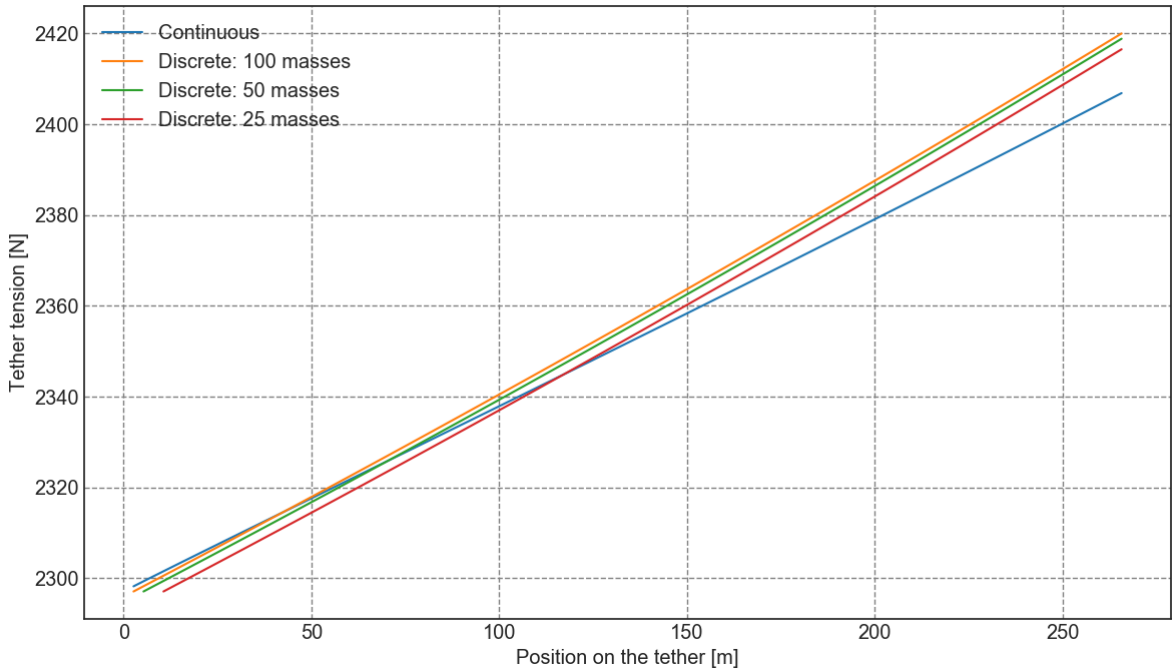

FIGURE 3.12: Tension validation and study of the inlfuence of the number of initial mass

3.5.3.7.2 Wind drag validation The same reeling out implementation is adopted in this section. The tether is maintained vertically and the wind is blowing in the positive x-axis direction. The results of Figure: 3.13 show no incoherence and are comparable to the ones found in [2].

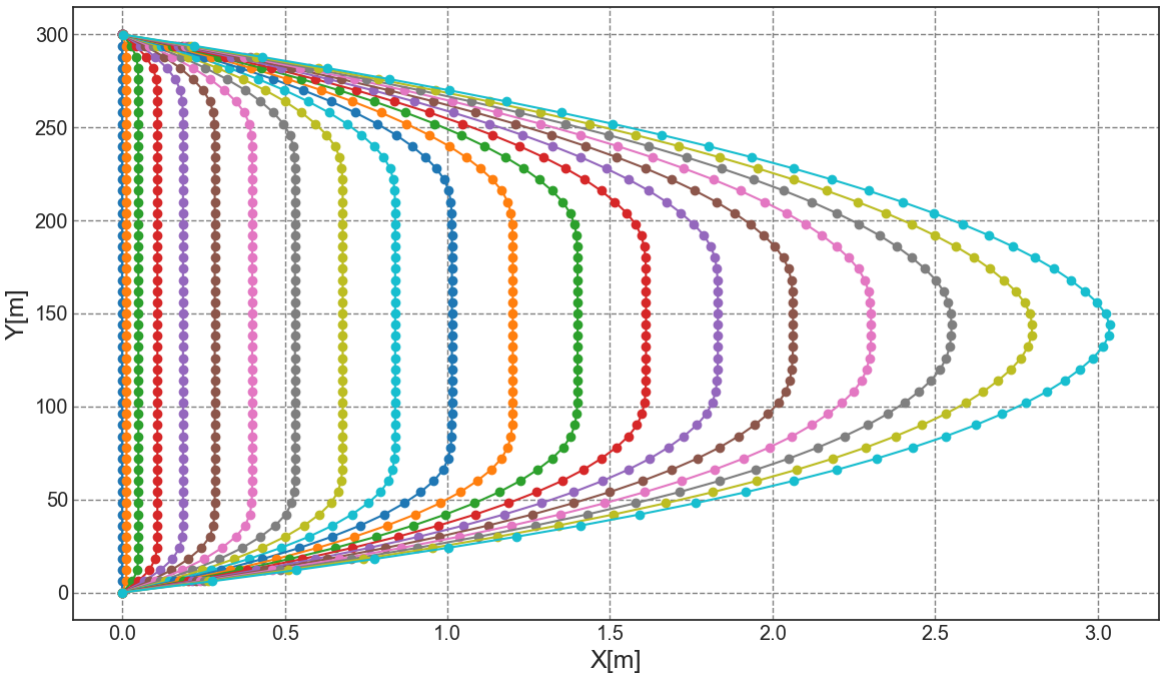

FIGURE 3.13: Wind drag validation

3.6 Force and moment computation

This section aims at giving a short summary of which efforts were considered and how they were applied onto the kite system.

3.6.1 Tether force

The tether force was considered using either the straight rod model or the multi mass model. When considering the multi mass model the tether weight ,drag and inertia were already accounted for in the final value of the tension, meaning that both of the terms m and $\bar{m}$ in equation 3.17 had to be changed by subtracting the tether's weight effect. The orientation of the tether also changed whether the multi mass model or the straight rod model were implemented. The moment of the tether on the kite was also accounted for by taking a lever arm of $\mathbf{d}_{KCU} = [0, 0, -8.54]$. The effort considered in the final force balance is then:

$$\begin{cases} \mathbf{F}_{Tether} = T_{Meas}\mathbf{T}_{dir,EG} \\ \mathbf{M}_{Tether} = \mathbf{d}_{KCU} \wedge R_{EG-B}\mathbf{F}_{Tether} \end{cases} \tag{3.53}$$

where T_{Meas} is the measured tension, $\mathbf{T}_{dir}$ is the orientation of the tether at the anchor point with the kite.

3.6.2 Weight force

The weight force of KCU, bridle line system, wing and tether if it is considered as a rod are taken into account for the force balance. The final effort are then:

$$\mathbf{W}_{total} = (m_{KCU} + m_{Tether} + m_{Wing} + m_{Bridle})\mathbf{g} \tag{3.54}$$

3.6.3 Additional drag force

The model also accounts for some additional drag forces like the drag coming from the KCU module or the drag of the tether when the straight rod model was considered. These forces were also accounted for in the moment equation by taking a lever arm of $\mathbf{d}_{KCU} = [0, 0, -8.54]$. The final efforts considered are then:

$$\begin{cases} \mathbf{F}_{D_{KCU}} = \frac{1}{2}\rho_{air}A_{KCU}C_{D,KCU}||\mathbf{v}_a||^2\frac{\mathbf{v}_a}{||\mathbf{v}_a||} + \mathbf{D}_T \\ \mathbf{M}_{D_{KCU}} = \mathbf{d}_{KCU} \wedge R_{EG-B}\mathbf{F}_{D_{KCU}} \end{cases} \tag{3.55}$$

where $A_{KCU} = 1.6[m^2]$ also accounting for the surface area of a wind turbine, $C_{D,KCU} = 1$ assuming that the KCU is a blunt body and $\mathbf{D}_T$ the drag of the tether computed with the rod tether model if this model is selected.

3.6.4 Additional inertial forces

The inertia of the KCU was also added in the model. First the trajectory of the KCU was computed and then derived twice with respect to time to find the acceleration. Finally the inertia of the KCU is found by multiplying the acceleration by the mass of the KCU. The moment applied by the inertia of the KCU on the kite is also considered. The length of the lever arm for this moment is taken as $\mathbf{d}_{KCU} = [0, 0, -8.54]$. The final contribution then writes:

$$\begin{cases} \mathbf{F}_{I_{KCU}} = m_{KCU}\mathbf{a}_{KCU} \\ \mathbf{M}_{I_{KCU}} = \mathbf{d}_{KCU} \wedge R_{EG-B}\mathbf{F}_{I_{KCU}} \end{cases} \tag{3.56}$$

3.6.5 Total force contribution

When summing all these contribution except for the aerodynamic efforts, the total external force contribution writes:

$$\begin{cases} \mathbf{F}_{Ext} = \mathbf{F}_{Tether} + \mathbf{W}_{total} + \mathbf{F}_{D_{KCU}} + \mathbf{F}_{I_{KCU}} \\ \mathbf{M}_{Ext} = \mathbf{M}_{Tether} + \mathbf{M}_{D_{KCU}} + \mathbf{M}_{I_{KCU}} \end{cases} \tag{3.57}$$

these are all the efforts used for the estimation of the aerodynamic coefficients.

3.7 Kinematics of depowering

As mentioned before the wing is put into either power mode or depower mode by respectively shortening or lengthening the power tape. This plays on the difference of length between the rear and the front bridle lines, which in term will bring the wing's chord line close to perpendicular to the front bridle line when powered and move it away from this position as the tape is lengthened, as illustrated in 3.14.When shortening the tape the angle of attack with respect to the apparent wind increases and so does the power. When increasing the tape the opposite happens.

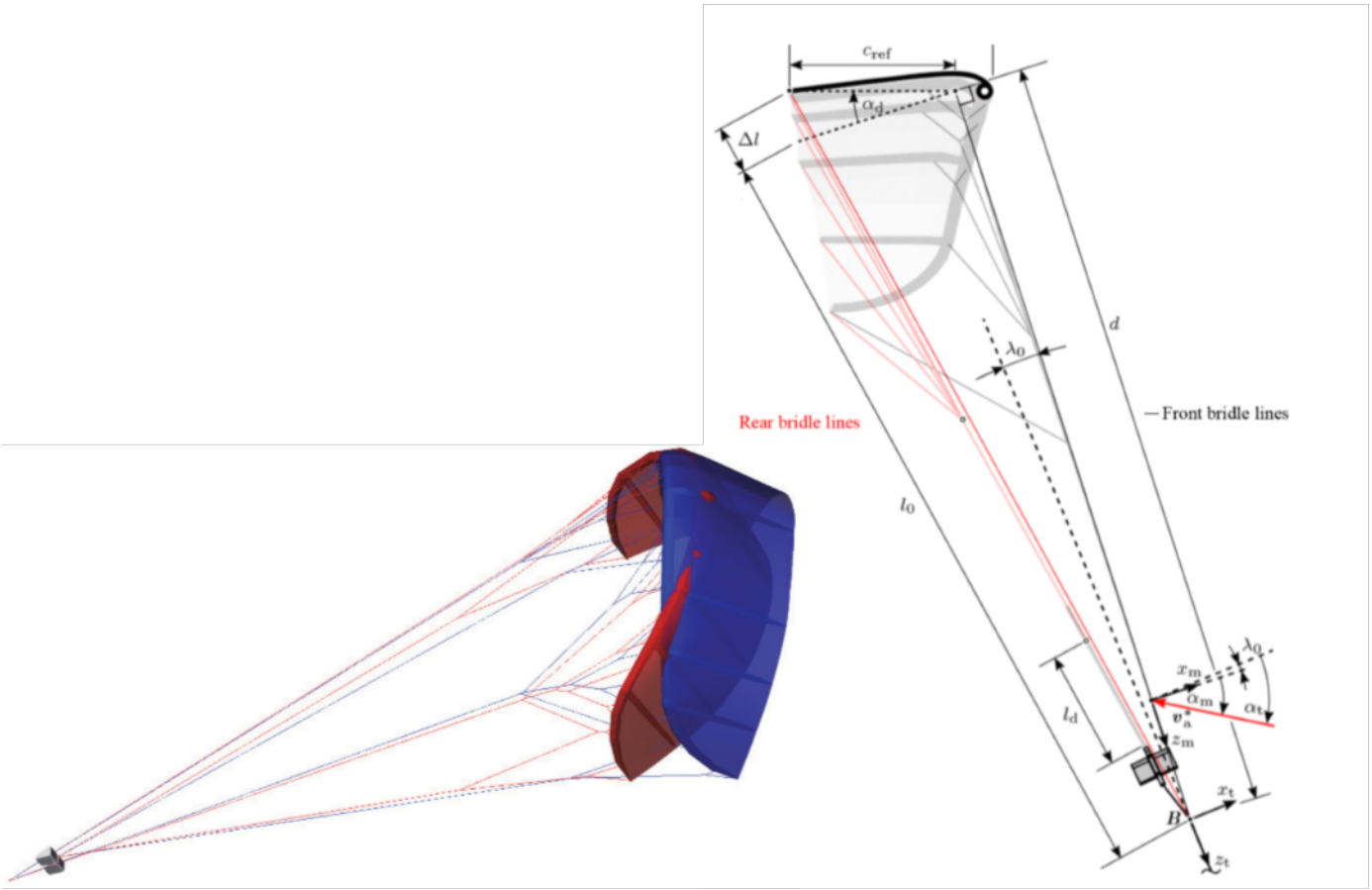

FIGURE 3.14: Illustration of powered mode (in red) and depowered mode (in blue) and Oehler's model illustration [(]Oehler)

Since the angle of attack of the apparent wind is measured with respect to the front bridle line, it must be corrected to account for the angle between the chord of the wing and the front

bridle lines. This is achieved by using a geometric model previously developed by Oehler [20] as illustrated in 3.14.Using the laws of cosines in the defined by the front and rear bridle lines and chord of the wing gives:

$$\cos(\pi/2 + \alpha_d) = \frac{d^2 + c_{ref}^2 - (l_0 + \Delta l)^2}{2dc_{ref}} \tag{3.58}$$

Given the layout of the actuation system the extension of the rear bridle line system due to the power input is then approximated as:

$$\Delta l = \frac{1}{2} l_d = \frac{1 - u_p}{2} l_{d,max} \tag{3.59}$$

with l_d is the deployed length of the depower tape. The half factor comes from the actuation system which comprises a pulley. All the geometrical properties needed and used for the calculations of this correction are given in table3.4.

TABLE 3.4: Geometric properties of the kite

Property	***Value***
d	11[m]
c_{ref}	2.2[m]
l_0	11.22[m]
$l_{d,max}$	1.7[m]

3.8 Aerodynamic Model

An aerodynamic model based on Fechner's four point mass approach [13] was built for system identification, for the exception that here only three points are chosen and correspond to three aerodynamic centers (K,L,R) (see Figure 3.15). This model was selected because it could handle the fact that the turning of a soft kite comes from the side ears of C-shaped kite. Different aerodynamic models based on this architecture will be developed and tested onto either selected part of the data (powered flight for example) or the full data. The variation of an aerodynamic model here stands for: the aerodynamic forces contributing to the force and torque balance, the formulation of the lift coefficient with respect to input variables.

3.8.1 Local velocities

The local apparent wind velocities in the body reference frame in point K, L and R are found by taking into account the angular velocity of the kite:

$$\begin{cases} \mathbf{v}_{a,B}^K = \mathbf{v}_{a,B,Meas}^K - \omega \wedge \mathbf{r}_B \\ \mathbf{v}_{a,B}^L = \mathbf{v}_{a,B,Meas}^L - \omega \wedge \mathbf{r}_B \\ \mathbf{v}_{a,B}^R = \mathbf{v}_{a,B,Meas}^R - \omega \wedge \mathbf{r}_B \end{cases} \tag{3.60}$$

3.8.2 Aerodynamic forces 3 plate model

Such a model is set to generate two aerodynamic forces at each aerodynamic center, namely a lift and a drag. The drag will be assumed as aligned with the incoming flow while the lift will be taken as perpendicular to the incoming flow and local plane defining the aerodynamic surface. Therefore the aerodynamic lift in point B with the adopted notation writes:

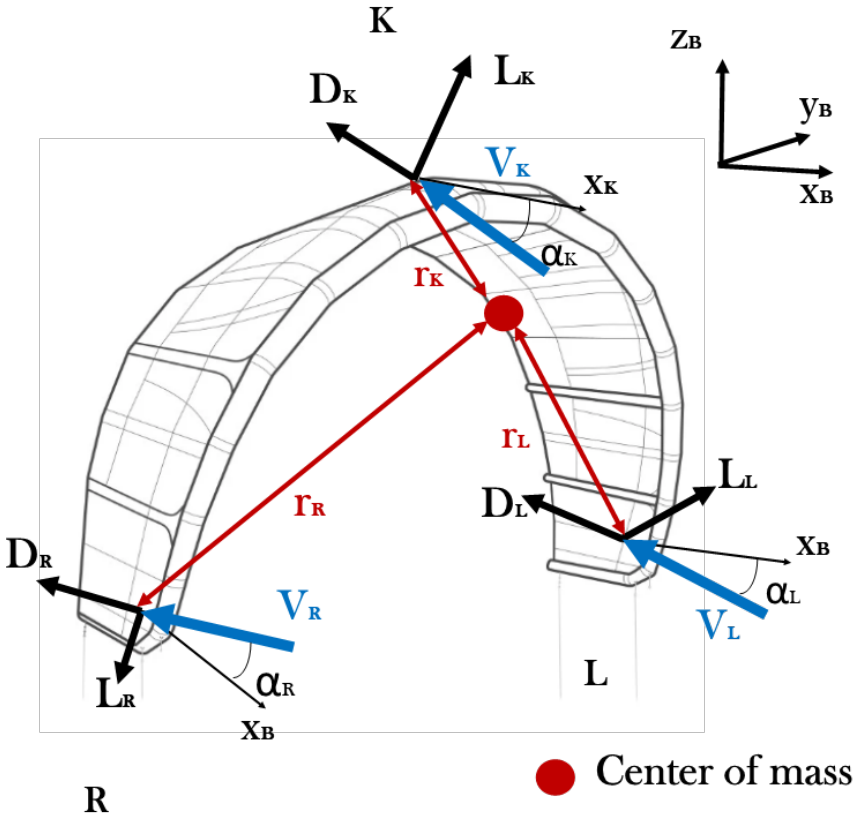

FIGURE 3.15: Definition of the aerodynamic model and centers

For point K:

$$\mathbf{L}_{EG}^{K} = \frac{1}{2}\rho(\mathbf{v}_{a,EG}^{xzB,K})^2 A C_L^K \frac{\mathbf{v}_{a,EG}^{K} \wedge \mathbf{e}_{EG}^{yB}}{||\mathbf{v}_{a,EG}^{K} \wedge \mathbf{e}_{EG}^{yB}||} = \mathbf{v}_{L,K} C_L^K \tag{3.61}$$

where $\mathbf{L}_{EG}^{K}$ is the lift component in point K written in the earth ground reference frame, $\mathbf{v}_{a,EG}^{xzB,K}$ is the apparent wind speed component in the xz plane of the body reference frame B at point K written in the earth ground reference frame EG, $\mathbf{e}_{EG}^{yB}$ is the y unit vector in the body reference frame B written in the earth ground reference frame EG, C_L^K is the lift coefficient in point K, A is the projected surface area of the kite and ρ is the density of air. The rest of the aerodynamic forces then follows:

$$\mathbf{L}_{EG}^{L} = \frac{1}{2}\rho(\mathbf{v}_{a,EG}^{xyB,L})^2 A C_L^L \frac{\mathbf{e}_{EG}^{zB} \wedge \mathbf{v}_{a,EG}^{L}}{||\mathbf{e}_{EG}^{zB} \wedge \mathbf{v}_{a,EG}^{L}||} = \mathbf{v}_{L,L} C_L^L \tag{3.62}$$

$$\mathbf{L}_{EG}^{R} = \frac{1}{2}\rho(\mathbf{v}_{a,EG}^{xyB,R})^2 A C_L^R \frac{\mathbf{v}_{a,EG}^{R} \wedge \mathbf{e}_{EG}^{zB}}{||\mathbf{v}_{a,EG}^{R} \wedge \mathbf{e}_{EG}^{zB}||} = \mathbf{v}_{L,R} C_L^R \tag{3.63}$$

The aerodynamic drag then follows for each aerodynamic center:

$$\mathbf{D}_{EG}^{K} = \frac{1}{2}\rho(\mathbf{v}_{a,EG}^{K})^2 A C_L^K \frac{\mathbf{v}_{a,EG}^{K}}{||\mathbf{v}_{a,EG}^{K}||} = \mathbf{v}_{D,K} C_L^K \tag{3.64}$$

$$\mathbf{D}_{EG}^{L} = \frac{1}{2}\rho(\mathbf{v}_{a,EG}^{L})^2 A C_L^L \frac{\mathbf{v}_{a,EG}^{L}}{||\mathbf{v}_{a,EG}^{L}||} = \mathbf{v}_{D,L} C_L^L \tag{3.65}$$

$$\mathbf{D}_{EG}^{R} = \frac{1}{2}\rho(\mathbf{v}_{a,EG}^{R})^{2} A C_{L}^{R} \frac{\mathbf{v}_{a,EG}^{R}}{||\mathbf{v}_{a,EG}^{R}||} == \mathbf{v}_{D,R} C_{L}^{R} \tag{3.66}$$

3.8.3 Aerodynamic torques 3 plate model

The equations of motions regarding the moment balance is in the body reference frame, therefore the aerodynamic torques applied to the center of mass of the kite are the result of the cross product of the previously defined aerodynamic force transformed into the body reference frame and the location of the aerodynamic center in question in the body reference frame. This then gives for point K for the lift:

$$\mathbf{T}_{L,B}^{K} = \mathbf{r}_{B}^{K} \wedge \mathbf{L}_{B}^{K} \tag{3.67}$$

where $\mathbf{T}_{L,B}^{K}$ is the torque generated by the lift force at point K in the body reference frame B, $\mathbf{r}_{B}^{K}$ is the position of point K in the body reference frame, $\mathbf{L}_{B}^{K} = R_{EG-B}(\phi_Y, \theta_P, \psi_R)\mathbf{L}_{EG}^{K}$ is the estimated lift force in the body reference frame. The same notation is adopted for the rest of the aerodynamic points and the torque generated by the drag:

$$\mathbf{T}_{L,B}^{L} = \mathbf{r}_{B}^{L} \wedge \mathbf{L}_{B}^{L} \tag{3.68}$$

$$\mathbf{T}_{L,B}^{R} = \mathbf{r}_{B}^{R} \wedge \mathbf{L}_{B}^{R} \tag{3.69}$$

$$\mathbf{T}_{D,B}^{K} = \mathbf{r}_{B}^{K} \wedge \mathbf{D}_{B}^{K} \tag{3.70}$$

$$\mathbf{T}_{D,B}^{L} = \mathbf{r}_{B}^{L} \wedge \mathbf{D}_{B}^{L} \tag{3.71}$$

$$\mathbf{T}_{D,B}^{R} = \mathbf{r}_{B}^{R} \wedge \mathbf{D}_{B}^{R} \tag{3.72}$$

Whether the drag generated by the sides of a C-shape kite contribute to the turning of the kite is debatable, indeed [7] showed that the main contribution to the turning of such a kite is mainly due to the induced skewing when steering. However it is still mentioned in his thesis that the drag has a small contribution to this turning. Therefore and as it will be shown further down, different model accounting for the drag as a steering mechanism or not will be developed and will hopefully highlight whether or not the drag does contribute to the turning of a kite. The distances of the aerodynamic center from the center of mass are computed by assuming that the aerodynamic center is at the quarter chord which seems in line with the mass distribution used by Bosh et al. [5] and the average ratio of 3:1 for the forces in front and rear bridle line measured by Hummel [17] for different kites. The final distances are:

$$\begin{cases} r_K = [-0.55, 0, 2.46] \\ r_L = [-0.75, 4.115, 0.95] \\ r_R = [-0.75, -4.115, 0.95] \end{cases} \tag{3.73}$$

3.8.4 Direct identification of the aerodynamic parameters

Using the previously defined aerodynamic forces the total aerodynamic model can be written in matrix form as:

$$\begin{bmatrix} \mathbf{F}_{EG}^{A} \\ \mathbf{M}_{B}^{A} \end{bmatrix} = \begin{bmatrix} \mathbf{v}_{L,K} & \mathbf{v}_{L,L} & \mathbf{v}_{L,R} & \mathbf{v}_{D,K} & \mathbf{v}_{D,L} & \mathbf{v}_{D,R} \\ \mathbf{v}_{M_L,K} & \mathbf{v}_{M_L,L} & \mathbf{v}_{M_L,R} & \mathbf{v}_{M_D,K} & \mathbf{v}_{M_D,L} & \mathbf{v}_{M_D,R} \end{bmatrix} \begin{bmatrix} C_L^K \\ C_L^L \\ C_L^R \\ C_D^K \\ C_D^L \\ C_D^R \end{bmatrix} \tag{3.74}$$

where the terms $\mathbf{v}_{M_L,P} = \mathbf{r}_B^L \wedge (R_{EG-B}\mathbf{v}_{L,P})$ is the term found in the previous matrix at point P. From equation 3.17 and 3.57 the forces and moments the aerodynamic parameters must balance is extracted, and therefore $\mathbf{F}_{EG}^A$ and $\mathbf{M}_{EG}^A$ are known. Also using the measurements the velocity terms are known, so all the information needed is available to invert equation 3.74 and find the aerodynamic coefficients.

3.8.5 Parameter system identification

Now supposing that the lift and drag coefficients are functions of the local angle of attack α_K , α_R &α_L as well as power input u_p and steering input u_s such that for example:

$$\begin{cases} C_L^K = C_{L,t}^0 + C_{L,t}^1\alpha_K + C_{L,t}^2\alpha_K^2 + C_{L,t}^3 u_p + C_{L,t}^4 u_p^2 \\ C_D^K = C_{D,t}^0 + C_{D,t}^1\alpha_K + C_{D,t}^2\alpha_K^2 + C_{D,t}^3 u_p + C_{D,t}^4 u_p^2 \\ C_L^L = C_{L,s}^0 + C_{L,s}^1 u_s + C_{L,s}^2 u_s^2 + C_{L,s}^3 u_p \\ C_D^L = C_{D,s}^0 + C_{D,s}^1 u_s + C_{D,s}^2 u_s^2 + C_{D,s}^3 u_p \\ C_L^R = C_{L,s}^0 - C_{L,s}^1 u_s + C_{L,s}^2 u_s^2 + C_{L,s}^3 u_p \\ C_D^R = C_{D,s}^0 - C_{D,s}^1 u_s + C_{D,s}^2 u_s^2 + C_{D,s}^3 u_p \end{cases} \tag{3.75}$$

Any formulation can be thought of but for the moment the choice was made to start with a simple model. Notice also that $u_s < 0$ for a right turn hence the change of sign. Once the formulation is found the problem is written down in such a way that a least square optimisation of the parameters from equation 3.75 is possible. The system of equation looked for is:

$$\begin{bmatrix} \mathbf{F}_{EG}^A \\ \mathbf{M}_B^A \end{bmatrix} = \Phi^T\Theta \tag{3.76}$$

where Φ is function of $\mathbf{v}_{L,K}, \mathbf{v}_{L,L}, \mathbf{v}_{L,R}, \mathbf{v}_{D,K}, \mathbf{v}_{D,L}, \mathbf{v}_{D,R}, \mathbf{v}_{M_L,K}, \mathbf{v}_{M_L,L}, \mathbf{v}_{M_L,R}, \mathbf{v}_{M_D,K}, \mathbf{v}_{M_D,L}, \mathbf{v}_{M_D,R}$ such that Θ can be written as:

$$\begin{aligned} \Theta^T = [&C_{L,t}^0,\ C_{L,t}^1,\ C_{L,t}^2,\ C_{L,t}^3,\ C_{L,t}^4,\ C_{D,t}^0,\ C_{D,t}^1,\ C_{D,t}^2,\ C_{D,t}^3, \\ &C_{D,t}^4,\ C_{L,s}^0,\ C_{L,s}^1,\ C_{L,s}^2,\ C_{L,s}^3,\ C_{D,s}^0,\ C_{D,s}^1,\ C_{D,s}^2,\ C_{D,s}^3] \end{aligned} \tag{3.77}$$

Then using the equations 3.57 and 3.17 and the measurements an estimation of the parameters $\hat{\Theta}$ is found using least square giving:

$$\hat{\Theta} = \left[\sum_{k=1}^{N} \Phi(k)\Phi^T(k)\right]^{-1} \left[\sum_{k=1}^{N} \Phi(k)y(k)\right] \tag{3.78}$$

where N is the number of measurement samples, and:

$$y(k) = \begin{bmatrix} \mathbf{F}_{EG}^A(k) \\ \mathbf{M}_B^A(k) \end{bmatrix} = \begin{bmatrix} m\ddot{\mathbf{r}}(k) - \mathbf{F}_{Ext}(k) - \tilde{m}\mathbf{g} \\ J_{kite}\dot{\omega}(k) + \omega(k) \wedge J_{kite}\omega(k) - \mathbf{M}_{Ext}(k) \end{bmatrix} \tag{3.79}$$

Notice that the least square method aims at minimising the prediction error given by $\epsilon(k,\Theta) = y(k) - \Phi^T(k)\Theta$

3.9 Oehler's Model

The most recent work attempted to identify aerodynamic coefficients in the TU Delft AWE team was done by Johannes Oehler. Therefore his work and the model he developed will be taken as a reference for this project. This section then aims at giving a short summary of this model but also show the corrections, improvements and modifications brought to adapt it to the new measurement setup and bridle line design.

3.9.1 Force Balance

Compared to the 3 plate model implemented from scratch in this work, Oehler's model is based on a static analysis. Moreover the orientation of the kite is simplified by only accounting for the heading and the elevation of the kite.

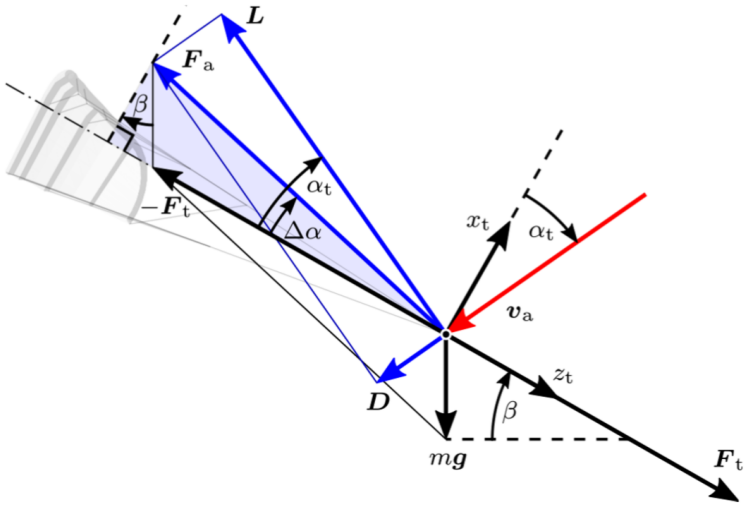

FIGURE 3.16: Force equilibrium of a kite as in Oehler's work (special case where the heading vector $\psi = 0$) [(]Oehler)

The approach to finding the lift and drag coefficient is different, in a way that Oehler reaches these values through the analysis of the angles lying between the different efforts. Using figure: 3.16 the force balance follows:

$$\begin{cases} \mathbf{F}_a + m\mathbf{g} + \mathbf{F}_t = 0 \\ \mathbf{F}_a = \mathbf{L}_{wing} + \mathbf{D}_{wing} + \mathbf{D}_{KCU} + \mathbf{D}_{sensor} \\ m\mathbf{g} = mg[-\cos\beta\cos\psi,\ \cos\beta\sin\psi,\ \sin\beta] \\ m = m_{Wing} + m_{KCU} \end{cases} \tag{3.80}$$

where β is the elevation angle and ψ the heading angle. The vector diagram also shows how the gravitational force is compensated by an upwards rotation of the aerodynamic force by an angle $\Delta\alpha$. Using the blue triangle in figure: 3.16 the following relation is found for the angle offset:

$$\tan(\Delta\alpha) = \frac{mg\cos\beta\cos\psi}{F_t + mg\sin\beta} \tag{3.81}$$

Using the angle of attack with respect to the tether α_T and the previous shift, the lift to drag ratio can be expressed as:

$$\frac{L}{D} = \cot(\alpha_T - \Delta\alpha) \tag{3.82}$$

Now the particularity of Oehler's model lies in its estimation of the difference between the angle of attack with respect to the tether α_T and the measured angle of attack α_m. Indeed the measurements are made with respect to the bridle lines, which because of the weight and drag of the KCU is miss aligned with the tether. Let's call the difference between those two angle λ_0 such that $\alpha_T = \alpha_m + \lambda_0$. Also this model accounts for the change of angle of attack due to depower, therefore the true estimation of the angle of attack $\alpha = \alpha_m - \alpha_d$ where the realtion for α_d is given in equation 3.58.

3.9.2 Estimation of the offset λ_0 between the tether angle of attack α_t and the measured angle of attack α_T

Because the geometry of the bridle line was modified compared to the kite that Oehler used for his model, some changes were brought to his model. Indeed the pigtail of the KCU was removed to connect both the rear and front bridle lines to the KCU. The new implementation however retains the main initial idea which is to find an offset that satisfies the static equilibrium in the bridle line system. An additional tweak was also brought by finding the offset not with a shooting method but with a optimisation scheme, to ensure the precision of the result. The first step comes from expressing the aerodynamic force in the front and rear bridle lines between the kite and the KCU. Using 3.80 one obtains:

$$\mathbf{F}_{a_{KITE-KCU}} = -\mathbf{F}_t - m\mathbf{g} + m_{Wing}\mathbf{g} \tag{3.83}$$

notice that since we are looking at the tension force between the KCU and the wing, some aerodynamic effort has already been "consumed" to balance the weight of the wing giving $\mathbf{F}_a = \mathbf{F}_{a_{KITE-KCU}} - m_{Wing}\mathbf{g}$. Then assuming that the aerodynamic center lies at the quarter chord, hence 75% of the load is considered to go into the front bridle lines (let's call it $\mathbf{F}_f$) and 25% in the rear bridle lines (lets' call this force $\mathbf{F}_r$). Also setting that the front bridle line angle with the normal to the chord is λ_2 one finally finds:

$$\begin{cases} \mathbf{F}_f = 0.75||\mathbf{F}_{a_{KITE-KCU}}||[\cos\lambda_2, \ -\sin\lambda_2] \\ \mathbf{F}_r = -\mathbf{F}_{a_{KITE-KCU}} - \mathbf{F}_f \end{cases} \tag{3.84}$$

Since the KCU is attached to both of these lines the drag and weight efforts acting on the KCU must be balanced by those two bridle line force giving:

$$\mathbf{F}_{Residual} = \mathbf{F}_f + \mathbf{F}_r + m_{KCU}\mathbf{g} + \mathbf{D}_{KCU} \tag{3.85}$$

where the norm of $\mathbf{F}_{Residual}$ is the objective function of minimize with respect to λ_2. Using the optimisation scheme one finds λ_2 which can be assumed as λ_0.

3.9.3 Aerodynamic coefficient estimation

Once λ_0 is estimated the lift to drag ratio is found using equation 3.82. Directly from the lift to drag coefficient comes the lift force:

$$L = F_a\sqrt{\frac{(L/D)^2}{1+(L/D)^2}} \tag{3.86}$$

and the lift coefficient is found with the relation $C_L = \frac{L}{1/2\rho_{air} v_A^2 A}$ with A the projected surface area of the kite and v_A the apparent wind velocity. The drag coefficient is found using the lift to drag ratio.

3.9.4 Comparison between Oehler's and the model developed in this thesis

	Aerodynamic centers	Influence Power-Depower on AOA	Drag KCU	Weight KCU	Inertia KCU	Weight Wing
Oehler	1 Point	✓	✓	✓	×	✓
Developed model	3 Point (3 plate model)	✓	✓	✓	✓	✓
	Inertia Wing	Tether Weight & Drag	Tether orientation	Kite Orientation	Moment Equation	
Oehler	×	×	Straight	Heading: ψ Elevation: β	×	
Developed model	✓	✓	Discrete Mass Model	Pitch:θ_P Yaw:ϕ_Y Roll:ψ_R	✓	

Chapter 4

Experimental setup and data analysis

4.1 Experimental setup

4.1.1 Sensors

The experimental system contains a variety of different sensors ranging from aerodynamic sensors to positional and orientation sensors. This section will give a general overview over the sensors in use. The acquisition of data is done at a sampling rate of $20[Hz]$.

4.1.1.1 Inertial Measurement Unit (IMU) and GPS system for positioning

Finding out the kinematic state of the kite is key to determining the aerodynamic performance. To find out about it, the experimental set up contains an IMU containing both a 3-dof accelerometer, a 3-dof gyroscope as well as a barometer and a magnetometer. The position is as well measured via GPS. Sensor fusion between the IMU's data and GPS data is then performed to provide the estimation of:

1. position $x_{EG},\ y_{EG}$ & z_{EG} (in (ENU) the earth ground reference frame)
2. altitude (in (ENU) the earth ground reference frame)
3. velocity $v_{x,EG},\ v_{y,EG}$ & $v_{z,EG}$(in (NED) the earth ground reference frame)
4. acceleration $a_{x,EG},\ a_{y,EG}$ & $a_{z,EG}$ (in (NED) the earth ground reference frame)
5. rotational rates $\phi_{YAW},;\ \theta_{PITCH}$ &ψ_{ROLL}

The IMU and GPS are both mounted onto one of the strut of the kite as shown in figure 4.2. It should also be mentioned that the strut might not be centred.

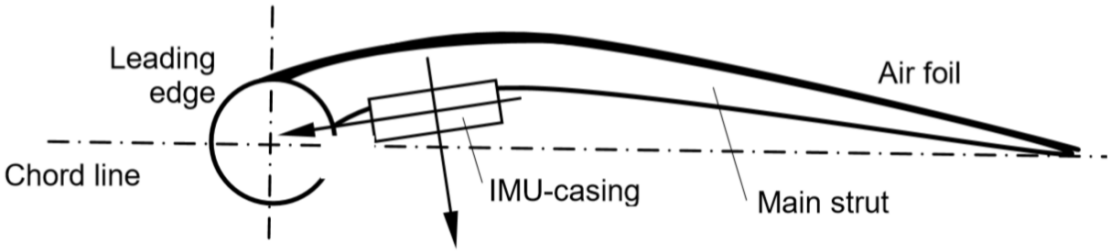

FIGURE 4.1: Positioning of the IMU

4.1.1.2 Wind measurement

The wind is measured at the ground station with an ultrasonic sensor at the end of a 6m mast. This collects information about the ground wind speed, air temperature and the wind direction with respect to the north axis, so here y_{EG}.

The apparent speed at the kite is also measured, this time using a pitot tube which is also accompanied with a wind vane to collect data about the angle of attack of the incoming flow. The measurement system is fix and attached in a "v" of the front bridle line system. Compared to Oehler [20] the pitot tube does not align with the flow. This should not bring any issue, since he had shown that the measured angle of attack would not exceed more than $20[deg]$ at which a pitot tube is still able to measure correctly the apparent wind speed. Notice that the angle of attack is measured with respect to the bridle line system, so the angle between the chord of the wing and the bridle line system is needed to use the measurements in the wing reference frame.

4.1.1.3 Depower and power measurement sensors

The steering and power values are measured from the position of the steering and power motors in the control pod using analogue potentiometers. The absolute values P^{abs} are converted into a relative steering/power values lying in the range of $\pm 100\%$ and $0 - 100\%$ using the following formulations:

$$P_S = \left(2\frac{P_S^{abs} - P_S^{min}}{P_S^{max} - P_S^{min}} - 1\right).100\% \tag{4.1}$$

for the steering settings measurements and for the power settings measurements:

$$P_P = \left(2\frac{P_P^{abs} - P_P^{min}}{P_P^{max} - P_P^{min}}\right).100\% \tag{4.2}$$

A negative steering setting corresponds to a right turn while a positive steering setting corresponds to a left turn.

4.1.1.4 Summary of the sensors

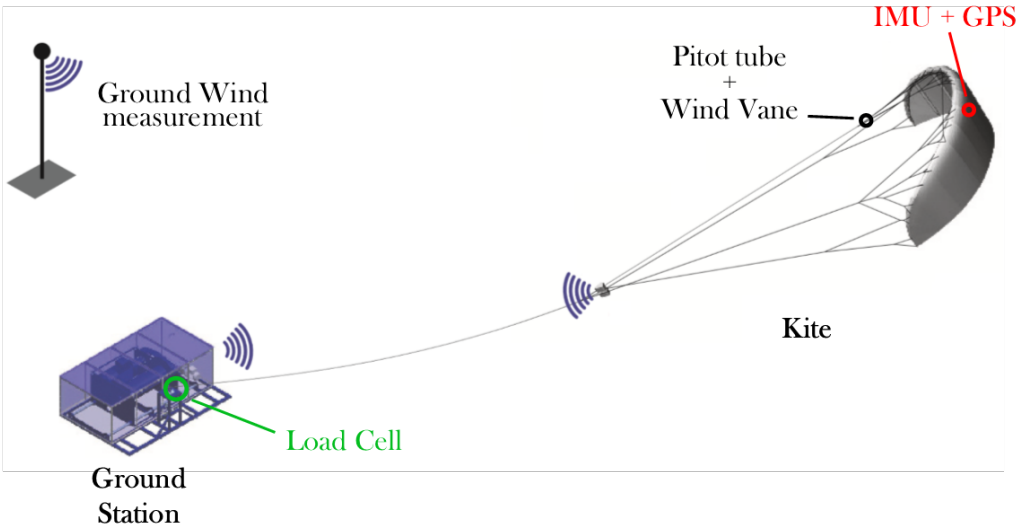

FIGURE 4.2: Positioning of the sensors, modified from [28]

Value	*Angle of Attack* α	*Apparent Wind* v_A	*Ground Wind speed*	*Ground Wind Orientation*	*Position*
Sensor	Wind vane	Pitot tube	Ultrasonic Sensor	Ultrasonic Sensor	IMU GPS
Resolution	$1[deg]$	$10^{-4}[m/s]$	$10^{-4}[m/s]$	$10^{-5}[m/s]$	$10^{-5}[m]$
Measurement Error	$\pm 0.5[deg]$	$\pm 0.2[m/s]$	$\pm 0.2[m/s]$	$\pm 0.1[deg]$	$\pm 0.1[m]$
Value	Velocity	Acceleration	Orientation ϕ_{YAW} θ_{PITCH} ψ_{ROLL}	Orientation rate $\dot{\phi}_{YAW}$ $\dot{\theta}_{PITCH}$ $\dot{\psi}_{ROLL}$	Tension
Sensor	IMU GPS	IMU GPS	IMU GPS	IMU GPS	Load Cell
Resolution	$10^{-5}[m/s]$	$10^{-5}[m/s^2]$	$10^{-5}[deg]$	$10^{-5}[deg/s]$	$10^{-4}[N]$
Measurement Error	$\pm 0.1[m/s]$	$\pm 0.1[m/s^2]$	$\pm 0.1[deg]$	$\pm 0.1[deg/s]$	$\pm 10[N]$

4.2 Experimental data

The experimental flight data has been provided by Kitepower and contains a variety of measurements namely more than 40 different variables. However no documentation nore description about the data was available, therefore the orientation of the angles, the orientation of the reference frames as well as the units and the meaning of certain values had to be determined. The methodology that was adopted to find an answer to all the unknown parameters about the data are presented as follow.

4.2.1 Data structure

The following data sets were used for this work and for the estimation of the aerodynamic parameters and are summarized in Table 4.1

Dataset	***Time length [min]***	***Wind vanes***	***Pitot tube***	***Kite Name***	***Tether diameter***	***WT***	***Bridle Geom***
2018-04-25	40	AOA & Sideslip	Self aligning with the wind	V3.25B	4 [mm]	No	Pigtail
2019-10-08	265	AOA	Fixed to the kite	V3.25B	10[mm]	Yes	Linked to KCU

TABLE 4.1: Summary of the different characteristics of each data set used for this study (WT stands for Wind Turbine)

For the oldest version of the data the KCU was attached to the front bridle line using a pigtail whilst for the most recent data both the front and rear bridle lines are attached to the KCU. A

description of the mostly used variables in this thesis is given as follow as a documentation for future studies on these datasets. Another important information about the data is that the kite was flying down loops.

4.2.1.1 Air temperature:

The air temperature or known as **airspeed_temperature** in the database is given in degrees Celsius and is the temperature measured by the pitot tube in altitude in order to get the local density.

4.2.1.2 Angle of attack: AOA

The wind speed angle of attack known as **airspeed_angle_of_attack** or **angle_of_attack** in the database is given in degrees and is measured with respect to the heading vector of the kite with a wind vane. Its positive axis of rotation is the body y axis Y_B as shown in Figure: 4.3.

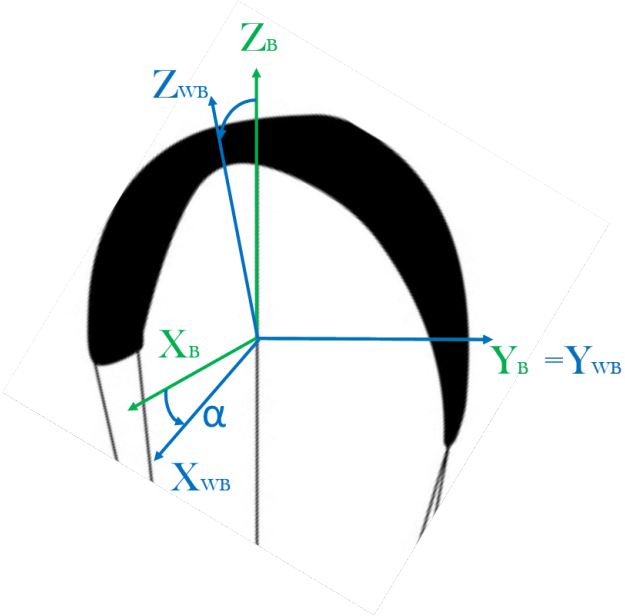

FIGURE 4.3: Definition of the angle of attack measurement with respect to ENU reference frame

4.2.1.3 Apparent wind speed:

The apparent wind speed or known as **airspeed_apparent_winspeed** or **apparent_windspeed** in the data base corresponds to the wind speed measured on-board of the kite by the pitot tube in $[m/s]$. Since this pitot tube is fixed the measurement of the apparent wind speed is in fact the projection of the wind speed onto the body x axis X_B.

4.2.1.4 Kite's position:

The kite's position is measured in $[m]$ with respect to the ground station using dual GPS, barometer and inertial sensors. The respective kite's coordinate in x,y and z axis are defined in the data base as **kite_pos_east**, **kite_pos_north** and **kite_height** .The measurement is done in the earth ground reference frame in the orientation **East-North-Up** reference frame as shown in Figure:4.4.
The kite's position can also be defined using the elevation and azimuthal angle. They are found in the database under the names, **kite_elevation** and **kite_azimuth**. These angles are however

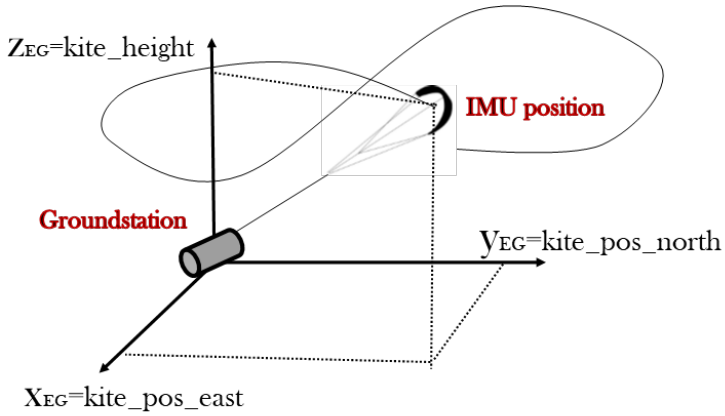

FIGURE 4.4: Kite's position measurement definition with respect to an ENU reference frame

defined in the **North-East-Down** reference frame meaning that in the **East-North-Up** reference frame the measured azimuth angle is in fact negative as shown in Figure 4.5.

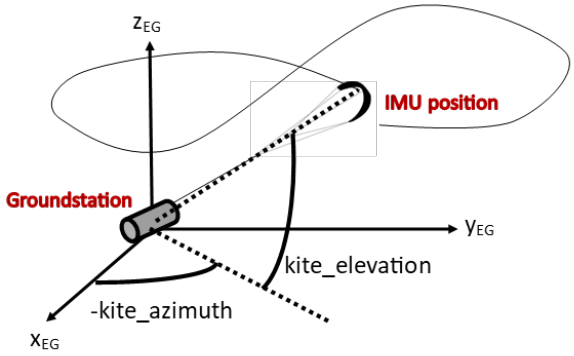

FIGURE 4.5: Kite's azimuth and elevation angle measurements definition with respect to an ENU reference frame

4.2.1.5 Kite's velocity:

The kite's velocity is estimated using a Kalman filter that extracts the position variations from the IMU and GPS positioning system. It is found in the database under the names of **kite_*_vx, kite_*_vy, kite_*_vz** with * an integer between 0 and 3. The velocity of the kite is measured in **the earth ground reference frame (EG)** in $[m/s]$. The orientation of the coordinate system in which it is measured is different from the one in which the position is measured. Indeed the measurement are made in an **North-East-Down** reference frame and not **East-North-Up** reference frame. As shown in Figure 4.6 when using the measured data in the **East-North-Up** reference frame the following correction have to be made: $v_{xENU} = v_{yNED}$, $v_{yENU} = v_{xNED}$ and $v_{zxENU} = -v_{zNED}$. This correction will be adopted along this thesis in order to have all values defined in the same orientation.

4.2.1.6 Kite's acceleration:

The kite's acceleration is estimated using a Kalman filter that extract the acceleration of the kite's from the IMU and GPS positioning system. It is found in the database under the names of **kite_*_ax, kite_*_ay, kite_*_az** with * an integer between 0 and 3. The acceleration of the

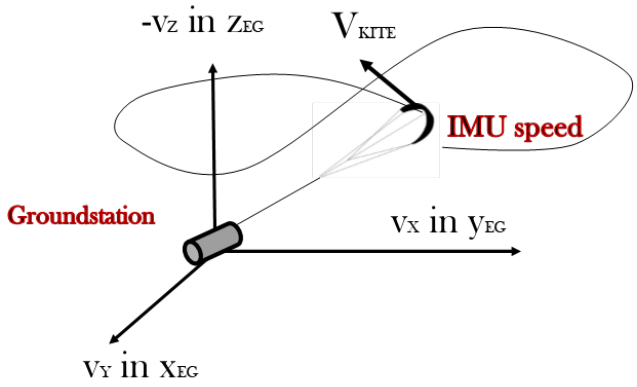

FIGURE 4.6: Kite's speed measurement definition with respect to an ENU reference frame

kite is measured in **the earth ground reference frame (EG)** in $[m^2/s]$, but just as the velocity the reference frame is different than the one chosen for the measurement of the position which also happens to be the reference frame chosen all along this work. As shown in Figure 4.7 when using the measured data in the **East-North-Up** reference frame the following correction have to be made: $a_{xENU} = a_{yNED}$, $a_{yENU} = a_{xNED}$ and $a_{zxENU} = -a_{zNED}$.

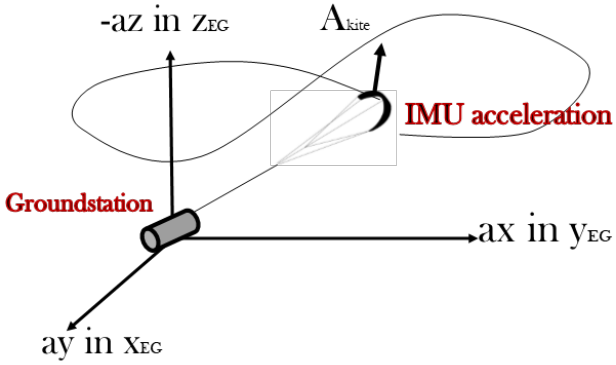

FIGURE 4.7: Kite's acceleration definition with respect to an ENU reference frame

4.2.1.7 Kite's Yaw, Pitch, Roll:

The kite's orientation is evaluated using Euler's angles in the earth ground reference frame. The three Euler angles at each time step can be found in degrees in the data set under the names: **kite_*_yaw** for the yaw angle, **kite_*_pitch** for the pitch angle and **kite_*_roll** for the roll angle. These angles are measured using the **North-East-Down** orientation therefore to convert the values into a **East-North-Up** orientation the kite's pitch and yaw must become negative and the measured roll value must remain the same. It was also noticed that the kite's yaw measurement values are shifted by $-90[deg]$ with respect to the **East-North-Up** when considering that the kite's initial heading vector is aligned with the ground earth's x axis X_{EG}. The orientation of the measurements are summarized in Figure 4.8. The methodology as well as the code used for changing of referential is presented in the next section of this chapter.

Last but not least, the measured Euler angles must be taken in the following order when estimating the rotation matrix **Yaw-Pitch-Roll**

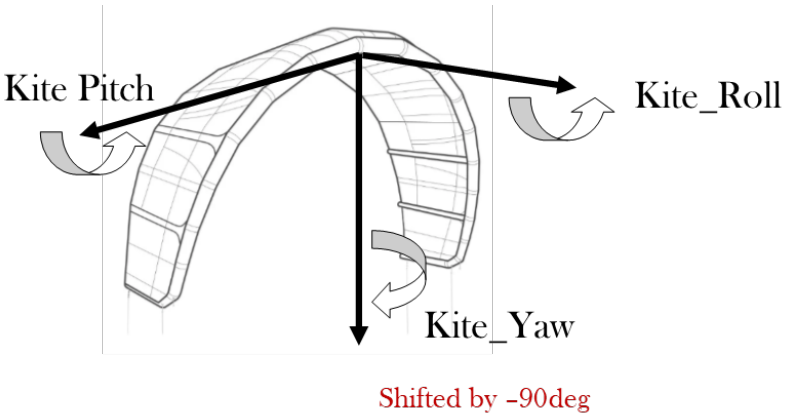

FIGURE 4.8: Kite's euler angle measurement definition with respect to an ENU reference frame

4.2.1.8 Kite's tether force:

The kite's tether force is registered in the data base under the name **ground_tether_force** and is given in **[kg]** and not in $[N]$. This force is measured at the ground station and therefore does not account for the tether's drag, or weight.

4.2.1.9 Ground wind:

The magnitude of the velocity named **ground_wind_velocity** in $[m/s]$ as well as its orientation **ground_upwind_direction** with respect to the y axis in the earth ground reference frame Y_{EG} can be found in the database. The user of the database should pay attention to the fact that the angle measurement of the wind is positive counter-clockwise, meaning that it is consistent with the z-axis in the **ENU** earth ground reference frame as shown in Figure 4.9.

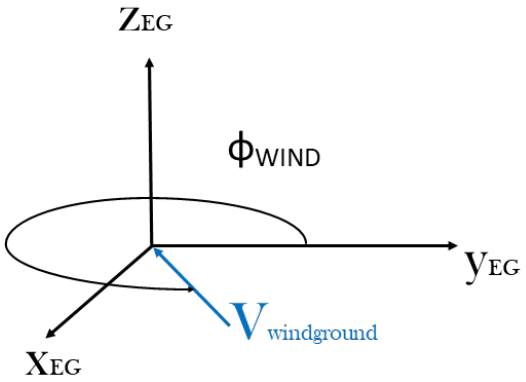

FIGURE 4.9: Ground wind measurement definition with respect to an ENU reference frame

4.2.1.10 Kite's power and depower setting:

The position of the steering and power motors in the control pod are measured by analogue potentiometers and transcribed into the data base as the power and steering settings of the wing. The resulting values can be found in the data base under the names **kite_actual_depower** for the power input and **kite_actual_steering** for the steering setting. From these values the power

setting u_p can be computed using the following formula:

$$u_p = (100 - P_P)/max(100 - P_P) \tag{4.3}$$

It should also be mentioned that **a negative steering input causes the kite to turn right while a positive input causes the kite to turn left.**

4.2.2 Flight visualisation and data check

Checking the data only with graphs might end up being complicated and tedious without talking about the great chance of making an error while checking it. Therefore a visualisation tool of the trajectory of the kite and its orientation in Blender as well as a comparison tool for the orientation of the kite have been developed to first of all determine if the orientation of the kite is correct and also if the trajectory makes sense.

4.2.2.1 Estimation of Euler angles

This tool was first of all developed to find how the Euler angles were defined since the data came with no documentation. Indeed the orientation of the Euler angles that is if they are defined positive in the counter-clockwise or clockwise direction or the sequence of order of the Euler angles were unknown. To find how these angles were defined and without having to go through all the possible permutations the following method was adopted: try to approximate the Euler angles on the base of the trajectory of the kite by considering that the kite's system is stiff enough to always be tangent to the trajectory. Therefore the heading vector of the kite is considered to always be tangent to the trajectory, and both the pitch and yaw angles of the kite can be estimated using the tangent vector. Indeed the elevation angle of the tangent vector to the trajectory is taken as the pitch angle of the kite and the azimuth angle of the tangent vector to the trajectory is taken as the yaw angle (Figure:4.10).

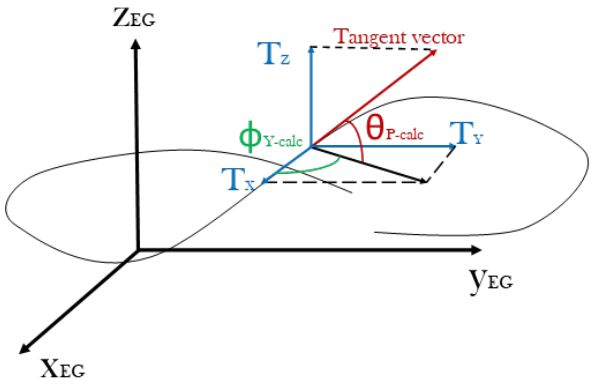

FIGURE 4.10: Estimation of the Euler angles

Hence the estimated pitch and yaw angles are computed with the following equalities:

$$\begin{cases} tan(\theta_{P-calc}) = \frac{T_z}{\sqrt{T_x^2+T_y^2}} \\ tan(\phi_{Y-calc}) = \frac{T_y}{T_x} \end{cases} \tag{4.4}$$

However an estimation for the roll angle is missing here. To find it one shall recall that the roll of the kite is actually constrained by the tether. It is then supposed that because of the tether the kite must be facing towards the ground station at all time during the flight. Therefore the roll angle is computed as follow: once the kite has been yawed and pitched using the estimated

values θ_{P-calc} and ϕ_{Y-calc} an intermediate body reference frame is found. Let's call it B'. The position vector of the the kite r is then projected onto the yz-plane of this intermediate body reference frame defined by $y_{B\prime}$ and $b_{B\prime}$. The angle between the resulting projection and the y axis is then taken as the estimation of the roll, because it corresponds to the angle that the intermediate body frame has to be rolled to be facing the ground station whilst the kite's heading vector x_B is aligned with the tangent vector. The process is summarized as follow: First of all, the intermediate reference frame is estimated using the rotation matrix previously defined: $(\mathbf{x_{B\prime}}, \mathbf{y_{B\prime}}, \mathbf{z_{B\prime}}) = R_{EG-B}(\phi_{Y-calc}, \theta_{P-calc}, 0)$, then the position vector of the kite is projected into the intermediate reference frame and is expressed as such $\mathbf{r}_{xByB\prime} =< R_{EG-B}(\phi_{Y-calc}, \theta_{P-calc}, 0)\mathbf{r}, \mathbf{x_{B\prime}} > \mathbf{x_{B\prime}} + < R_{EG-B}(\phi_{Y-calc}, \theta_{P-calc}, 0)\mathbf{r}, \mathbf{y_{B\prime}} > \mathbf{y_{B\prime}}$ with $<,>$ the dot product. Finally the estimated roll angle is computed as: $\psi_R = arctan(< \mathbf{r}_{xByB\prime}, \mathbf{y_{B\prime}} > / < \mathbf{r}_{xByB\prime}, \mathbf{z_{B\prime}} >)$. Once the estimated angles were computed different combinations of the measured angles were done to see whether each one of them was defined clockwise or counter-clockwise with respect to the **ENU** orientation. Then once the shape were starting to look similar a shift in the data was estimated for the yaw using a least square problem. This is how the orientation and shift of the kite's yaw, pitch and roll were estimated.

4.2.2.2 Visualization of the kite's flight in Blender

To further check the data and verify if the Python code was valid another visualisation tool was developed but this time in Blender. This visualization tool not only enables for checking if the kite's trajectory and orientation both make sense such as in Figure 4.11, in which the take of, reel out and reel in phases are visible. Two key characteristic to check if the data is correctly interpreted is whether the kite is pointing towards the sky right before take off, and whether the kite is always facing towards the ground station. This tool also helps to further compare the estimated Euler angles and the measured ones (Figure 4.13) and the results that were found will be discussed in the next section of this chapter.

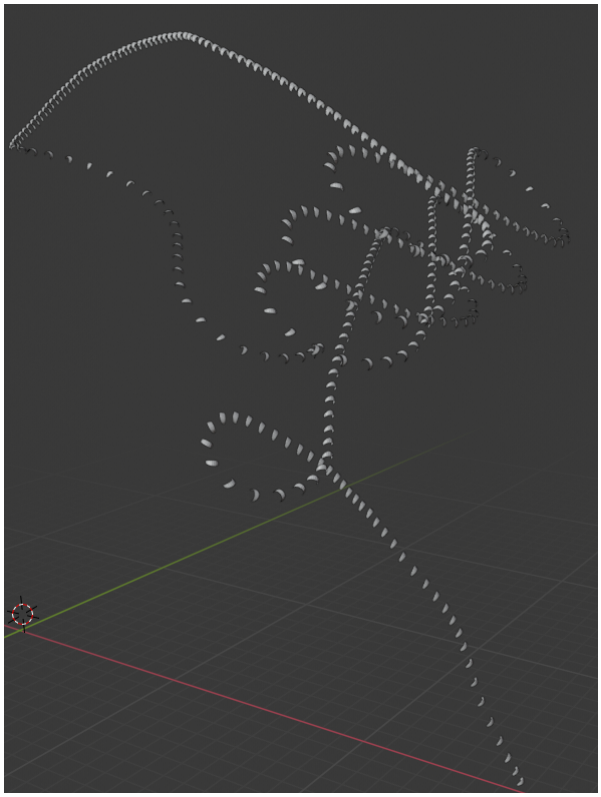

FIGURE 4.11: Visualisation of the kite's orientation and trajectory

4.3 Data analysis

4.3.1 Results of the estimation of the kite's Euler angles

Some early conclusions were found with this method as shown in Figure 4.12. It should be mentioned that the kite is making a right turn (green in Figure 4.12) when the kite's yaw goes from negative to positive and left turn (red in Figure 4.12) when the kite's yaw goes from positive to negative. First of all the estimated results are close to the measured ones except for the reel in phase and sharp turns. This makes sense since the kite is depowered during reel in, the system is less "stiff" and the kite has much more freedom in its flight. The predicted Euler angles also seem overestimate the measured angles, this seems logical since the real system is not constrained by the trajectory and can go loose with respect to it. An overshoot seen in the roll measurement with respect to the estimated roll happens during a turn. This comes from the outward swing of the KCU during a turn and will be investigated later on with a simple model (shown with the red circles in Figure 4.12).

4.3.2 Results of the analysis of the trajectory and orientation in Blender

Several flight characteristics can be observed in Figure 4.13. The first one is that during straight up flight the pitch angle is higher than the one imposed by the trajectory. Also during straight up flight a side slip angle is visible. This side slip angle allows for an increased angle of attack at the side of the kite facing towards the sky. This increase of angle of attack allows for an increase of the lift force generated by this side, which in the end should balance the weight force due to the kite's mass. Another effect observed is the latency of the kite to subject itself to the trajectory when initiating a turn this is when the estimated and measured yaw angles differ the most. Another interesting observation is that the kite is rolling less inward during a turn when measured than when estimated. The hypothesis explaining some rolling inward during a turn is that the inertial force of KCU during a turn should be balanced by the lift generated by the upper part of the wing hence a need for rolling in or shifting of the bridle line system or both.

4.3.3 Influence of the KCU on the kite's rolling behaviour: the role of the roll

4.3.3.1 First reasoning and potential explanation

One characteristic of the studied system that stands out compared to other AWE systems is that the control unit of the kite is kept on-board and not on the ground. Therefore this mass is carried around by the kite during crosswind manoeuvres and is then subject to inertial effects due to trajectory changes. The consequence of these inertial effects have for the moment not been studied, however a certain intuition of these effects on the kite's flight behaviour can be developed. Indeed since the KCU is linked to the ground station and to the kite with a rope system (bridle line and tether), one can expect the entire rope system to get out of its initial alignment when such an inertial side force is applied. Since a rope's resistance to bending is assumed null, a deflection appears in the chord's profile when a side effort is applied until the side force generated by the deflection of the chord's tension is enough to balance the side effort. Therefore one would expect the KCU to swing outwards during a turn. But how does this deflection or outwards swing affects the kite system? Since the kite is fully powered during crosswind manoeuvres the bridle line and the wing can be considered as a single rigid body, therefore an outward swing of the KCU due to inertial efforts should then force the kite to roll inwards as illustrated in 4.15. A first confirmation of this hypothesis can be found in the literature, indeed Lukas Braun [6] already noticed this effect in

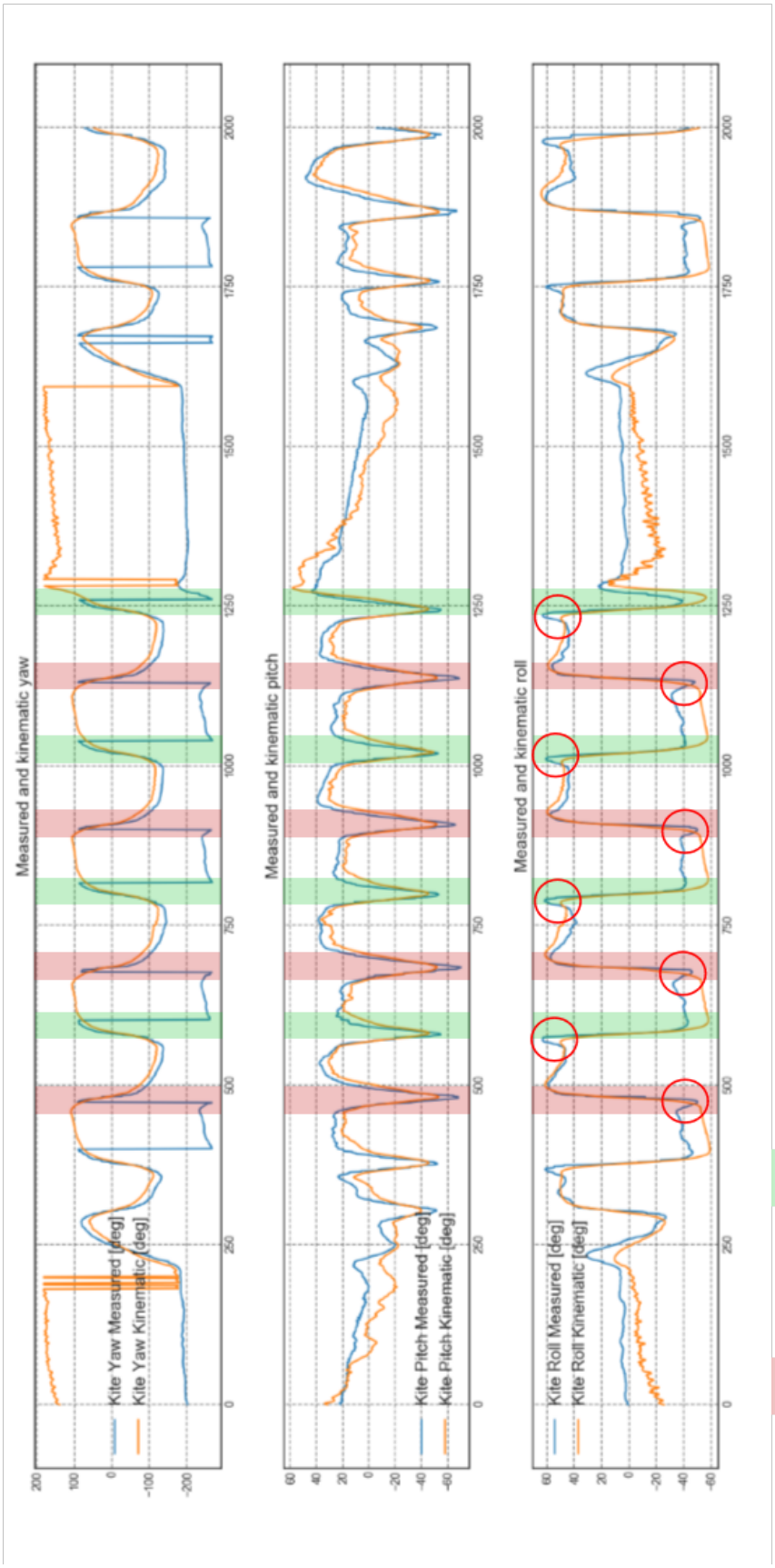

FIGURE 4.12: Comparison between the estimated and measured Euler angles

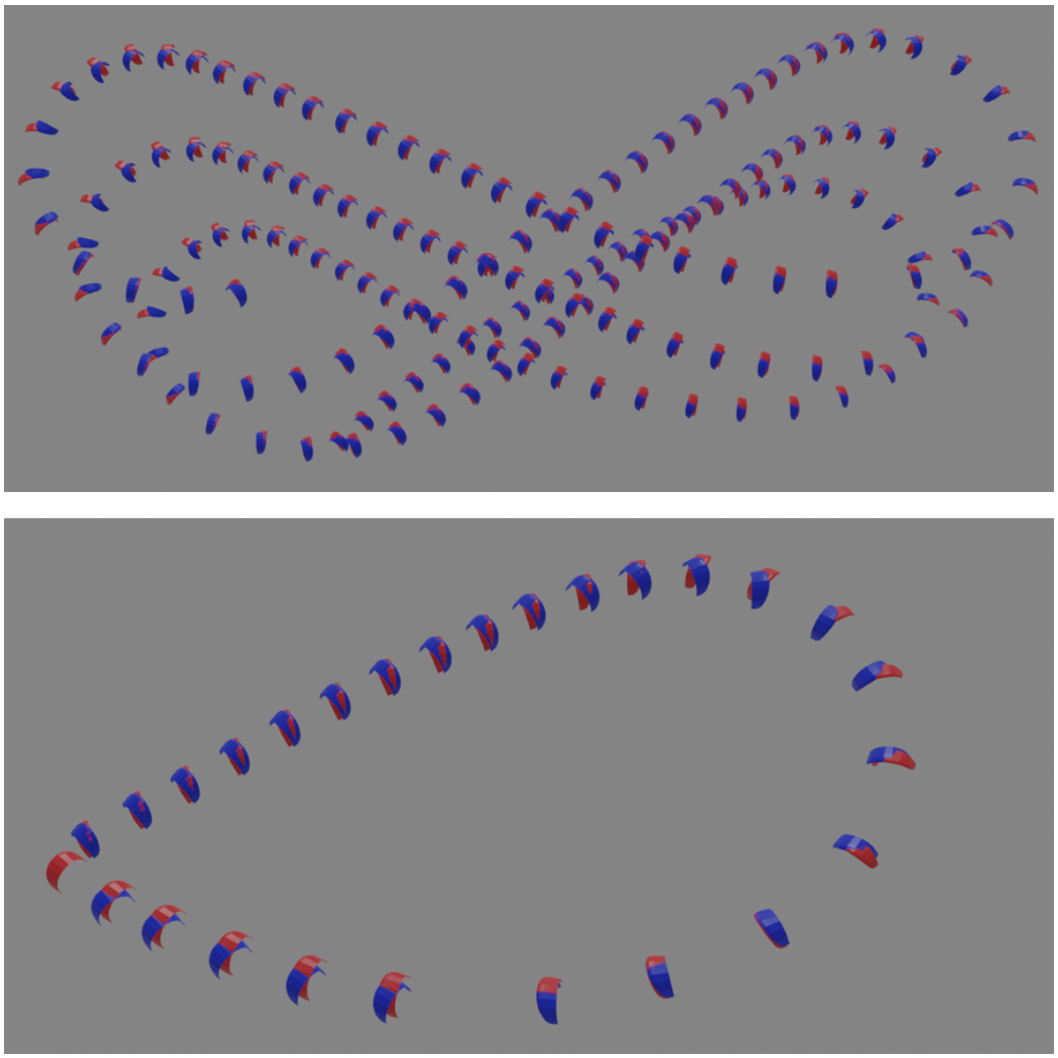

FIGURE 4.13: Measured (blue kite) and estimated (red kite) Euler angles comparison in Blender

the flight pattern of a kite with an on board KCU as shown in Figure 4.14. A further attempt to verify the validity of such a hypothesis using a simple model and flight data will be made.

Since the roll of the kite is measured by a KCU placed on-board of the wing this section aims at creating a simple model that could explain an induced roll of the kite due to the inertial effects acting on the KCU and compare the results of this model with the measured roll.

4.3.3.2 Simplification of the problem, hypothesis made and modelling

A simplification of the system is first of all needed for the description of this phenomenon that can prove to be complex if all parameters are taken into account. Following the discussion in the previous section some hypothesis are made:

1. The kite assembly (wing, bridle line and KCU) is considered as a single rigid body that rolls under the influence of the kite's inertia and weight forces.

2. The problem is considered as planar, since the deformation of the tether always stays in the plane that is tangential to the resulting effort applied at the KCU.

(a) (b)

FIGURE 4.14: Real life illustration of the pendulum effect (Genetrix Hydra $14m^2$ Kite) [6]

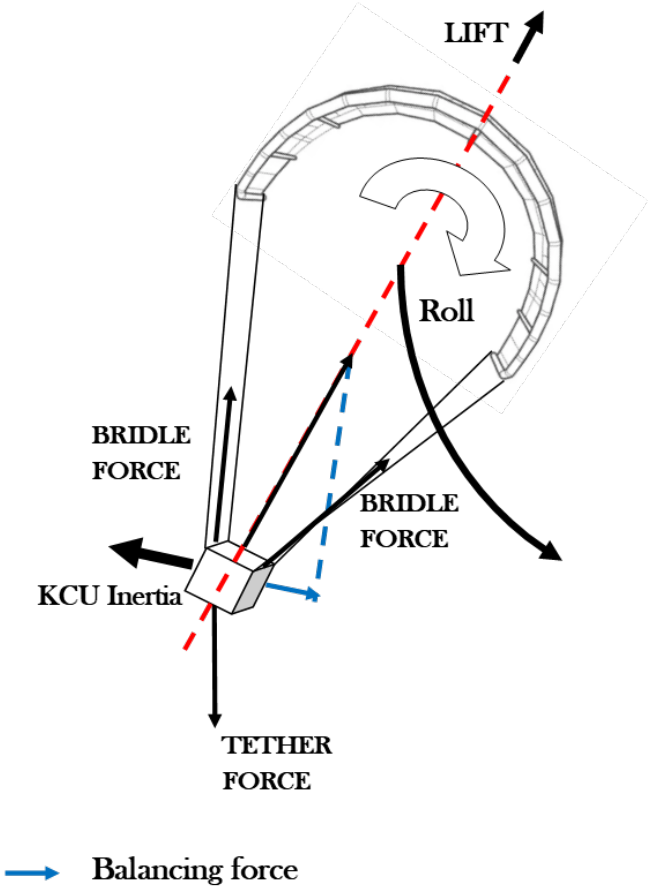

FIGURE 4.15: Illustration of the induced rolling of the kite due to KCU's inertia during a left turn

3. No tether sagging due to aerodynamic drag or weight is considered. Therefore the tether is assumed to be straight when no forces are exerted by the KCU.

4. The rolling behaviour does not influence the aerodynamic characteristics of the wing.

5. Since the inertial force of the KCU can be extracted from the data the problem the inertia is considered as a time varying force.

Also since the acceleration as well as the position of the kite is measured with respect to the ground station the trajectory of the KCU with respect to time can be estimated using the rigid assumption. This then gives access to the KCU's acceleration and so to the inertial efforts acting on it at all time. The tether tension at the ground station is also provided at all time step. Therefore the model that is looked for is a function that will try to link the measured efforts with the measured roll angle. This then leads to the following model 4.16 where $F_I[N]$ is the inertial force of the KCU

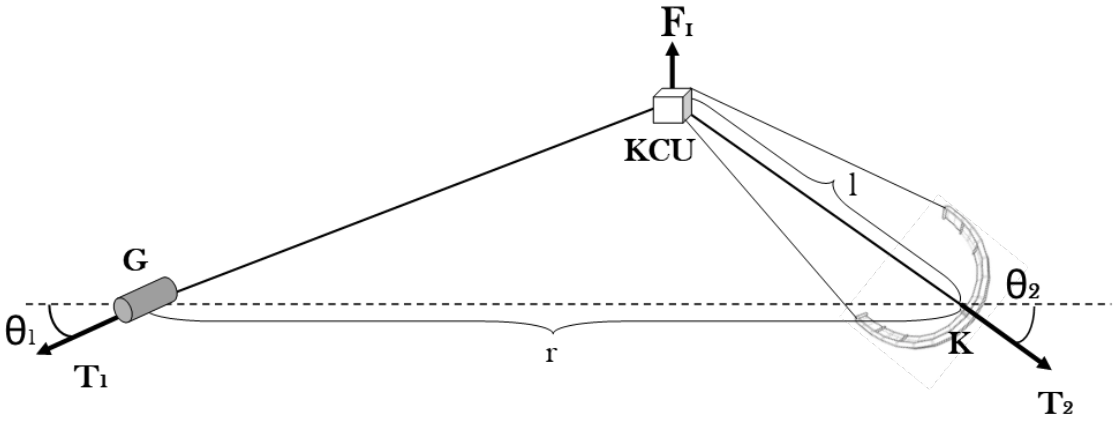

FIGURE 4.16: Model representation of induced roll due to a KCU's inertia

which takes into account both the acceleration due to gravity and the acceleration due to a change in the trajectory, $T_2[N]$ and $T_1[N]$ are the tensions at both ends of the tether, θ_1 and θ_2 are the deflection angles at both ends of the tether due to the inertial force of the KCU, $l = 11[m]$ is the IMU's distance to the ground station, r is the distance between the KCU and the IMU and finally point K,KCU and G respectively represent the kite, the KCU and the ground station. The main unknown of this problem that is looked for is the angle of the kite system θ_2 and the derivation of an expression for this unknown will be presented next. Since the problem is quasi static the force equilibrium in both x and y axis and the torque equilibrium in point K give the following system of equations in the tether reference frame:

$$\begin{cases} \sum F_x & T_1 sin(\theta_1) + T_2 sin(\theta_2) = F_I \\ \sum F_y & T_1 cos(\theta_1) = T_2 cos(\theta_2) \\ \sum M_K & T_1 sin(\theta_1) r = F_I cos(\theta_2) l \end{cases}$$

and with the introduction of a change of variable such that $cos(\theta_1) = X_1$ and $cos(\theta_2) = X_2$ the system becomes:

$$\begin{cases} T_1\sqrt{1 - X_1^2} + T_2\sqrt{1 - X_2^2} = F_I \ (*) \\ T_1 X_1 = T_2 X_2 \ (**) \\ T_1\sqrt{1 - X_1^2} r = F_I X_2 l \ (***) \end{cases}$$

After squaring and isolating X_2 equation (***) gives:

$$X_2^2 = \left(\frac{T_1 r}{F_I l}\right)^2 (1 - X_1^2) \tag{4.5}$$

Using equation (**) an expression for T_2 is found $T_2 = \frac{X_1 T_1}{X_2}$ and injected into equation (*) and gives;

$$X_2\sqrt{1-X_1^2} + X_1\sqrt{1-X_2^2} = \frac{F_I X_2}{T_1} \tag{4.6}$$

The equation 4.5 gives the following expression $\sqrt{1-X_1^2} = \frac{F_I X_2 l}{T_1 r}$ which is then injected into 4.6 and gives:

$$X_2^2\frac{F_I l}{T_1 r} - \frac{F_I X_2}{T_1} = X_1\sqrt{1-X_2^2} \tag{4.7}$$

And after squaring and some manipulation gives:

$$X_1^2 = \frac{X_2^2}{1-X_2^2}\left(\frac{F_I}{T_1}\right)^2\left(\frac{X_2 l}{r} - 1\right) \tag{4.8}$$

Replacing X_1 in equation 4.5 using equation 4.8 and expanding the expression finally gives a polynomial expression of X_2 function of known parameters:

$$\left(\frac{2r}{l}\right)X_2^3 - \left(\left(\frac{T_1 r}{F_I l}\right)^2 + \left(\frac{r}{l}\right)^2 + 1\right)X_2^2 + \left(\frac{T_1 r}{F_I l}\right)^2 = 0 \tag{4.9}$$

The three roots of this polynomial equation are found numerically using python. One of them will be a complex root which since it does not ave any physical meaning, will not be considered. The two other roots correspond to both realistic equilibrium angles. However one key characteristic that is not taken into account by the model and will help select the correct root is the constraint imposed by the tether on the KCU. Indeed one of the two valid root gives an angle that violates this constraint and lets the KCU be above the kite meaning that on Figure: 4.16 the KCU would end up to the right of the kite. This configuration respects the force equilibrium but breaches the constraint imposed by the tether, therefore the root that gives the minimum equilibrium angle should then be taken and corresponds to the estimation of θ_2. θ_1 is then computed using 4.6 and T_2 using $T_2 = \frac{X_1 T_1}{X_2}$

4.3.3.3 Estimation of the KCU's inertial force and weight

The inertial force of the KCU is used in previous equations however no method has been given yet to estimate it, and this section will try to remedy to this. Using the rigid body hypothesis, the KCU's trajectory can be estimated with the measurements. Indeed the orientation of the wing (yaw,pitch and roll angles) is known at all time as well as its position. Since the length and position of the KCU are assumed to be constant with respect to the wing (l=11[m] distance between IMU and KCU) the trajectory of the KCU is computed at all time, and by differentiating it twice with respect to time the acceleration due to the trajectory of the kite is then known. However as it is known, differentiation amplifies high frequency noise, therefore a low pass filter is used on the data before and after the first differentiation to get rid of high frequency noise. The resulting acceleration ends up being close to the one measured by the IMU, to a point where it could be used instead of the computed KCU's acceleration. Not all of the inertial efforts generated by the KCU participates into the deformation of the tether which will in the end induce a roll, only the component that is in the local $y_B z_B$ plane as well as normal to the tether does. Therefore the inertial component of the F_I force defined in the previous model writes:

$$\mathbf{F_I} = ||\mathbf{F_{IB}^{y_B z_B}} - < \mathbf{F_{IB}^{y_b z_b}}, \mathbf{e}_{tether} > ||\mathbf{e}_{tether} + \mathbf{W}_{KCU} \tag{4.10}$$

with W_{KCU} the gravitational force on the KCU that contributes to the induced roll which corresponds to the gravitational force projected onto the $y_B z_B$ plane and perpendicular to the tether

$\mathbf{W_{KCU}} = m_{kcu} < \mathbf{g}_B^{y_B z_B}, \mathbf{e}_t ether > \mathbf{e}_{tether}$. Also $\mathbf{e}_{tether}$ stands for the vector that is tangential to the tether, $\mathbf{g}_B^{y_B z_B}$ is the gravitational acceleration in the body reference frame and $\mathbf{F_{IB}^{y_B z_B}} = m_{KCU}\mathbf{a}_{KCU}$ is the inertial effort on the KCU in the body reference frame and projected onto the $yBzB$ plane. One should also notice that the effect of the weight on the roll induced by the KCU depends on the trajectory and orientation of the kite, and that this is taken into account by projecting the gravitational acceleration into the body reference frame.

4.3.3.4 Estimation of the roll in the tether reference frame

As mentioned before the estimated roll given by θ_2 is defined with respect to the tether reference frame. However the measured roll is expressed in the earth ground reference frame and needs therefore to be converted into the tether reference frame. The following method is applied to do just so. First the transformation matrix from the body reference frame into the tether reference frame $R_{B-Tether}$ is derived:

$$\begin{cases} R_{B-Tether} = R_{EG-Tether} R_{B-EG} \\ R_{B-EG} = (R_{ROLL}(\psi_R).R_{PITCH}(\theta_P).R_{YAW}(\phi_Y))^T \\ R_{EG-Tether} = R_{ROLL}(\pi/2 - \theta_{ELEVATION}).R_{PITCH}(0).R_{YAW}(\pi/2 - \phi_{AZIMUTH}) \end{cases}$$

where $\theta_{ELEVATION}$ is the measured elevation angle defined and $\phi_{AZIMUTH}$ is the measured azimuth angle Both angles are defined in the NED orientation earth ground reference frame. For all angles equal to zero the kite is pointing in the x_{EG} direction and its z-axis is in the z_{EG} direction. From the resulting transformation matrix the yaw, pitch and roll angles defined in the tether reference frame are computed from three components of the transformation matrix as follow:

$$\begin{cases} sin(\theta_{P-Tether}) = -R_{B-Tether}(3,1) \\ cos(\phi_{Y-Tether}) = R_{B-Tether}(2,1)/cos(\theta_{P-Tether}) \\ sin(\psi_{R-Tether}) = R_{B-Tether}(3,2)/cos(\theta_{P-Tether}) \end{cases}$$

where $R_{B-Tether}(i,j)$ designates the component of $R_{B-Tether}$ in line i and column j.

4.3.3.5 Model results

The model is implemented in python and the measurements are used for estimating the inertial force and hence the roll of the kite. The results speak for themselves (Figure: 4.17), the estimated roll using the previously presented model correlates with the measured roll except for the persistent shift that lies between the estimated and measured signals. First of all the positions of peaks between the measured and estimated roll during turns match. This then means that the abrupt changes measured in roll during a turn would then be coming from the inertial efforts of the KCU as described by the model. Another similarity between the measured and estimated roll lies in the straight flights between a right and a left turn, where a plateau in the roll due to the gravitational effect of the KCU is observed in both measured and estimated signals (circled in red in Figure: 4.17). Indeed when flying along a straight path of the figure of eight the gravitational effects on the KCU will have a tendency to impose a roll in the same direction as the roll observed during the previous turn, creating an hysteresis effect where the roll does not go back to zero right after a turn. This then comforts the hypothesis that the gravitational and inertial efforts imposed by the KCU on the kite are one of the main sources of roll. One should also notice that the similarities observed only hold for the powered flights during reel out phases, which makes sense since the kite is mainly flying turns and generating inertial and gravitational efforts into the $y_B z_B$ plane during reel out and not reel in phases.

FIGURE 4.17: Roll prediction: the kite is rolled onto its right side when the roll angle is positive and to its left side when the roll angle is defined negatively. The green band corresponds to a left turn followed by the straight flight leading to the next right turn. The red band corresponds to a right turn followed by the straight flight leading to the next left turn

It is now clear that the roll of the kite is mainly caused by the inertial forces of the KCU, but does this have any impact on the performance of the system? Using the previously developed model the difference between the tether tension at the kite and the tether tension at the ground station is computed. This then gives the amount of pulling force lost and used for balancing the inertial effects. The following results are found in Figure: 4.18.The most significant difference between the two tensions happens during a turn and corresponds to the peaks in Figure: 4.18. This difference peaks at values ranging from 40 [N] to 80 [N] which is an order two smaller than the total tether tension, making the direct effects of the KCU on the pulling force negligible. One can expect this effect to be even more negligible for an increase of the tether tension and therefore of the kite's size. Now this gives the direct effect of the inertia of the KCU on the pulling force but it does not account for any of the possible changes in the aerodynamic that could cause such a roll of a kite.

However this still does not provide an explanation to why such an offset exists between the estimated and measured signals. The answer probably lies in the asymmetry of the measured roll, since the kite seems to maintain a positive roll throughout most of the flight. As shown in Figure: 4.17 the roll peaks into the negative values during a left turn to then go back up into positive values, when it is expected to remain negative because of the gravitational effect. The consequence is that the plateau that is expected to remain in negative roll values after a left turn is now found in the positive values. This would then mean that the system remains in equilibrium when no inertial effects are applied to it when the roll angle is positive. But why? Does this come from an asymmetry of the steering, power or reel out speed signal between the right and the left turns? Could it be an asymmetry of the bridle line system which could then impose an asymmetrical loading onto the kite? After inspection no asymmetry in the power and reel out signals were found, however some asymmetry was found in the steering signal as shown in Figure:

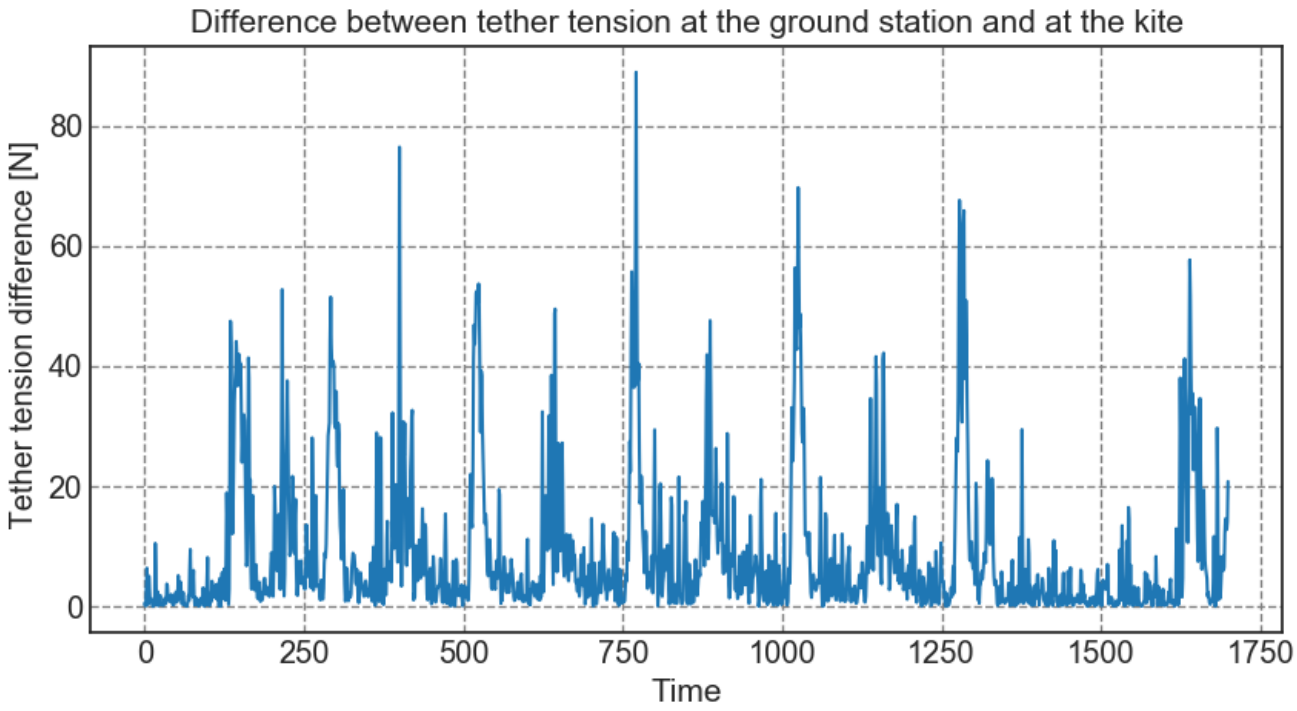

FIGURE 4.18: Illustration of the force lost in the balance of the inertial effects due to the KCU

4.19. Indeed the steering remains activated to the right during the straight section of the flight after a right turn but does not remain activated during the straight flight that follows a left turn and is set back zero by the controller (highlighted in red in Figure: 4.19). Also the kite seems to continue to yaw left after a left turn even if the steering input is not activated (the difference is highlighted in black in Figure: 4.19). This then confirms that the kite has an asymmetrical behaviour and has a tendency to turn left when no steering is activated. Recalling the skewing process of a kite for turning discovered by [7], the kite is yawed when a differential pulling is applied onto the sides of the kite when a yaw to the left is wanted the left and vice versa for a right turn. From the observations, the kite has a tendency to yaw left therefore one could then believe that the bridle line system presents an asymmetry which leads to an asymmetrical loading that imposes a higher loading onto the left than onto the right side. This asymmetrical loading would then skew the kite making the entire system yaw to the left.

However this does not explain why an unbalanced bridle line system directing more efforts onto the left side would make the kite roll to the right as observed in the measurement and create the shift observed into the data. The following static model (Figure: 4.20) might bring light onto the influence of an asymmetry of the bridle line system onto the roll when the kite is in equilibrium. Supposing that the kite's bridle system and wing are stiff enough to be considered as a single solid body, the angle θ_G between the two bridle lines is considered as constant. It is also supposed that the left bridle line force F_L is proportionally linked to the right bridle line force F_R with the coefficient x_p, which then allows for the introduction of an uneven force distribution in the bridle line system. It is also assumed that the bridle line system can be approximated using two

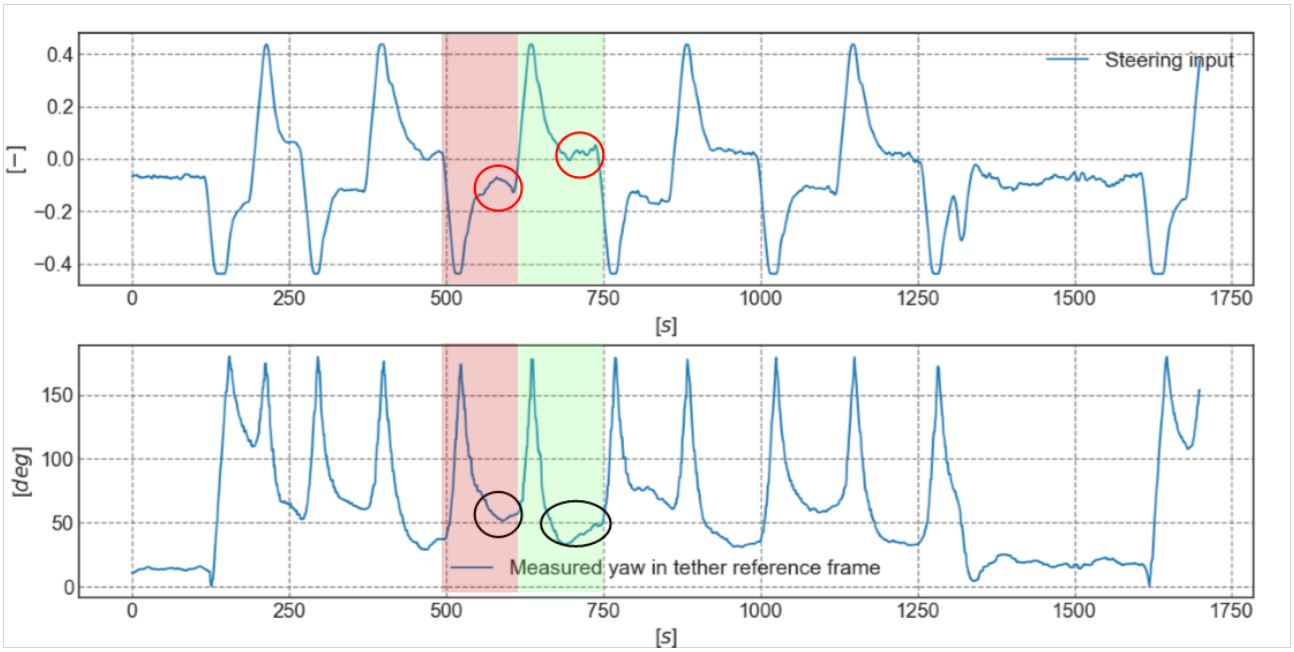

FIGURE 4.19: Illustration of the asymmetry in the steering input and measured yaw in the local reference frame. As usual the green segment corresponds to a left turn and the red one to a right turn

lines only. The following system of equation is then drawn when imposing a force equilibrium:

$$\begin{cases} F_R cos(\theta_R) = F_L cos(\theta_L)\ (*) \\ F_R sin(\theta_R) + F_L sin(\theta_2) = F_T\ (**) \\ F_L = x_p F_R\ (***) \\ \theta_L + \theta_R + \theta_g = \pi\ (****) \end{cases}$$

Replacing θ_L with equation (****) and F_L with equation (***) in equation (*), and after expansion the following equation is found:

$$cos(\theta_R) = x_p(cos(\pi - \theta_g)cos(\theta_R) + sin(\pi - \theta_g)sin(\theta_R)) \tag{4.11}$$

After replacing $sin(\theta_R) = \sqrt{1 - cos(\theta_R)^2}$ in 4.20 and some development the following expression is found for the right angle:

$$\cos(\theta_R) = \frac{x_p sin(\pi - \theta_g)}{\sqrt{-2x_p cos(\pi - \theta_g) + x_p^2 cos(\pi - \theta_g)^2 + x_p^2 sin(\pi - \theta_g)^2}} \tag{4.12}$$

and for the right force:

$$F_R = \frac{F_T}{sin(\theta_R) + x_p sin(\pi - \theta_g - \theta_R)} \tag{4.13}$$

the constant value of is computed using the width and height of the bridle line system and is equal to 64 [deg]. Looking back to Figure: 4.17 the shift that is supposedly imposed by an asymmetry in the bridle line system is computed by subtracting to the measured roll the estimated roll and averaging the value of the resulting signal over time. This finally gives an average shift of 7 $[deg]$. Using equation 4.12 the induced roll due to the uneven distribution of forces in the bridle line

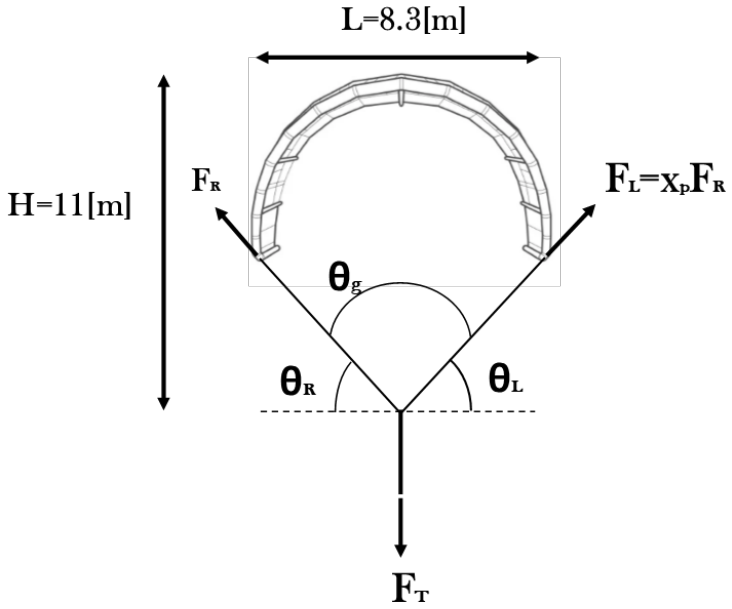

FIGURE 4.20: Model for the estimation of the roll due to the asymmetry of a bridle line system

system is found with $\psi_{ASYM} = \theta_g/2 - \theta_R$ for a given force disparity given by x_p. Therefore the magnitude of the roll induced by uneven force distribution in the bridle line function of the magnitude of this disparity modelled by the coefficient x_p is drawn in Figure: 4.21. It is then found that an increase in the effort in the left bridle line causes the kite to roll onto its right side. Analysing the second equation in 4.3.3.5 could have given the same prediction. Indeed when looking at $F_R cos(\theta_R) = F_L cos(\theta_L)$ to maintain the equilibrium and so the validity of this equation if F_L increases $cos(\theta_L)$ has to decrease so θ_L has to increase, which then means that the kite will roll onto its right side. Figure: 4.21 shows that the left force F_L has to be 1.78 times higher than the right force F_R for a shift of 7 [deg] in the roll angle as seen in the measured signal. This difference is too significant to take this answer seriously and consider the presented model as valid, even when considering an asymmetry only in the steering bridle line which is only accountable for 20% of the bridle line loads. The incoherence in the answer will most certainly come from the oversimplification of the bridle line system, which in reality carries several forks which would then split the total effort for the steering and or the load asymmetry seen by the previous model. It is still believed that a certain asymmetry in the loading will generate a roll and a yaw however the modelling of the coupled interactions of the efforts in the bridle line system and the aerodynamic distribution on the wing is complex and not all the data is available and will therefore not be undertaken. It is suggested for future work to install load cells in the bridle line system to study this asymmetry effect, and also to extract using CFD the aerodynamic load distribution to see how much effort is needed in the asymmetry to make the kite yaw and roll.

Finally a study of the influence of the mass of the KCU on the roll of the kite system was performed. The same computation process was adopted but with a change in mass. It is already known that the effect on the pulling force are and will probably remain negligible, however it was thought that this could prove handy for control theory and design of a system especially for the stability of the kite during a turn. Therefore the maximum roll angle during a turn, function of the mass of the KCU was studied (Figure: 4.22). The relation is clear, the roll will increase with an increase of the mass, this effect is however non linear. What is surprising is the amount of roll

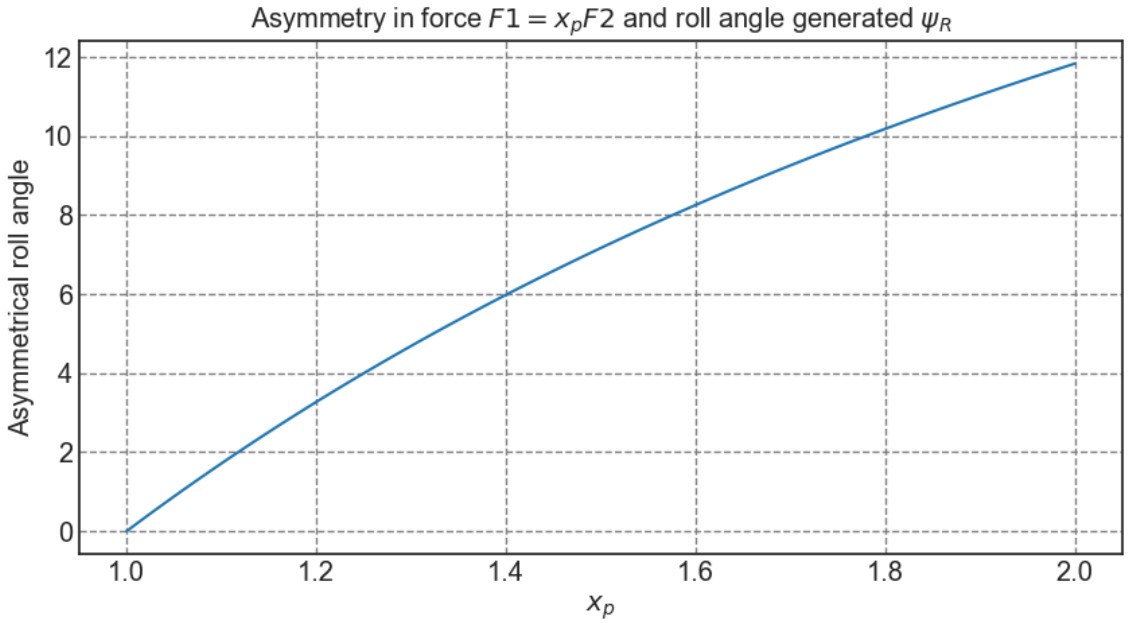

FIGURE 4.21: Relation between angle roll induced angle and asymmetry of the bridle forces

that is generated by a 20[kg] for a consequent tension which on average is 10 times bigger than the inertial effect, meaning that regardless of how small the effort is relative to the tension it will probably end up having an effect of the orientation of the kite.

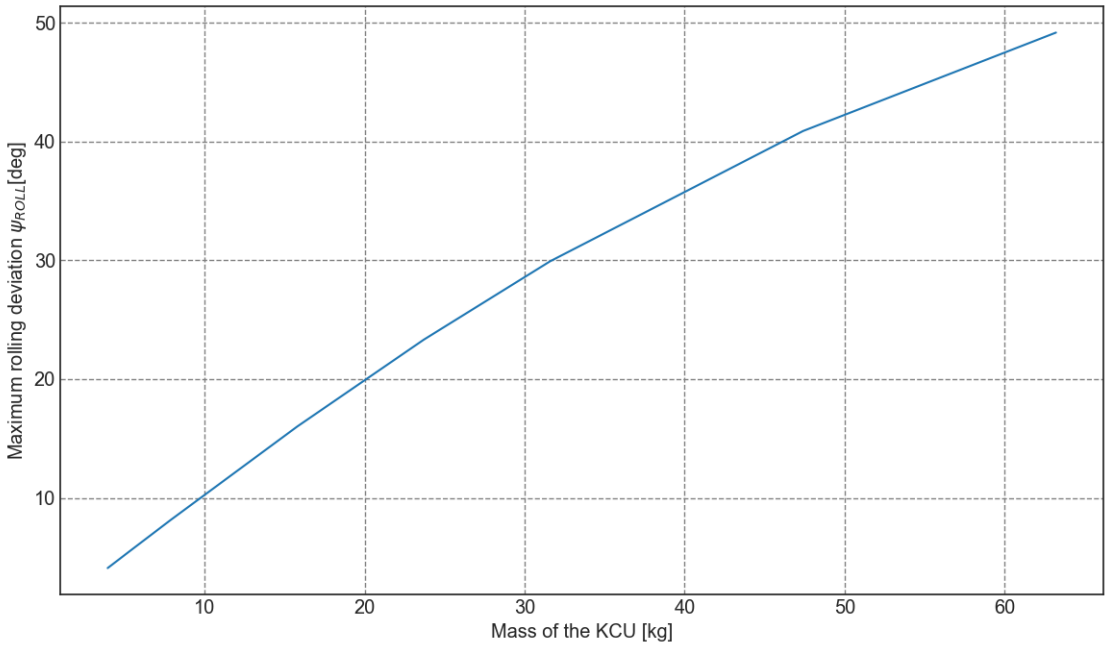

FIGURE 4.22: Roll of the kite with respect to a change in mass of the KCU (the weight of the studied KCU was 22 [kg])

In conclusion the roll mainly comes from the inertial force of the KCU, swinging outwards the kite assembly during a turn, but it also comes from an asymmetry of the system, however further investigation on this topic is needed.

4.3.4 Dimensional analysis

Before jumping into modelling the entire system, it was thought that mapping the different efforts applying on the kite for different flight configurations would prove useful to then identify which ones are predominant or negligible. Therefore the following efforts where analysed:

1. The tether tension from the measurements.
2. The tether drag, the values come from the discrete multi mass model.
3. The KCU's drag that was evaluated using the measured trajectory and orientation of the kite. Using a rigid body hypothesis the trajectory of the KCU is estimated at each time step and derived with respect to time to get the KCU's speed. The projected area of the KCU accounting for the wind turbine is $A_{KCU} = 1.6[m^2]$ The KCU assembly is considered as a blunt body so its drag coefficient is taken as $C_{D,KCU} = 1$.
4. The KCU's inertial force. The same process is adopted for the evaluation of its speed. The mass of the KCU is taken as $16[kg]$.
5. The wing's inertia where the values come from the measurements of the acceleration. The mass of the wing is taken as $12[kg]$.
6. The tether's weight.
7. The KCU's weight.
8. The wing's weight.

The analysis of these forces was made on three different sections of the flight (straight flight figure: 4.23, left turn figure: 4.25, right turn figure: 4.24) always in the powered setting. The filtering was done using empirical filters based on the values of the power and steering inputs (Right steering mask: $u_s < -0.08$, Left steering mask: $u_s > 0.05$, Straight flight $u_s > -0.08 \& u_s < 0.05$). One of the main result is that the tension in the tether is the most dominant force contribution and will then influence greatly the estimation of the aerodynamic forces. This then means that its orientation potentially has some effects on the values of the estimation of the aerodynamic forces. Then comes the drag efforts these are the second main source of effort behind the tension, whether it is for a straight flight or a turn. When summing for all types of flight the mean values of the KCU's drag and tether drag, those forces then becomes not negligible with respect to the tension force. Also something not surprising at all is that the inertial effects due to the KCU or the wing are much more present during turns than straight flights, to a point where they become as important as the drag effects during turns. The most negligible efforts in the end are the weights of tether, KCU and wing, however since their values are constant it is not impossible that they become more important than the inertial effects during straight flights. All in all, when considering the average values the sum of all the efforts apart from the tension will make up between a third to a half of the average tension.

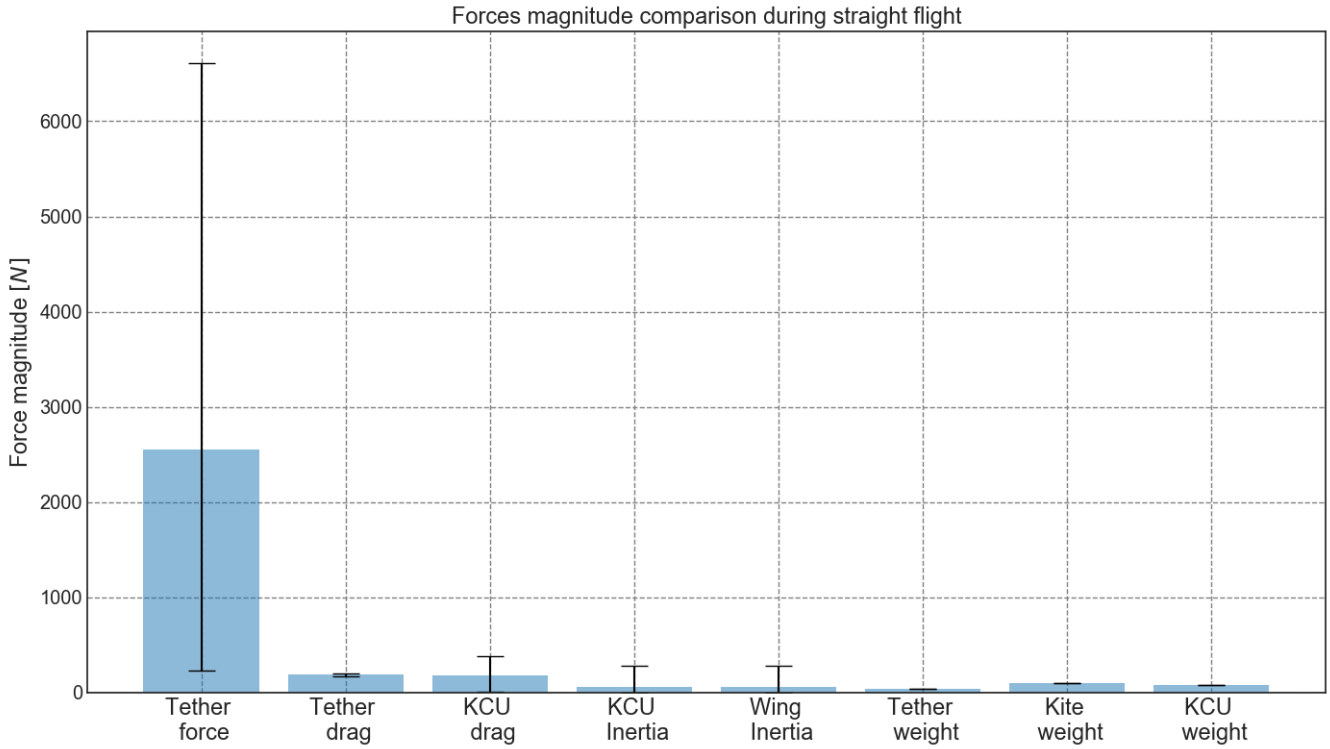

FIGURE 4.23: Dimensional analysis for straight flights: mean values in blue and maximum and minimum values given by segment

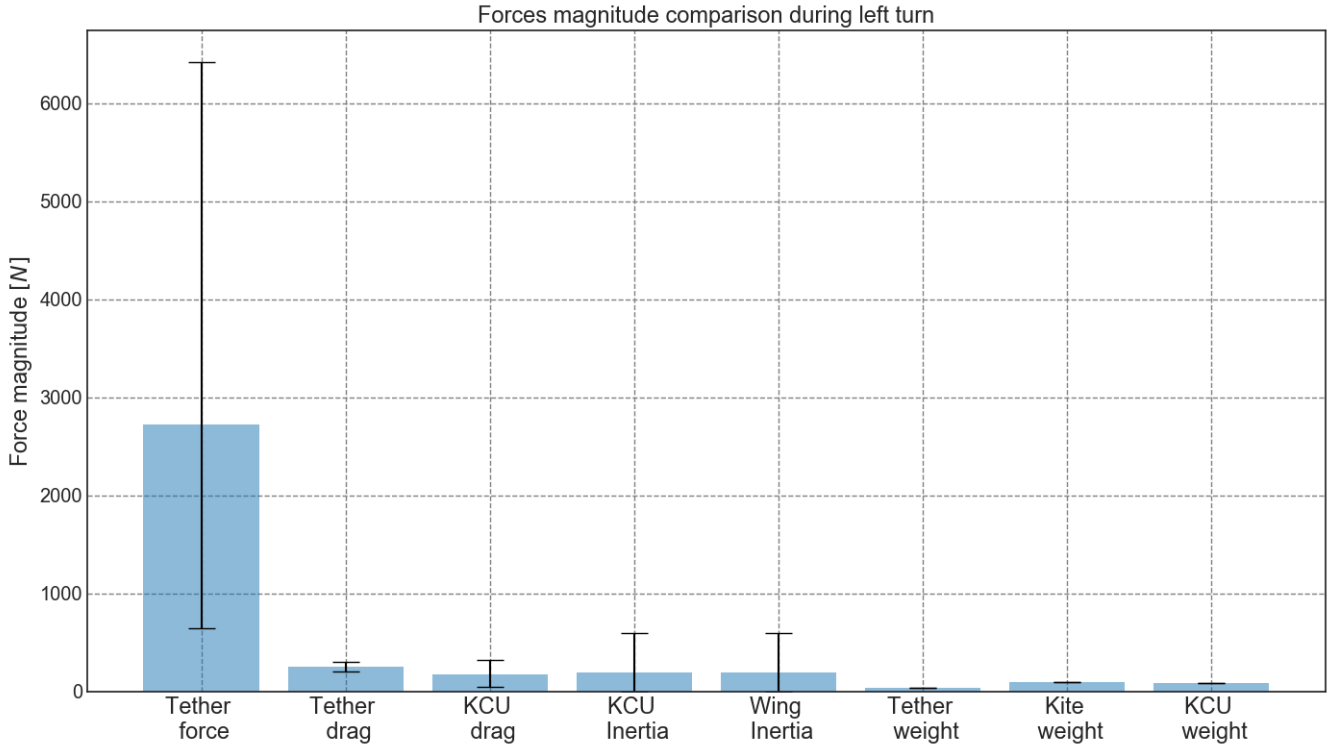

FIGURE 4.24: Dimensional analysis for left turns:mean values in blue and maximum and minimum values given by segment

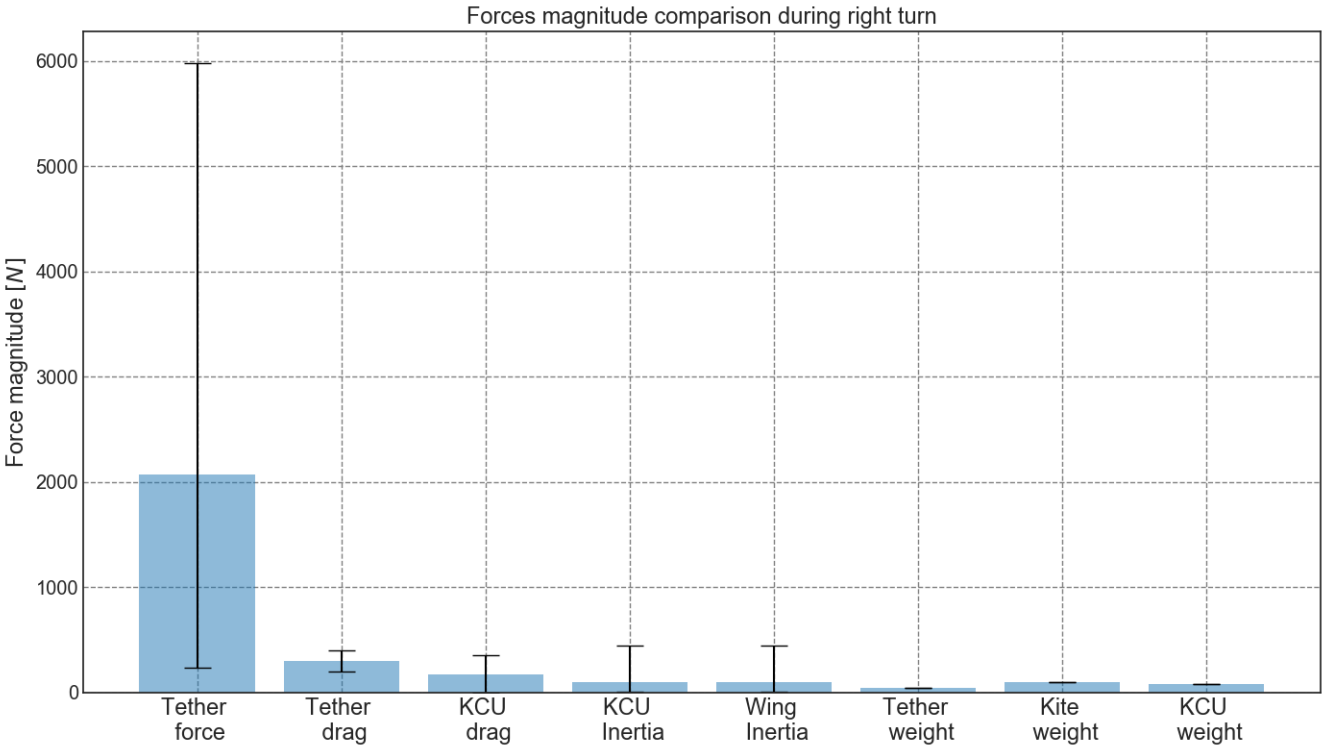

FIGURE 4.25: Dimensional analysis for right turns:mean values in blue and maximum and minimum values given by segment

4.3.5 Turning rate law

4.3.5.1 Model

Since the 3 plate model had some issue evaluating the side efforts needed to balance the inertial forces another approach was used to quantify the turning effects of a kite. This is done through a turning rate law that will only focus on trying to explain how a kite turns. Several assumptions were made before drawing any formulation for this law:

1. First the kite is assumed to fulfil its turn on a single plane. This property was verified and the kite would not exceed a change of plane of 2[m] which is assumed negligible for a turn radius of 25[m]. Therefore the problem is planar and the tangential plane is called τ
2. Only the aerodynamic side force $\mathbf{F}_{a,s}$, inertial force and weight force are taken into account.
3. $\mathbf{F}_{a,s}$ is assumed to vary linearly with the steering input δ_s
4. The kite's yaw rate $\dot{\chi}$ is equal to the instantaneous angular velocity of the kite around the instantaneous center of the turn.

The aerodynamic side force considered to balance out the gravitational and inertial effects corresponds to the projected side aerodynamic forces onto the y axis of the kite:

$$\mathbf{F}_{a,s} = (\mathbf{L}_l + \mathbf{D}_l + \mathbf{L}_r + \mathbf{D}_r).\mathbf{y_B} \tag{4.14}$$

Assuming that the kite's radial velocity is negligible with respect to the kite's tangential velocity $\mathbf{v}_{k,r} << \mathbf{v}_{k,\tau}$, one assumes $\mathbf{v}_{k,\tau} = \mathbf{v}_k$ the force balance on the kite's during a turn considering the inertial force gives:

$$F_{a,s} + m\mathbf{g}.\mathbf{y}_B = mR\dot{\chi}^2 \tag{4.15}$$

Supposing that for moderate steering actuation a linear dependency between the side force and the steering exists: $F_{a,s} = Cv_a^2\delta$ and considering $R\dot{\chi}^2 = \mathbf{v}_k$ the final turn rate law is found:

$$\dot{\chi} = K\frac{v_a^2\delta}{v_k} + \frac{\mathbf{g}.\mathbf{y}}{v_k} \tag{4.16}$$

The coefficient K would then correspond to a parameter proper to each kite and to identify with experimental data. In a previous attempt the hypothesis that $v_k \simeq v_a$ was made, meaning that the wind velocity if negligible with respect to the kite's velocity. This lead to an hysteresis effect where the kite would turn faster at the end of a turn than at the beginning. After verification it seems that the apparent wind velocity at the height of the flight is not negligible since $v_k \simeq 1/2v_a$. The hysteresis effect then makes sense since the kite accelerates during a turn since it is flying downwards and the law was previously not normalised by v_k.

4.3.5.2 Results

Using the yaw rate, orientation, apparent wind speed and kite's velocity measurements a linear regression was made to first of all find out if the turning rate law considered would fit the data and if so find the constant K defined in equation 4.16 and specific to each kite. As shown in figure: 4.26 the presented law fits surprisingly well the data to an accuracy of 88% based on the residuals. After computation the 95% confidence interval lies between $[+0.126, -0.122]$ of the linear regression. First of all the data clearly shows the asymmetry previously denoted, as the data cloud is not centred on zero, meaning that the kite stops turning not with a zero steering input but in our case with a positive steering input. Also shown here by the data is the non linear behaviour when transitioning from a stand still to a rotation. There is indeed a plateau when the corrected yaw rate $\dot{\psi}_R - \mathbf{g}.\mathbf{e}_y^B/v_A$ reaches zero, meaning that when initiating a turn, the transition between straight and curved flight does not happen instantly. This might come from the combination of inertial effects and the transition time needed for the aerodynamic loads to establish once the steering input is actuated. Also the fact that the apparent velocity is during a turn higher than during straight flight may indeed play a role on the aerodynamic efforts during this transition. It then seems that once the turn is initiated, the linear behaviour is restored. Finally notice the dependency of $\dot{\psi}_R$ with v_A this will then mean that if the steering input u_s is maintained constant, a sudden change of v_A due to for example a wind gust will directly affect the yaw rate.

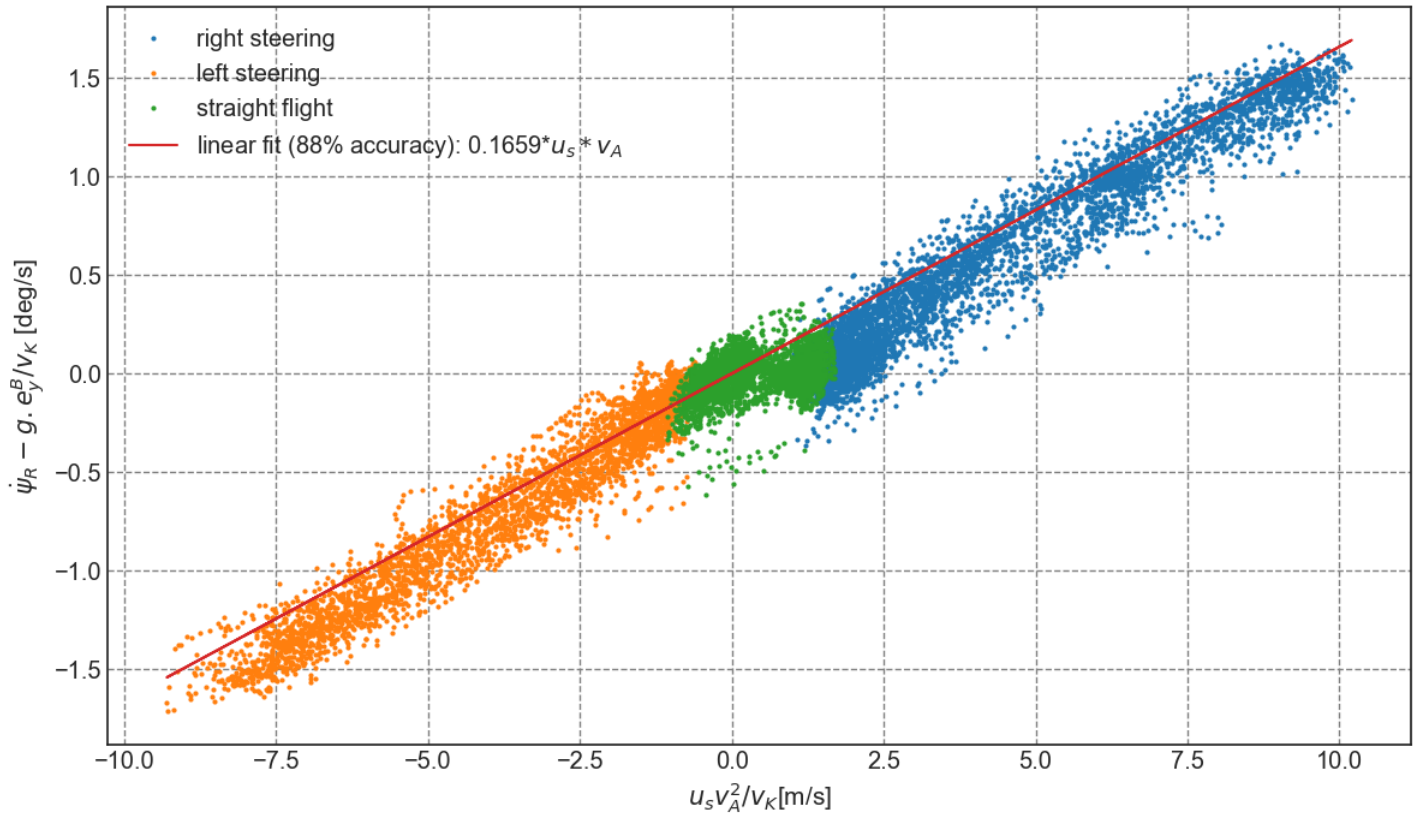

FIGURE 4.26: Turning rate law identification using experimental data

Chapter 5

Simulation and Identification results

In this chapter the data will sometimes be split into powered flights corresponding to the reel out phase and depowered flights corresponding to the reel in phase. The powered flights are then split into three different flight category straight flights, right and left turn. The empirical filtering applied on the steering and power input to select the data is summarized in table ??.

Type of flight	Depowered Flight	Powered Flight	Right Turn	Left Turn	Straight Flight
Mask	$u_p < 0.701$	$u_p > 0.778$	$u_s < -0.08$	$u_s > 0.05$	$-0.08 < u_s < 0.05$

TABLE 5.1: Mask used for filtering the data

5.1 Direct computation of the aerodynamic coefficients

As shown in chapter 3, a direct estimation of the aerodynamic parameters is possible. This is then done to find the total lift and drag of the kite for the 3 plate aerodynamic model. For a matter of comparison and verification some additional lift and drag coefficients were computed using Oehler's modified model. CFD results coming from Patrick Demkowicz [9] thesis are also used for comparison. The CFD results were computed for a Reynolds number of 3.10^6 where the Reynolds number of the experimental data computed with the average measured apparent wind id $3.6.10^6$.

5.1.1 Model comparison and early observations

3 plate model vs Oehler's model: When comparing the aerodynamic coefficient either obtained with Oehler's model or the three plate model in figure 5.2 and 5.1 it seems that both the lift and drag coefficient capture the same trends. One can therefore say that there is an increase of trust in the information about the difference in lift and drag coefficient with respect to an increase of the angle of attack since it was found with two different methods. This also shows that to capture such an information there is no need for implementing a complex model. Also one notices an offset in the y-axis between the lift and drag coefficient of the two models, which is negligible for the lift but not for the drag. This then probably comes from the different efforts considered in those two models but also from the difference in the orientation since Oehler's model does not account for the pitch nor the roll of the kite.
Confidence interval: As a remark the 95% confidence interval is very close to the mean, this partially comes from of the quality of the data but mainly from the fact that the angle of attack are discrete. This then means that most of the samples are aggregated to those discrete values, hence "artificially shrinking" the 95% confidence interval as shown by the relation to estimate it: $C_{95\%} = [\bar{x} - \sigma/\sqrt{N}, \bar{x} + \sigma/\sqrt{N}]$. Indeed for a given standard deviation if the number of samples increases the 95% confidence interval shrinks and gets closer to the mean value.

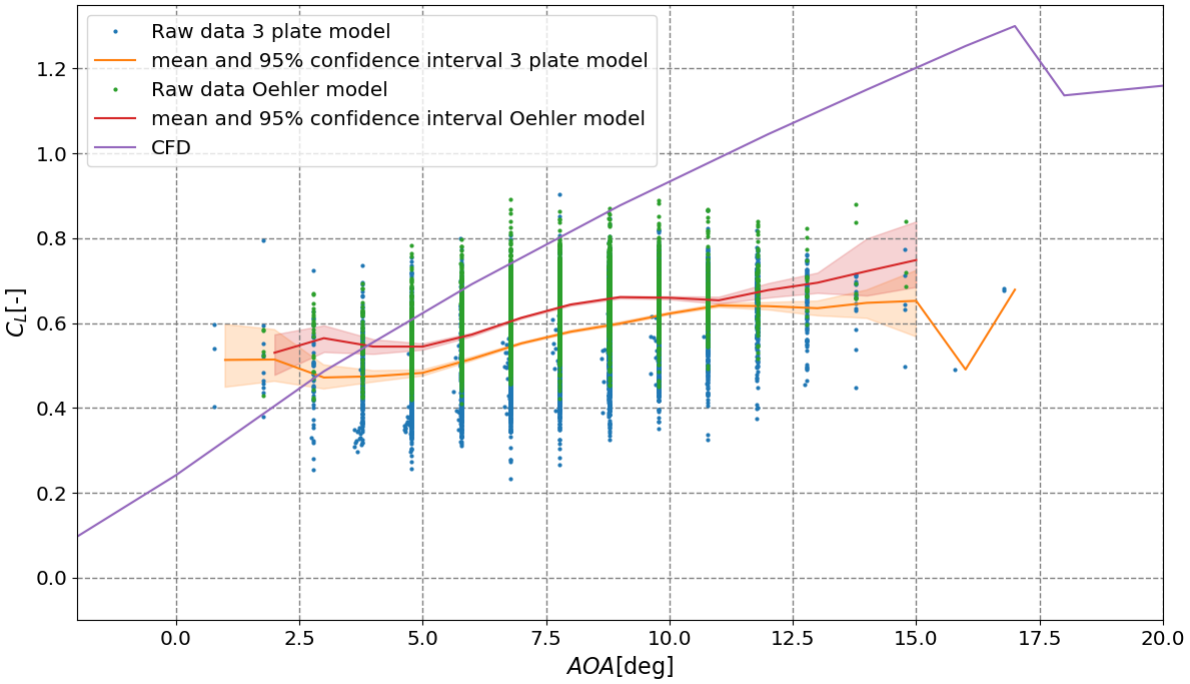

FIGURE 5.1: C_L function of the angle of attack of the wing α: comparison of 3 plate model, Oehler's model and CFD resutls

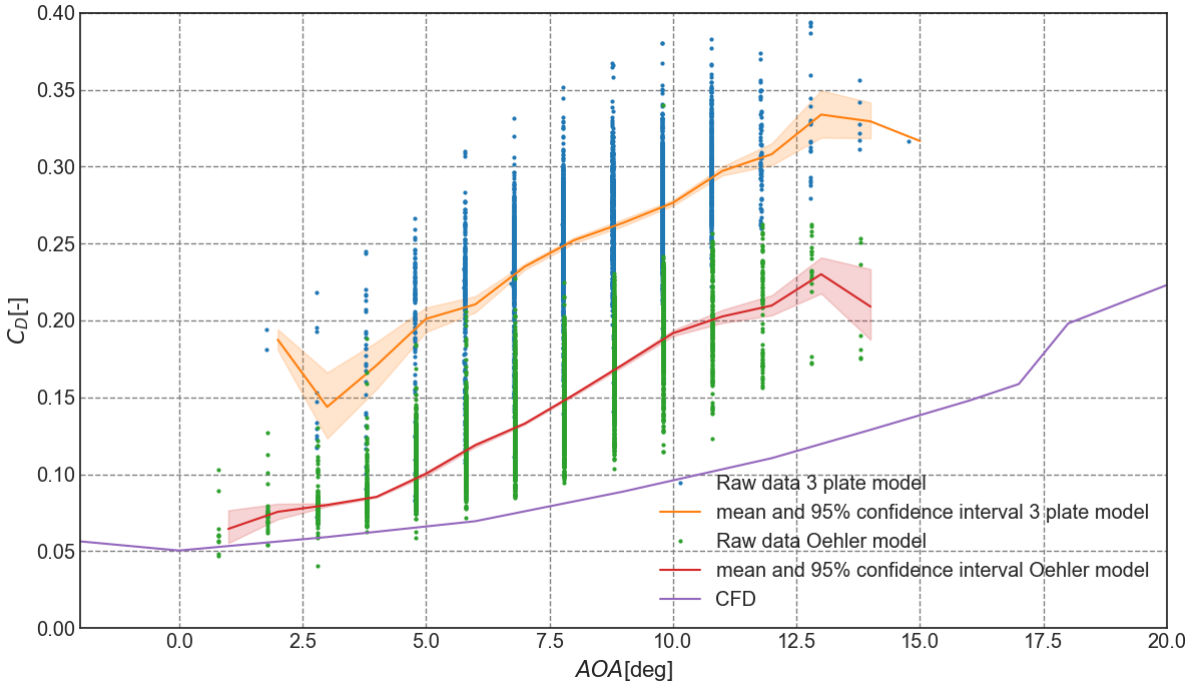

FIGURE 5.2: C_L function of the angle of attack of the wing α: comparison of 3 plate model, Oehler's model and CFD resutls

For complementary information both C_L and C_D the mean standard deviation was found to be equal to $\bar{\sigma} = 08$.
Experimental vs CFD: The difference between the experimental results and the CFD for the lift and the drag mainly comes from a difference in trend. This can be explained by the deformations that the wing is subject to during a powered flight. Since the geometry used for the CFD was rigid and chosen as the shape of the kite at rest, it will not match the shape of the kite during a real flight. Indeed in the experiment the wing deforms under loads when flying powered flights, mainly because of the flexibility between the parts of the wings that are transmitting the efforts. The canopy is reinforced and rigid however the connection between the canopy and the front beam is still not and flexes under stress. This then brings down the front beam of the wing and increases the frontal surface area of the kite and therefore the drag. This change of shape also affects the slope of the lift, which decreases under loads.

5.1.2 Influence of power input on the aerodynamic coefficients

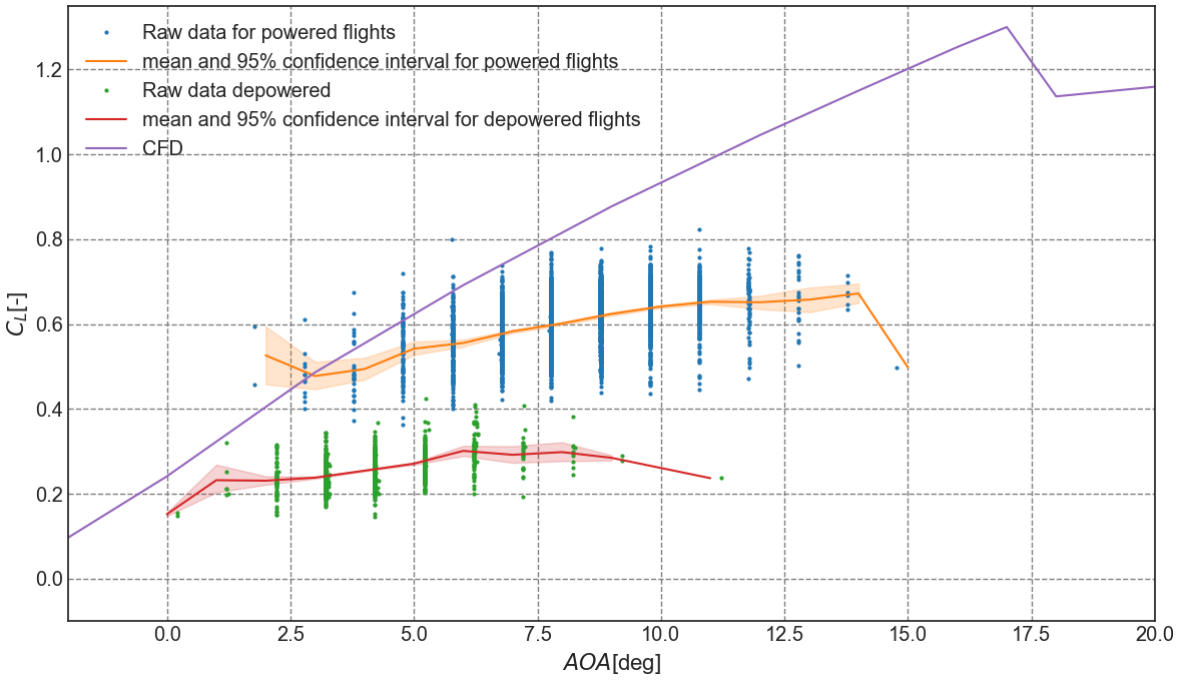

FIGURE 5.3: C_L comparison for the wing between powered and depowered flights for the 3 plate model

As a follow up to the previous conclusions on the difference between the CFD and the experimental results, it was thought that comparing the experimental results between a powered and depowered flight would bring some light on the previous conclusions. Looking at figure 5.4 and 5.3 seems to partially confirm the previous explanation of the deformation. Indeed figure 5.4 shows that during depower the drag coefficient C_D gets closer to the CFD results. This does not only affect the offset to the CFD curve but also the difference in slope. Since the kite under depower mode is subject to lower loads the deformation should be smaller and the frontal area of the kite should decrease and the drag with it pulling the experimental results closer to the CFD results. However this still does not explain the difference that remains in the C_L curve (figure 5.3). Indeed in figure 5.3 the lift curve in depower mode still has the same slope as in power mode, which is smaller than the one found in CD. Therefore the deformation talked about might only

affect the frontal surface area and will therefore only have an effect on the drag.
Regarding the effect of the power and depower mode on both of the C_L and C_D curve, it seems not surprising that the lift as well as the drag decrease when going from power to depower mode. This is mainly due to increasing angles of attack and the flattening of the wing because of increasing loads, which in the end will increase the total surface area producing lift. This affects the performance coefficient C_L/C_D in a way that it is in average for the same angles, two times bigger in power mode than in depower mode . So not only does the power input affect the angle of attack of the wing but it will also act on its performance. It is also clear in figure: 5.4 and 5.3 that the average angle of attack seen by the wing increases when going from power to depower mode, as the center of the data cloud shift towards higher angles.Also The same remark can be made about the confidence interval.

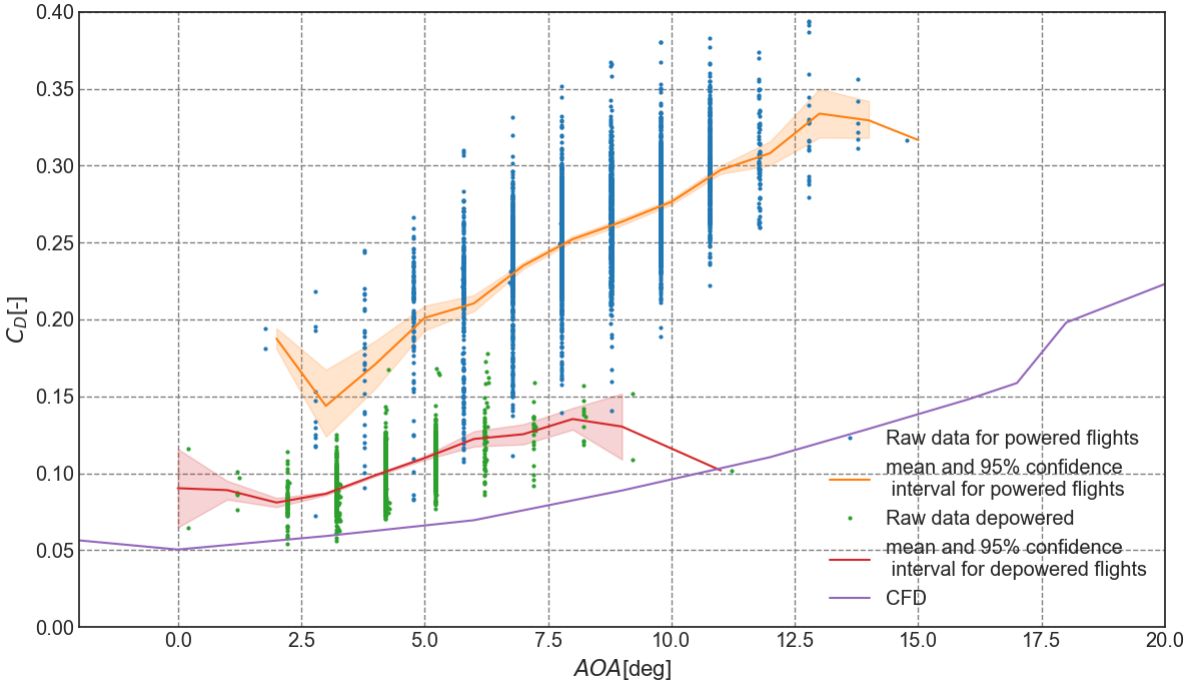

FIGURE 5.4: C_D comparison for the wing between powered and depowered flights for the 3 plate model

5.1.3 Influence of turns on the aerodynamic coefficients

To continue to assess the aerodynamic performance of the kite during its flight a study of the influence of a turn on a kite's aerodynamic parameters was made. The turns in question were the one the kite makes during a figure of eight meaning that for this study the kite was always in its power mode. The model used for this section was the 3 plate model. The performance of the kite drops during a turn as shown in figure 5.5, 5.6 and 5.7. The lift coefficient decreases during a turn whilst the drag coefficient increases during a turn. The lift decreases because during a turn it must balance the inertial effect and there might also be some wing deformations due to the turning mechanism that changes the geometry of the wing and therefore its lift producing capability. The drag increases during a turn, the hypothetical reason would be that the steering mechanism augments the lift of the side ears and would then increase the drag of these ears. Another hypothesis would also as well be that because of the turning mechanism that warps and deforms the kite, the geometry of the wing changes and with it would come an increase in the drag

force. This finally translates on average to a 5% performance loss during a turn as shown in 5.7. Note also that for angles smaller than 5 degrees the L/D is not statistically sound because there are not enough samples therefore the relationship should only be considered for angles greater than 5 degrees.

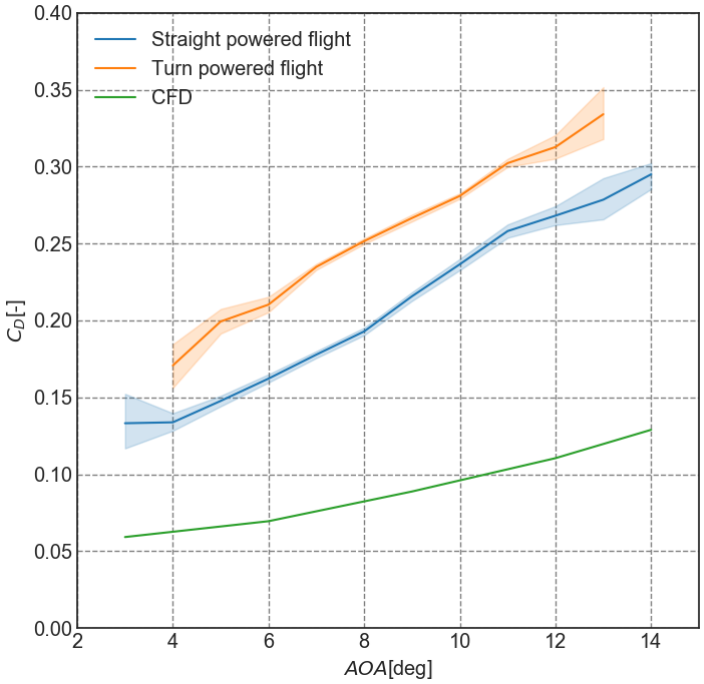

FIGURE 5.5: C_D comparison between a turn and a straight flight

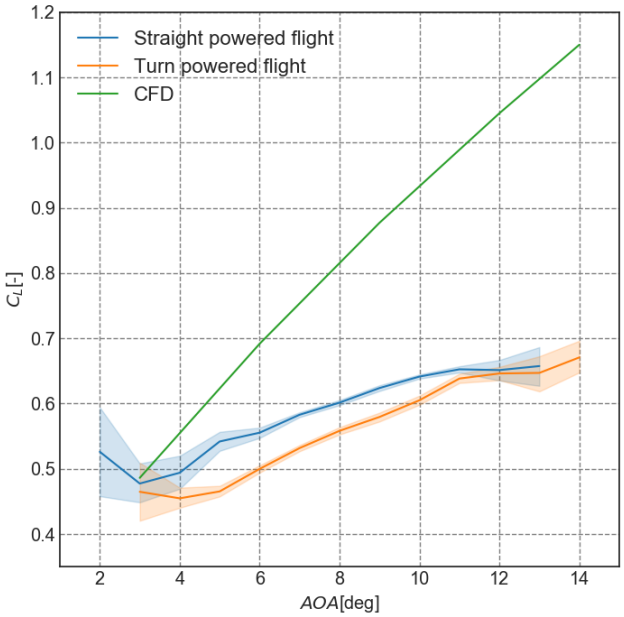

FIGURE 5.6: C_L comparison for the wing between a turn and a straight flight

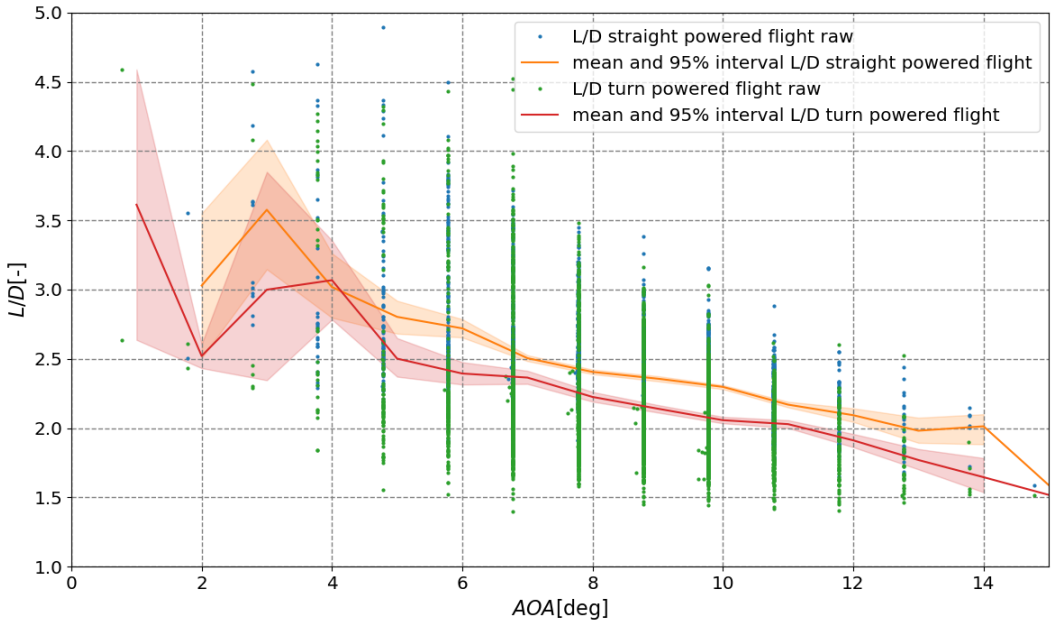

FIGURE 5.7: L/D comparison for the wing between a turn and a straight flight

5.2 Sensitivity study of the aerodynamic coefficients

As mentioned in the dimensional analysis of Chpater: 4 the tether tension accounts for at least a half to two thirds of the total effort applied on the kite. Therefore one supposes that the orientation of the tether tension vector could have a significant impact on the estimation of the aerodynamic parameters. So before building a complex model to compute the shape and orientation of the tether at each time step, a sensitivity study of the estimated aerodynamic parameters on angle values of the tether at the wing was performed. The approximation of the orientation of the tether was simply made by introducing a lag in the azimuth and elevation angles. The lag in the elevation angle would come from the weight and the drag of the tether during a turn. The effect of the weight would always create an increasing offset of the elevation angle value. As for the drag it was implemented so that the value of the offset would always stand in the direction of the apparent wind speed splitting its effect between the azimuth and elevation offset. The effect of an offset by the drag and by the weight would then be studied. Looking at figures: 5.8, 5.10, 5.9 and 5.11 it seems that the drag and weight offset mostly have an impact on the mean value of the lift coefficient, whilst it seems to have more of an effect on the standard deviation for the drag coefficient. Including the drag and weight offset should then decrease the lift coefficient value, and decrease the standard deviation of the drag coefficient values. So in the end the development of a complex tether model might only bring small improvements to the results. However it was deemed interesting enough to proceed to its implementation to study not only the effect it has on the estimation of the aerodynamic parameters but also to study phenomenon happening in terms of the tether.

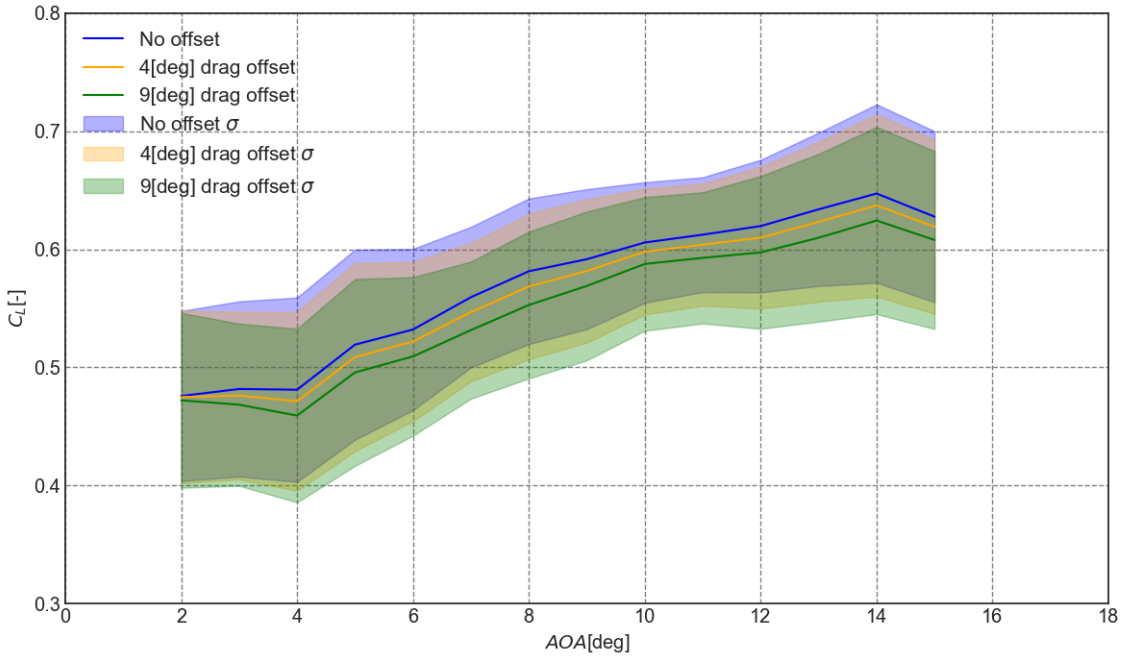

FIGURE 5.8: Influence on C_L of the offset due to the drag

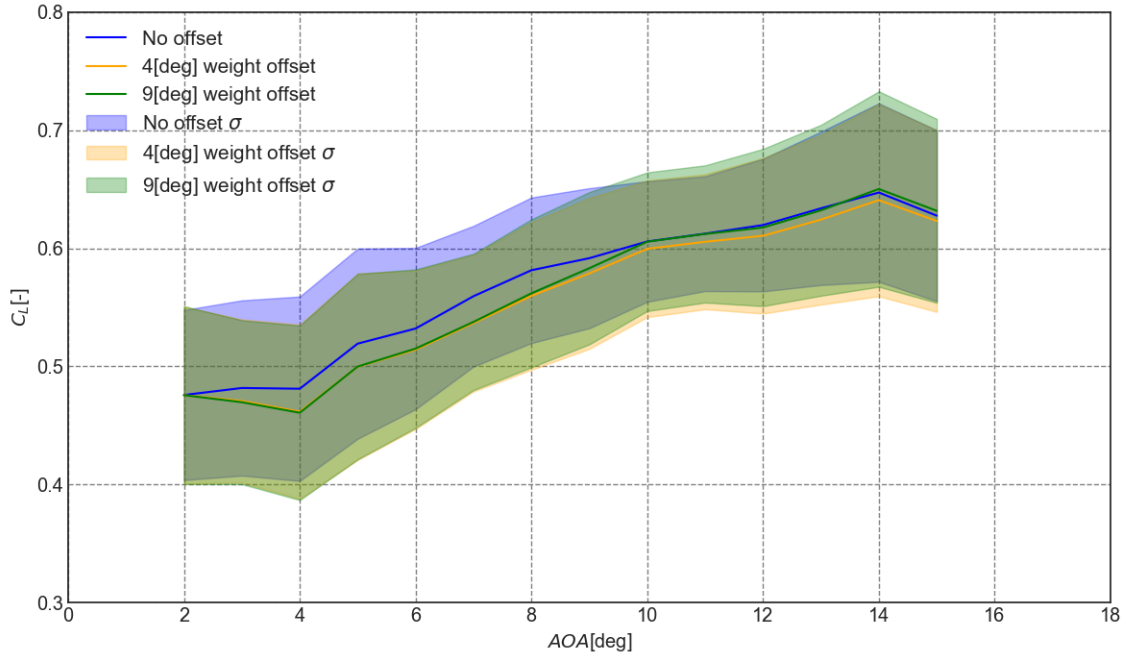

FIGURE 5.9: Influence on C_L of the offset due to the weight

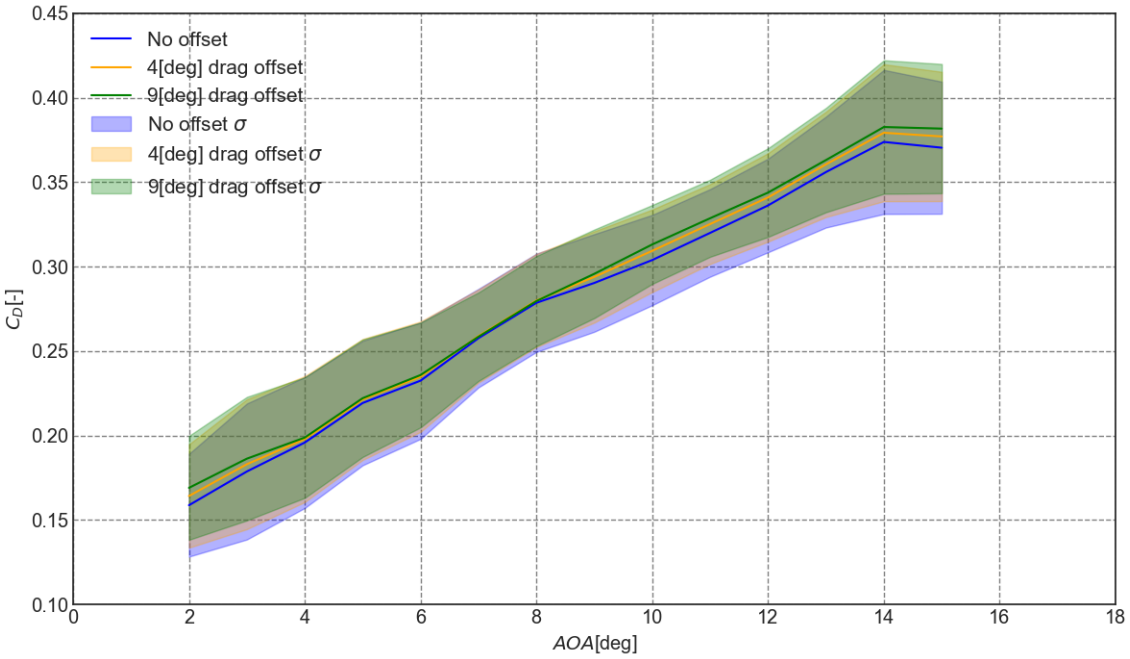

FIGURE 5.10: Influence on C_D of the offset due to the drag

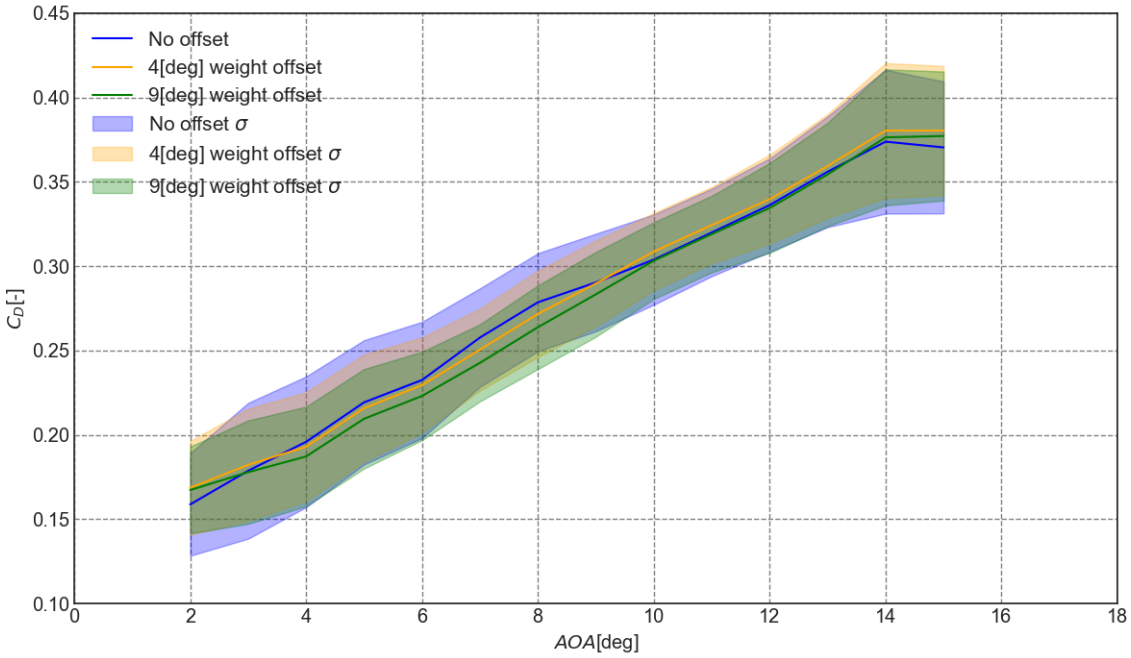

FIGURE 5.11: Influence on C_D of the offset due to the weight

5.3 Results of the discrete multi mass tether model study

5.3.1 Orientation at the kite

The main reason of the implementation of the multiple discrete mass tether model was to get an estimation of the orientation of the tether at its anchor point with the kite. The identification

5.3.1.1 When flying figures of eight

For the estimation of the difference between a model considering a straight tether and the discrete multi mass tether model in terms of the orientation at its anchor point with the kite, a simulation of a complete figure of eight was performed (see figure: 5.12).

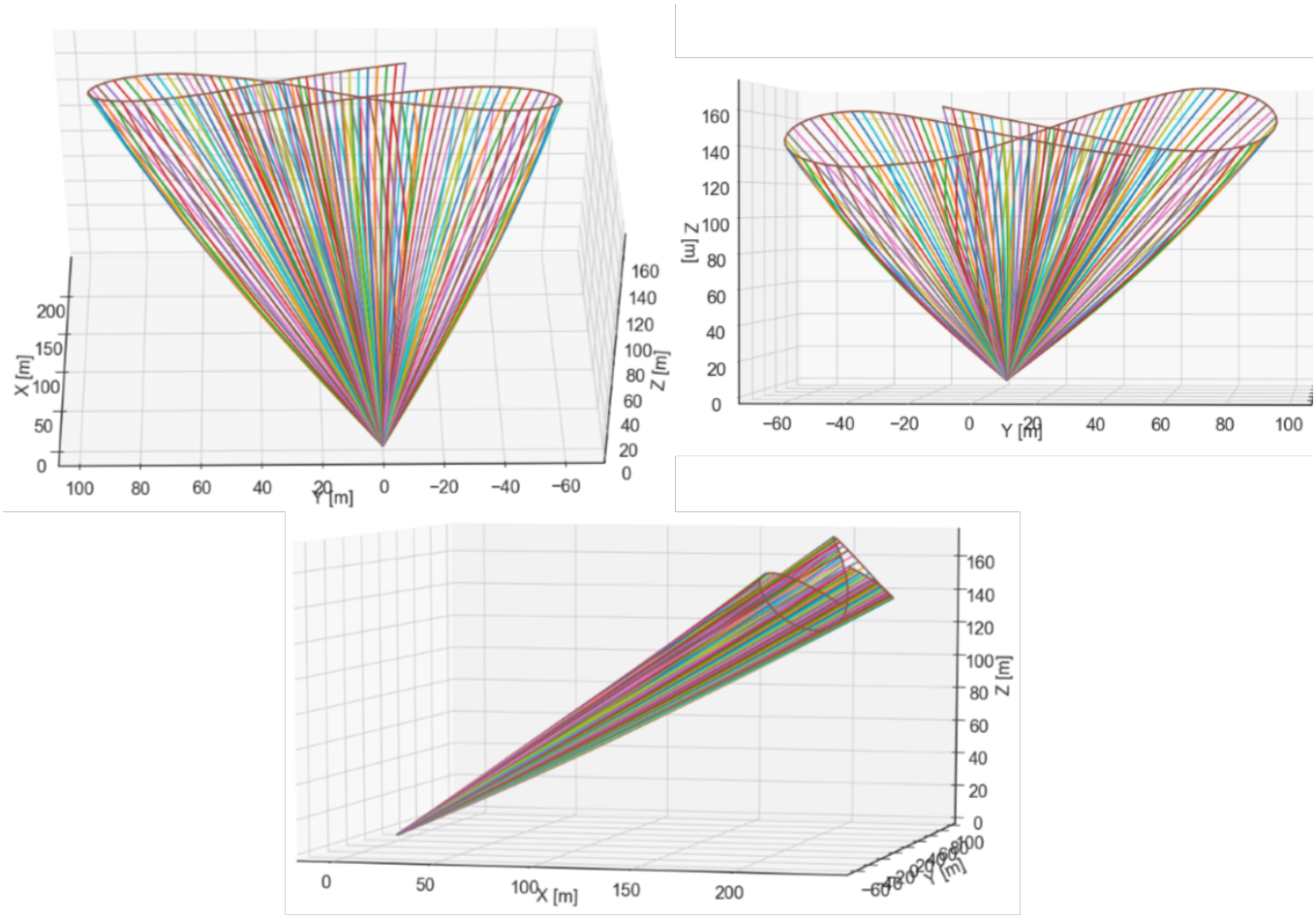

FIGURE 5.12: Trajectory of the end point of the tether and tether geometry during a figure of eight flight (top left: up view, top right: facing view, bottom: side vies)

To investigate the values of the orientation of the tether at the anchor point, the angles found with the discrete multi mass model will be compared to the ones found if the tether was assumed straight. Therefore the difference between the angles of those two cases will be studied. The difference in polar angle θ (figure: 5.13) seems to manifest different behaviours between straight and curved flights. When flying straight the difference increases negatively. Since the kite is flying upwards when flying straight, the sag effect due to the weight will increase, since the tension decreases, hence the negative increase in the difference. It also seems, that the sag in θ is mainly

due to the weight during a straight flight. Indeed, when computing the sag effect in θ with Benoit Python's model for a wind speed of zero (in orange in figure 5.13) meaning that only the weight effect is considered, the results do match. This also means that during a straight flight, the deviation in θ can be approximated using a simpler model of the catenary under its on weight. Now when looking at turns the difference increases positively compared to a straight flight. Since the kite is flying towards the ground during a turn, the drag effort exerted on the tether is opposing the weight effort, hence increasing the angle positively with respect to a straight flight. At the end of a turn as the kite starts flying upwards again, the tether "overshoots" downwards due to to the inertia, as shown in 5.13 (circled in red).

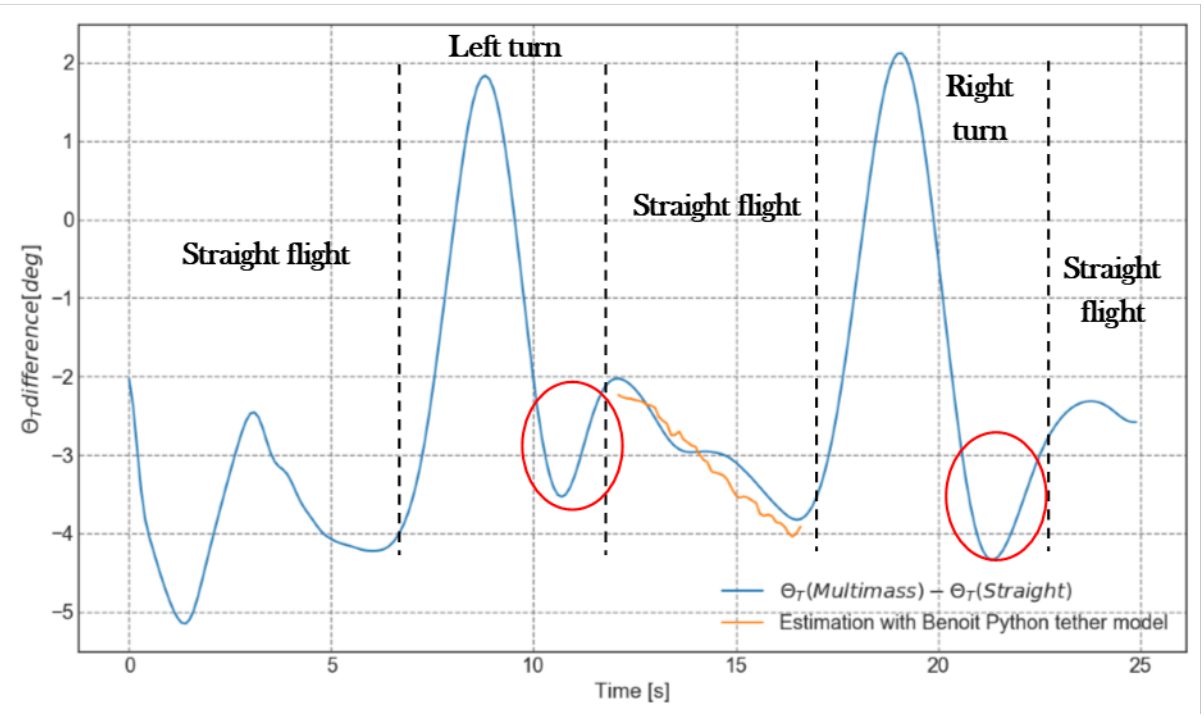

FIGURE 5.13: Difference in polar angle θ at the anchor point with the kite between a straight tether model and a discrete multi mass tether model

The difference in the polar angle ϕ between a straight tether and a flexible tether, has a relatively constant value for a straight flight (figure: 5.14). Also this value changes sign depending on whether the kite flies from left to right or from right to left. This is not surprising since the expected main contribution to this difference during a straight flight is the drag efforts applying on the tether. Since the velocity of the kite during a straight flight remains constant, the drag efforts on the tether should also be constant. However it seems that trying to capture this effect using Benoit Python's tether model gives an overestimation of the difference in the ϕ angle as shown in orange in figure: 5.14. This is most probably due to the different models used for the estimation of the drag coefficient, which will directly affect the value of the aerodynamic force. Right at the start of a turn the difference in ϕ angle increases before a left turn and decreases before a right turn. This increase is due to the change of direction of the kite and the inertia of the tether. Once the tether starts to follow the kite in its turn, the tether will swing outwards of the trajectory. The outward swing will reach its maximum when the kite reaches the point of maximum curvature of the trajectory which is in the middle of the turn, as shown in figure: 5.14 by the two peaks at $10[s]$ and $20[s]$. There is no doubt that this effect is due to the inertia of the tether, which will drag the

tether outwards of the kite's trajectory. This effect is also noticeable in the right hand top figure of figure: 5.12, where the tether seen from upwards shows a deflection at the extremity of a turn.

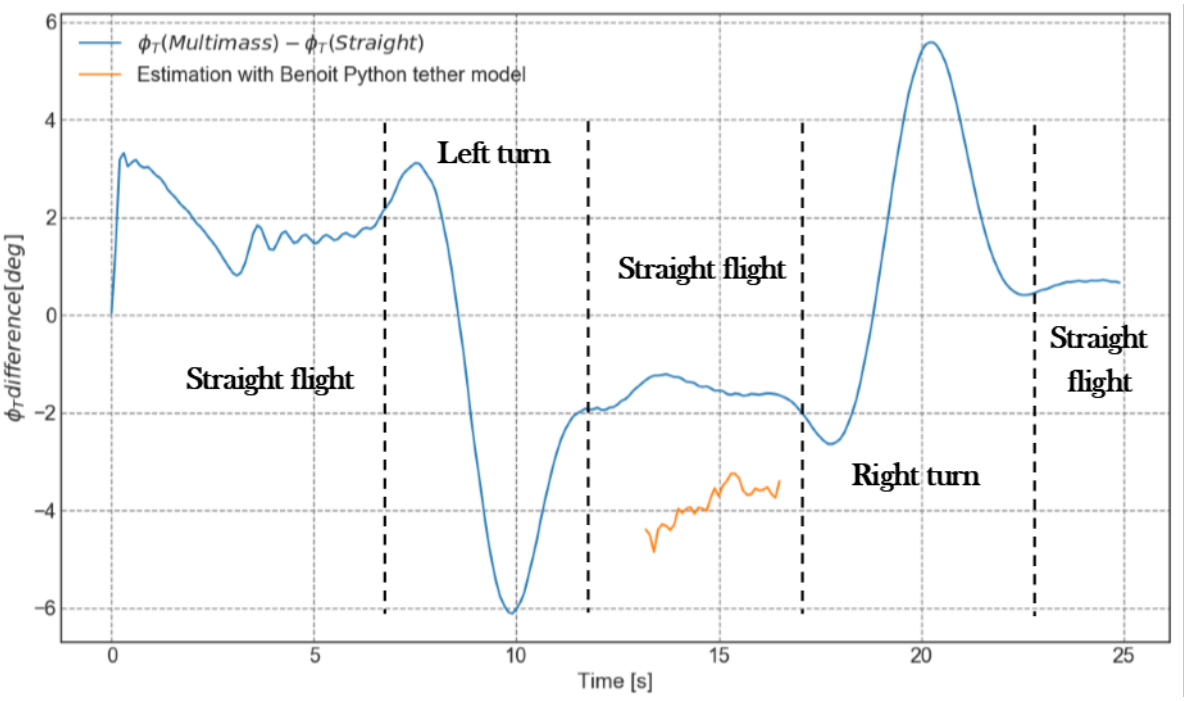

FIGURE 5.14: Difference in polar angle ϕ at the anchor point with the kite between a straight tether model and a discrete multi mass tether model

5.3.1.2 Reel in reel out comparison

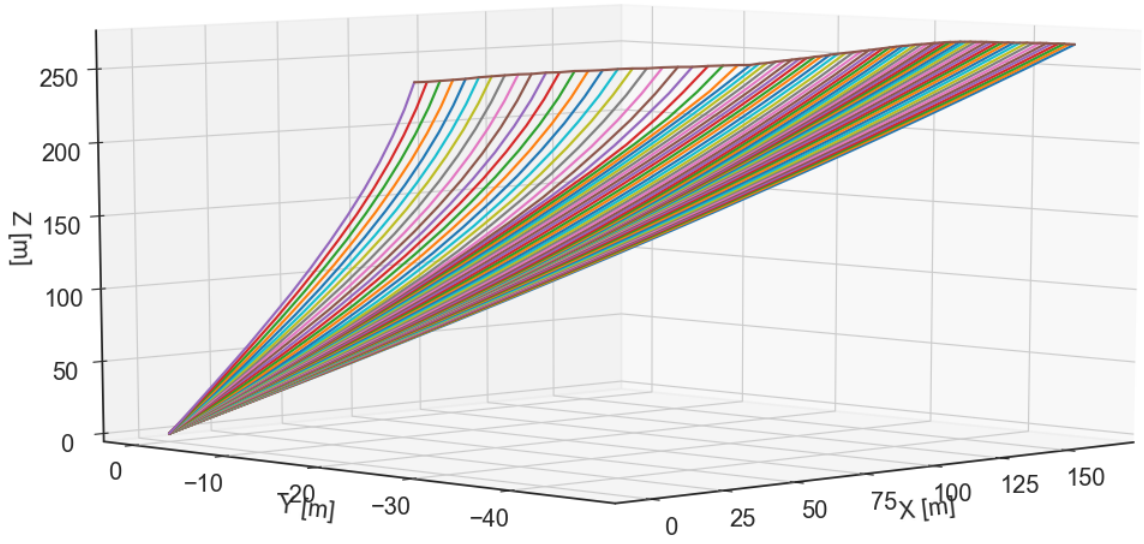

FIGURE 5.15: Illustration of the increase of sag during reel in

As mentioned previously, the efforts seen in the kite system during reel out are less than the ones seen during reel in. This has a direct effect on the the orientation of the tether at the kite as shown in figure: 5.16, where the sag doubles when going from reel in to reel out. The polar angle θ is only analysed since during reel in the kite is flying straight into the wind, therefore no significant efforts are expected across the tether. Since the weight and drag efforts are oriented in the same direction, while the tension in the tether is decreased, the tether inevitably will have a greater sag in θ polar than during reel out. Figure: 5.16 is a telling illustration of this behaviour, where the sag increases as the kite is flying towards the ground station.

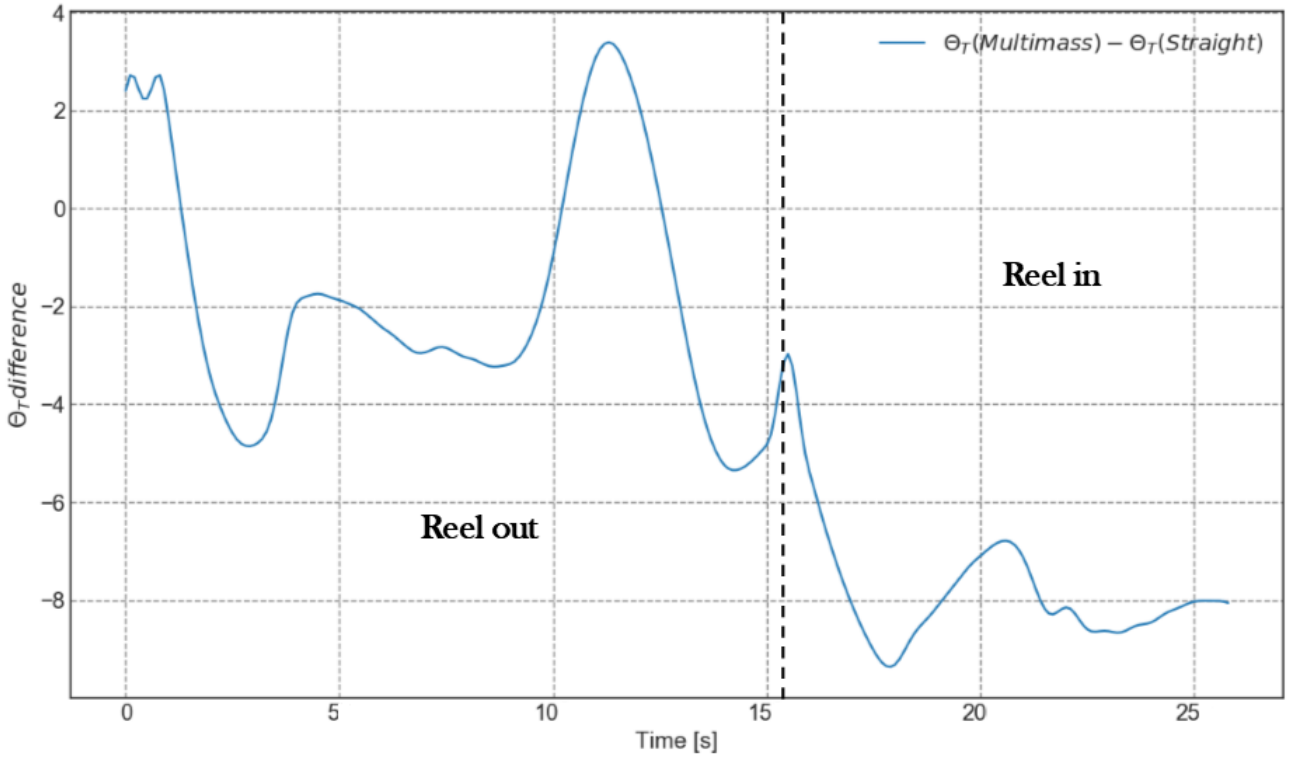

FIGURE 5.16: Influence of the power setting on the tether sag

5.3.2 Efforts

One of the advantage of the developed tether model is that it gives an estimation of the pulling force at the kite. Some of of this pulling force when transmitted by the tether, will balance the drag, weight and inertial efforts of the tether, hence decreasing the final force used to produce power. This model then gives access to an estimation of the losses in the tether. The amount by which this pulling force is decreased is illustrated in figure 5.17 where the percentage of losses in tether tension is showed. It is computed as follow:

$$Tether_{losses}[\%] = \frac{|\hat{T}_{kite} - T_{ground}|}{\hat{T}_{kite}} \tag{5.1}$$

Where $\hat{T}_{kite}$ and T_{ground} are respectively the estimated tension at the kite and the measured tether force at the ground station. It should also be mentioned that these results only concern the reel

out phase. From this figure it seems that there are more losses in the tether during a straight flight than during a turn. This comes from the fact that the tether tension increases during a turn. Therefore the proportion of the losses compared to the pulling forces become smaller because of an increasing tether force during at turn. Finally as shown in the figure the loss due to the external forces applying on the tether cause a decrease in average of 5% but can go up to 8% right before a turn.

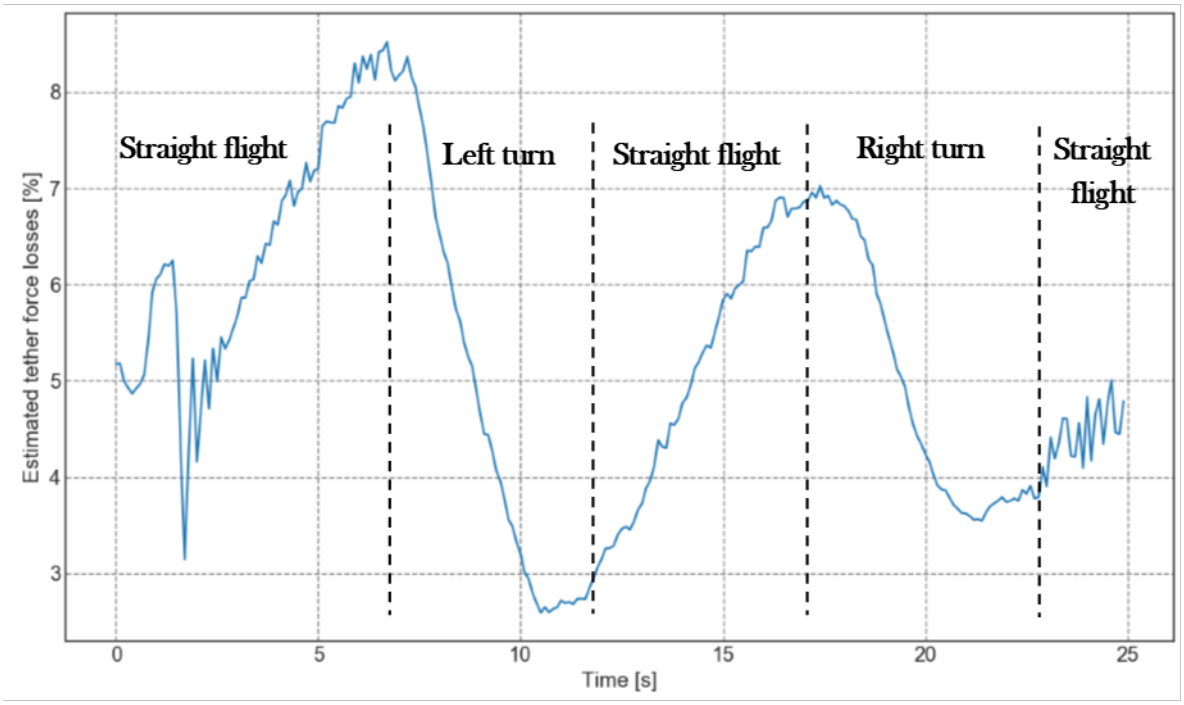

FIGURE 5.17: Loss percentage in tether force

From a perspective of comparison of models and investigation of efforts on the kite, the drag acting on the tether was computed for a straight tether model and the discrete mass tether model to compare them (see figure: 5.18). First of all the drag acting on the tether is greater during a turn than during a straight flight since the velocity during a turn increases. However as seen previously this increase is smaller than the increase in tether force during a turn, therefore the efficiency is in fact not worsened during a turn but improved. It also seems from figure 5.18 that the multi mass model gives a higher estimation of the drag than the straight rod model in certain conditions. The discrepancy might be coming from the difference in the apparent wind velocity seen by the tether since an extra care was given to choose the same aerodynamic model for both straight and multi mass models. Indeed the speed for a straight tether rod is assumed to vary linearly which might not be the case as in the discrete tether mass model in which a more accurate apparent velocity is computed based on a force balance for each element. Not only are the values different but they are also shifted in time, since the multi mass model shows some lag with respect to the straight rod model. Indeed the maximum drag for the straight tether is delivered sooner than for the multi mass model . This seems logical since the 'information' about an increase or a change in velocity is transmitted immediately to the entire tether for a straight rod but is not the case for a flexible tether model for which this transmission takes some time. This time lag is in the order of 2 to 3 seconds.

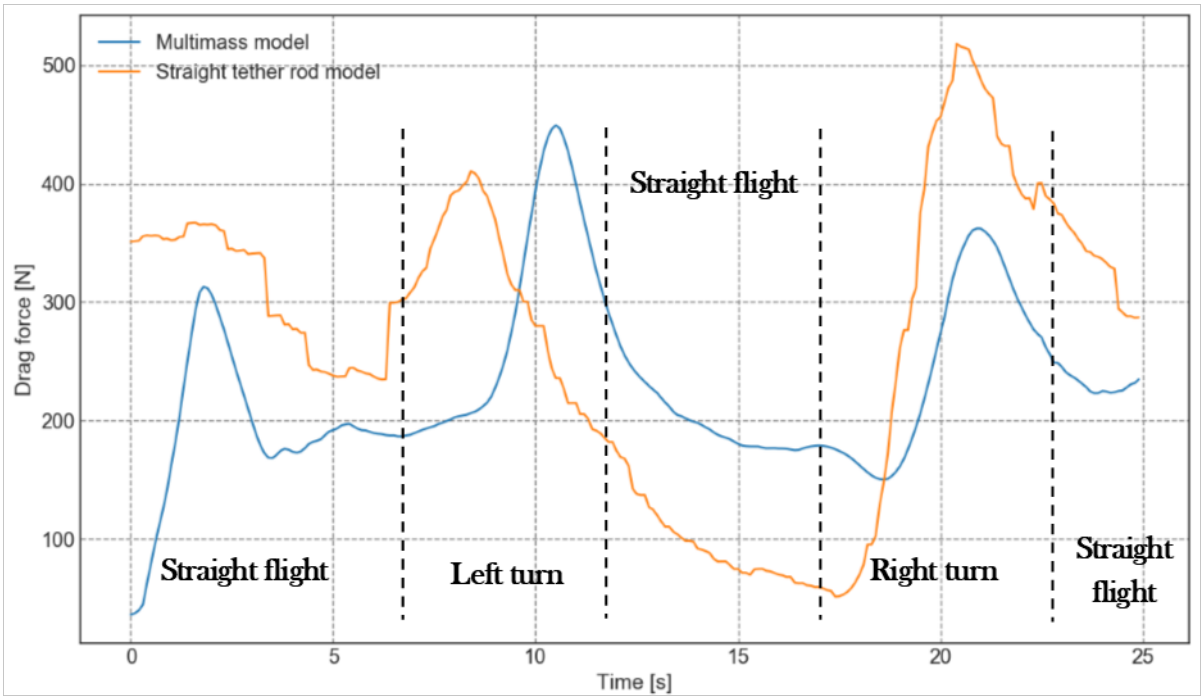

FIGURE 5.18: Drag acting on a straight tether and discrete multi mass tether model

5.3.3 Effect on the aerodynamic parameters

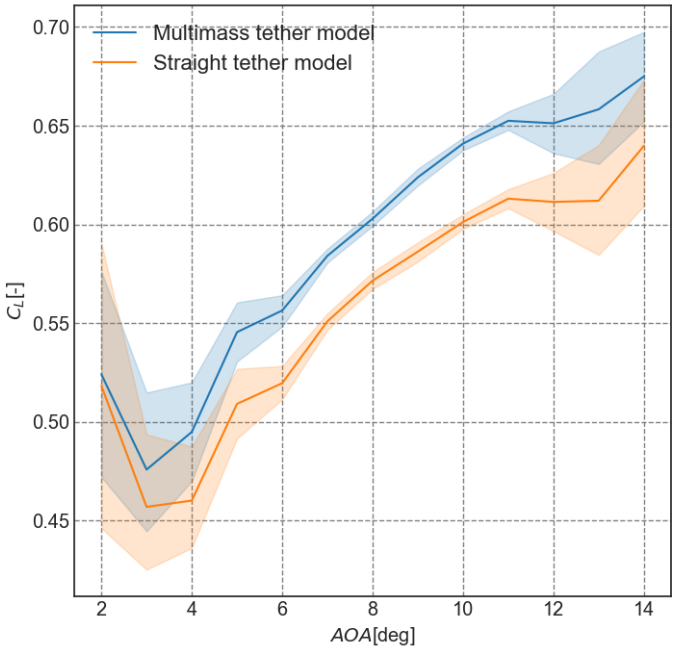

FIGURE 5.19: Influence of the tether model on the lift coefficient

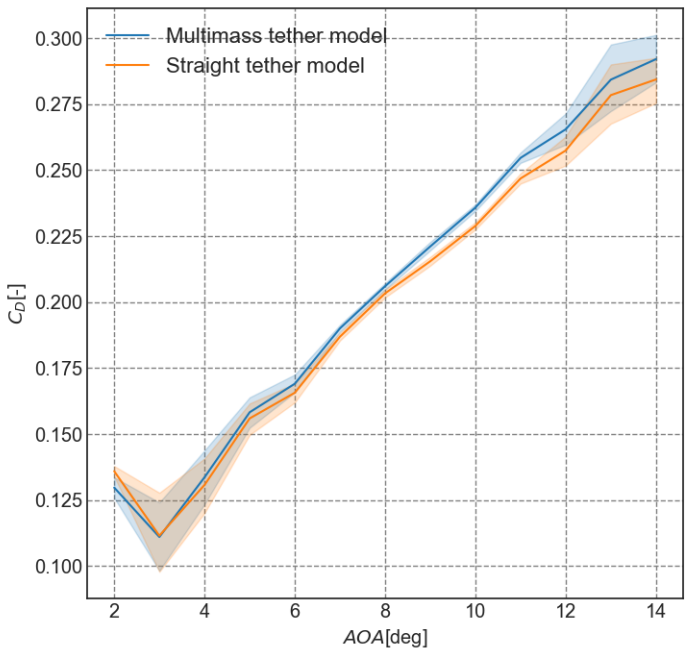

FIGURE 5.20: Influence of the tether model on the drag coefficient

The early idea of implementing a flexible tether model came to see whether or not it had an influence on the estimation of the parameters. The difference in the end does exist but is not major as shown by figure 5.20 and 5.19. Not only does the tether model reduce ever so slightly the 95% confidence interval it also increases the values of both C_L and C_D. Why this happens is a complex question, but in the end the flexible tether mass model seems to include and orient efforts in such a way that the lift has to balance more effort hence giving a grater C_L value. Also it should be mentioned that since the acceleration measurement was used as an input and the model is in the end an integration of the dynamic law, the error accumulated and the end point of the tether might drift away from the trajectory. Therefore the solution found to remedy to this is to reinitialise the problem when the difference becomes too big. A correction to the acceleration as an input was attempted but on successful because it created instability in the integration. For further development this would still be the right track, but the implementation of a controller would be needed.

5.3.4 Study of the effect of the tether diameter

One of the limit in the maximum of traction force is the load the tether can withstand. With wings increasing in size to produce more force and more power the tether must be adapted to those higher loads. One of the option would then be to increase the tether diameter. However this has consequences on the efforts and angles seen at the tether and this is what will be investigated in this section. It should be mentioned that for this study, only the tether diameter was changed and the tension force was kept unchanged since the measurements were taken as an input. As shown in figure: 5.21, 5.23 and 5.22 the values vary linearly with an increase in tether diameter when the drag force or the difference in angles are not changing to abruptly. However during an abrupt change highlighted by the peaks in the values, the value of the extrema does not vary linearly. Since this corresponds to a turn the share of dynamic effect is much greater meaning that a non

linear interaction between the change in inertia and drag can happen. This non linear interaction the gives peaks that are smaller than if the relation between the maximum and the tether diameter was linear. Also another noticeable effect is the shift in time of the values as the tether diameter grows. This is not surprising since the inertial efforts will increase with the mass and the tether diameter so will the drag, the transmission of a change of direction or velocity in the tether will then take more effort and more time. Hence the peaks in the data happen later for a tether with a larger diameter.

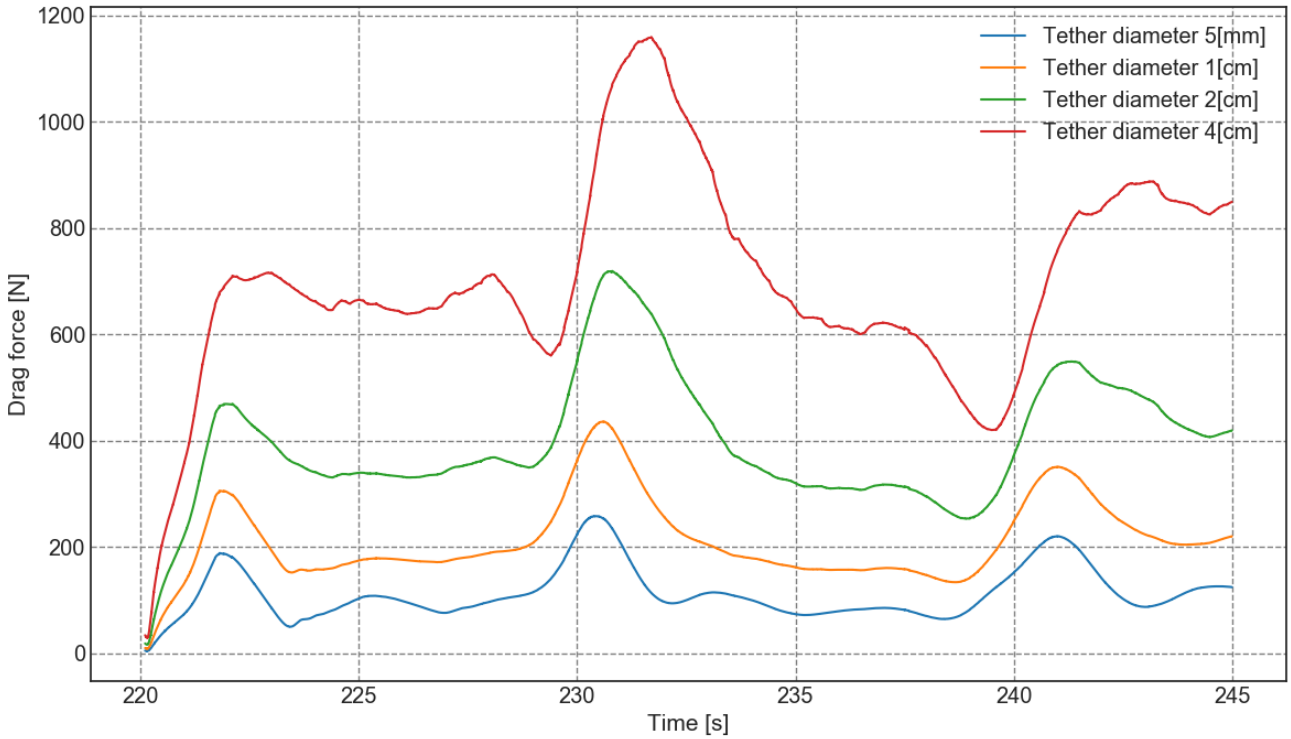

FIGURE 5.21: Effect of the tether diameter on the drag

5.4 Parameter System Identification

This section is only for your information, since the models were not verified and presented limits due to unavailable measurements. The parameter system identification was done by assuming that there exists a polynomial function between the lift coefficient and the power setting, steering setting and local angles of attack. The relation presented in Chapter 3 is simplified, by omitting the effect of the power input, since the experimental data only contains two discrete power setting one for reel in and the other one for reel out. To study its effect a test flight should be done with more than two difference power positions. Therefore only the steering input and the local angles of attack are considered. For the lift coefficient on the side, some limits were found. Indeed when directly computing from the experimental data the side lift coefficient, its value explodes

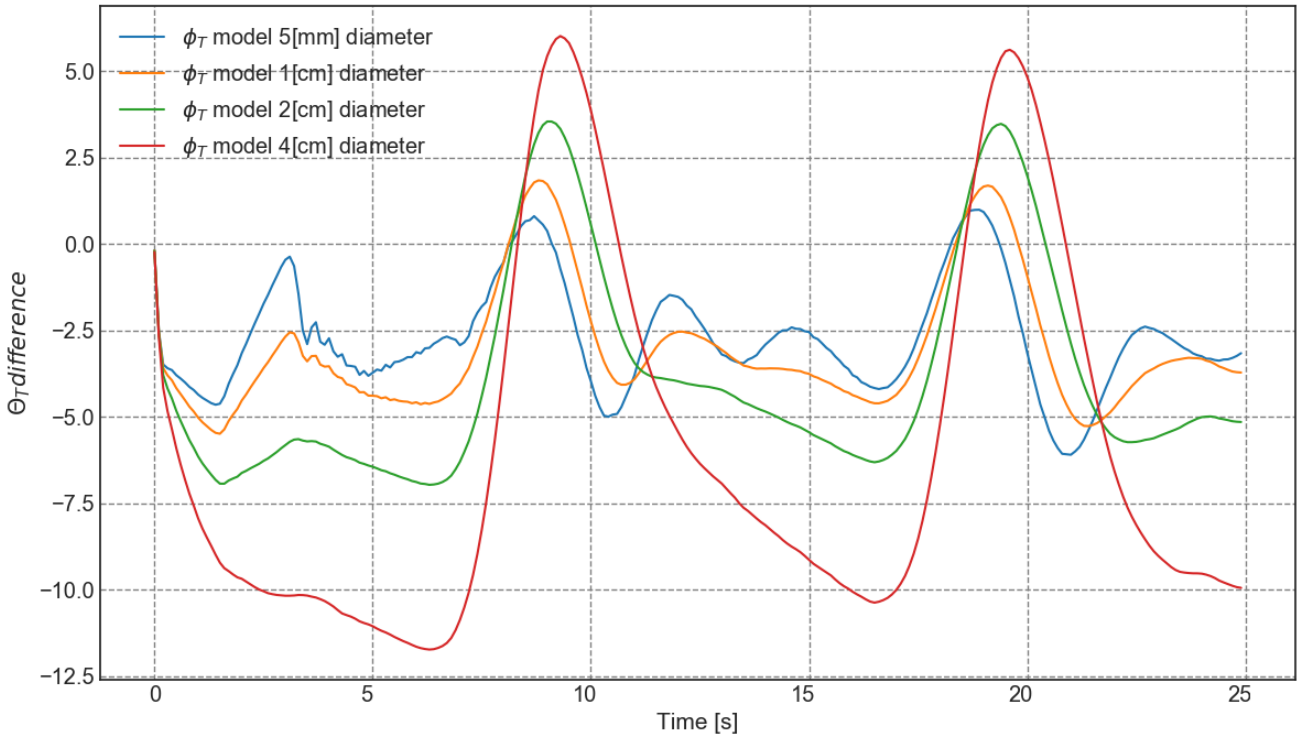

FIGURE 5.22: Effect of the tether diameter on the difference in polar angle θ

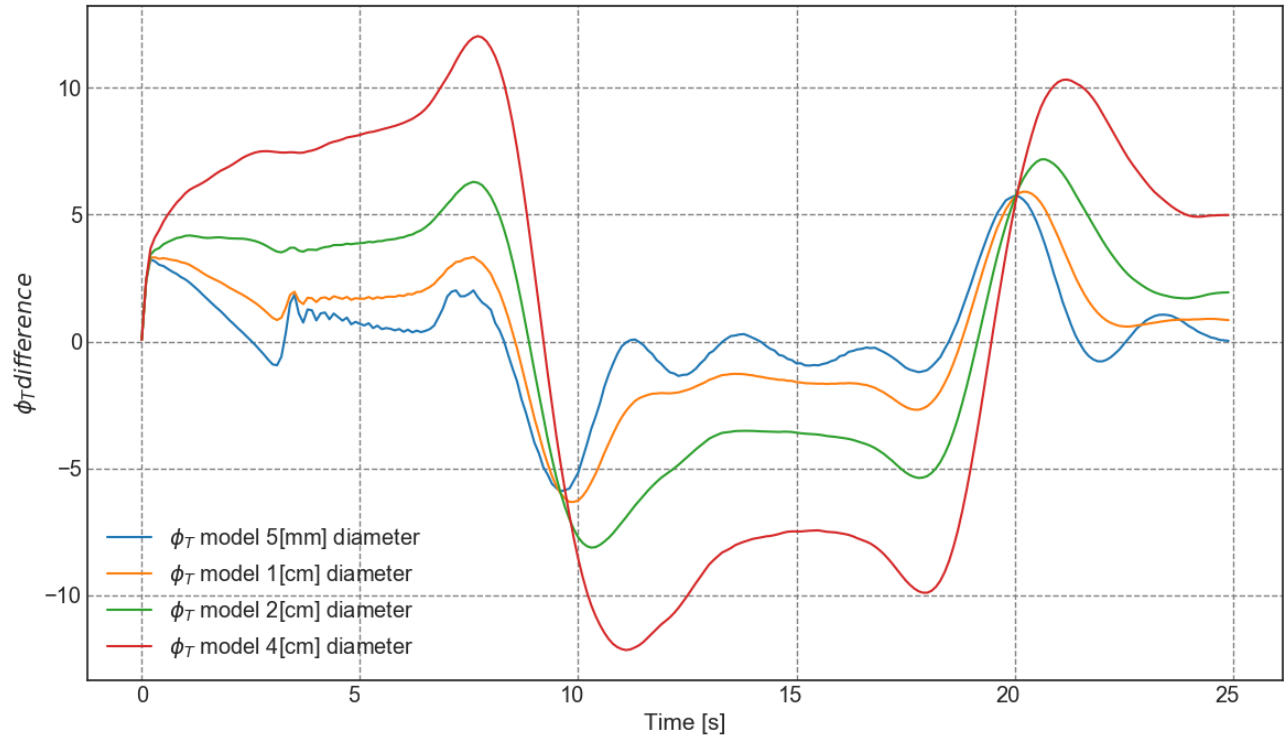

FIGURE 5.23: Effect of the tether diameter on the difference in polar angle ϕ

and reaches non-physical values. This is mainly due to a limit in the model, because the side slip angle is not measured the only parameter to change the angle of attack at the side is s change in the angular velocity. However during a straight flight this change in angular velocity does not happen and the velocity component available for the lift becomes so small because the angle of

attack is so smell that the only was for the model to have a side force big enough to compensate the side forces acting on the kite is to have a very large lift coefficient. Therefore to fix this issue, the side slip would have to be measured. The model is anyway available for further studies if in future experiments the side slip angle is measured. Also it was checked if this would not have any influence on the drag or the lift by transforming the coefficient and it seems that it does not if the proper lever arm are chosen. Indeed at the beginning the arm lever were taken as the position of the center of mass but they should in fact be taken as the position of the aerodynamic center. Once this is done there are no major changes noticed. Therefore the following model was identified for flights during reel in and reel out:

$$\begin{cases} C_L^K = C_{L,t}^0 + C_{L,t}^1 \alpha_K + C_{L,t}^2 \alpha_K^2 \\ C_D^K = C_{D,t}^0 + C_{D,t}^1 \alpha_K + C_{D,t}^2 \alpha_K^2 \\ C_L^L = C_{L,s}^0 + C_{L,s}^1 u_s + C_{L,s}^2 u_s^2 \\ C_D^L = C_{D,s}^0 + C_{D,s}^1 u_s + C_{D,s}^2 u_s^2 \\ C_L^R = C_{L,s}^0 - C_{L,s}^1 u_s + C_{L,s}^2 u_s^2 \\ C_D^R = C_{D,s}^0 - C_{D,s}^1 u_s + C_{D,s}^2 u_s^2 \end{cases} \tag{5.2}$$

The idea behind this model was to study the influence of the angle of attack on the top part of the wing, and the influence of the wing on the sides of the wing. Since the kite is not turning during reel in and for reasons explained previously, no identification of the side coefficients were made. The coefficient found are:

	$C_{L,t}^0$	$C_{L,t}^1$	$C_{L,t}^2$	$C_{D,t}^0$	$C_{D,t}^1$	$C_{D,t}^2$	$C_{L,s}^0$	$C_{L,s}^1$	$C_{L,s}^2$	$C_{D,s}^0$	$C_{D,s}^1$	$C_{D,s}^2$
Reel out	0.4653	0.4556	2.9085	0.0722	-0.3465	5.4567	0.326	1.715	10.1242	0.332	0.583	0.4488
Reel in	0.2	0.5277	-0.3335	0.1371	-0.1061	1.2744	-	-	-	-	-	-

TABLE 5.2: Identified parameters with least square

To validate those parameters a simulation should be run with those coefficients to see how close it ends up to the real measurements. Also one needs to be careful since the polynomial correlations given in equation (5.2) might actually not reflect the real relationship between those parameters. To overcome the latter concern, a system identification using deep learning was implemented. The choice of deep learning is explained by the fact that a deep neural network can identify highly non-linear laws between the parameters. The identification with deep learning was implemented as follow, the lift and drag coefficients were directly computed with the data and gave the objective data. Then as an input the neural network got the angles of attack, power setting and steering settings. The results were close to the ones presented here but this is still not conclusive. Indeed to be sure about those results one would need the measurements for the side slip angle and then verify the coefficients identified through deep learning or least square in a simulation.
However one can notice that the results shown in 5.24 and 5.25 have a physical meaning. Indeed the drag coefficients identified with this relation decrease between reel out and reel in and gets closer to the CFD curve when reeling in. Also regarding the side efforts in figure 5.25 the lift and drag coefficient increase when a turn is initiated. Indeed when turning left the steering setting u_s is increased positively and the left side lift and drag increase while the right side lift and drag decrease.

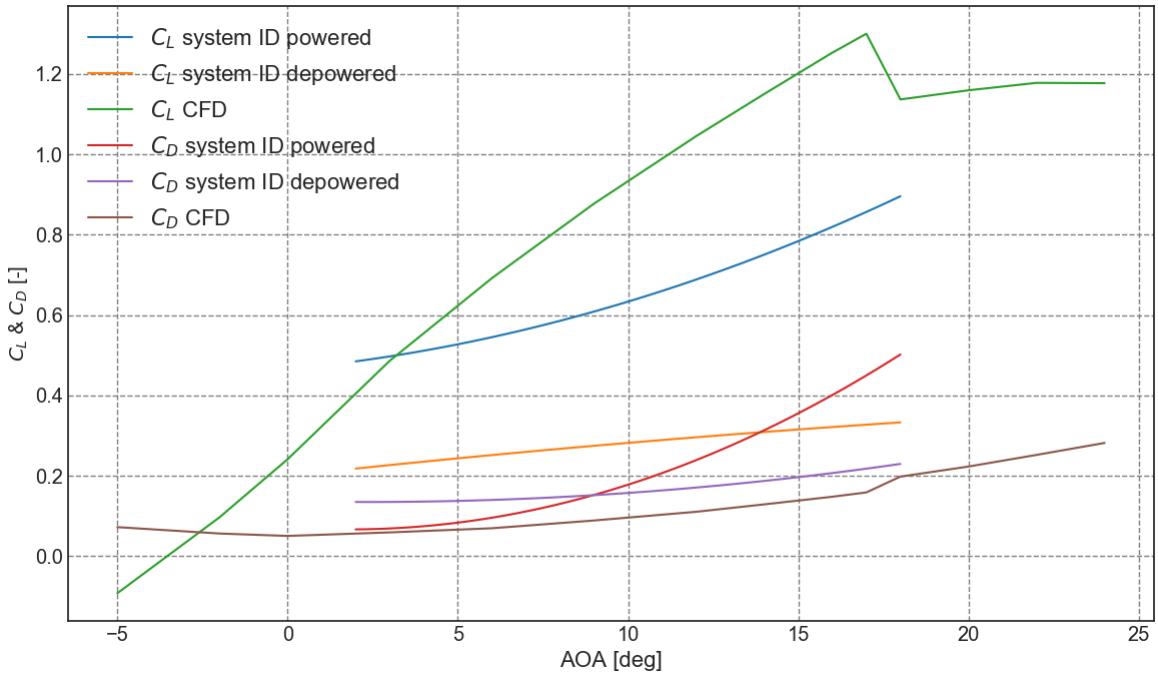

FIGURE 5.24: Total lift identified using least square between powered and depowered flights

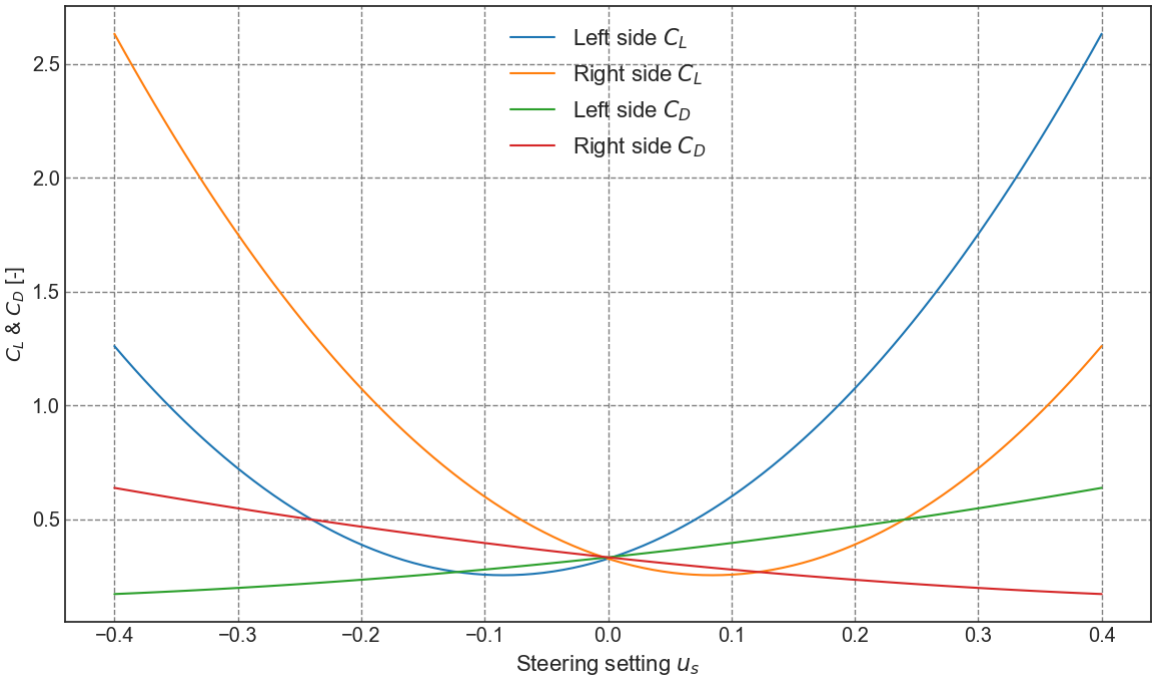

FIGURE 5.25: Side aerodynamic coefficients identified using least square

Chapter 6

Conclusion

First of all it was shown that the KCU does have an effect on the dynamics of the kite. Indeed the inertia of the KCU makes it swing outwards during at turn since the tether cannot withstand any bending moment. This roll makes it possible for the lift to balance the inertial. This explains most of the measured roll but some asymmetry in the behaviour was observed. One supposes that it comes from an uneven bridle line system or force distribution. This still must be proven since the model implemented was too simple and there are complex most probably complex interactions and efforts distribution happening in the bridle line system. In the end effect on the performance is negligible since only 1 to 2% of the lift goes into balancing this effort. This also shows how sensitive tethered systems are to side forces, since small efforts can cause deviations.

Then regarding the different efforts applying on the kite were quantified. The pulling aerodynamic force is the main one however for straight flight the drag of both tether and KCU when added up represent a significant share of the efforts, and given the previous conclusion might be the origin of rotations. During turns the inertial effects of both the tether and KCU also represent a non negligible share of the efforts.

A turning rate law was derived based on a inertial force balance. The results are corresponding well with the reality, it then seems that the side forces generated by the side of the kite's wing are then balancing the inertial forces of the kite. There is however a lag between the turning of the kite and the actual yawing of the kite. Several hypothesis were made about this subject ranging from a slack in the bridle line system to a settling and establishment characteristic time of the aerodynamic efforts and of the dynamic efforts after a turning input.

A comparison of the wing's aerodynamic coefficients C_L and C_D was made between a 3 plate aerodynamic model, Oehler's model and CFD results where a rigid wing hypothesis was used. Both experimental cases are off the CFD results in terms of variation of the coefficient with respect to the angle of attack. As shown the deformation of the kite due to an increase in the loads during reel out is responsible for this difference. Since the reinforcement of the canopy of the kite does not reach the front beam, a non negligible amount of deformation occurs in the junction of the canopy with the front beam changing the shape with respect to the CFD. The frontal area will increase and so will the drag, the shape will change and so will the lift and drag. The fact that the change of C_D with the angle of attack is closer to the CFD results for depower than for power confirms this hypothesis. The turning of a kite has an effect over its performance, it seems that the steering input increases the drag and decreases the lift. The actual decrease of performance is in the order of 5 %

Finally the tether orientation used for computation has an influence on the estimation of the aerodynamic parameters, even if the orientation angles at the end of the tether are small. It seems that using a more complex tether model gives an orientation to the tether tension such that it is oriented more vertically, increasing the force the lift has to balance. It was estimated that the polar angle θ was influenced by weight during a straight flight and is well estimated by a catenary model

.During a turn it was shown to be governed by drag and weight forces. About the ϕ polar angle, its behaviour in straight line is governed by drag mainly, and during a turn by inertia and drag. The final efforts lost in balancing tether weight inertia and drag decreases during a turn and increases during a flight and is on average of 5%. The reason is mainly that the increase in tether tension due to an increase in speed so aerodynamic force during turns is higher than the increase in drag and inertial force of the tether. The multi mass tether can be approximated with a straight tether model, however it will under estimate the drag effort in straight line and there will present a lag in effort delivery.

Appendix A

Code Appendix

A.1 Rotation matrix

```
def R_EG_Body(Roll,Pitch,Yaw):#!!In radians!!

    #Rotational matrix for Roll
    R_Roll=np.array([[1, 0, 0],
    [0,np.cos(Roll),np.sin(Roll)],
    [0,-np.sin(Roll),np.cos(Roll)]])

    #Rotational matrix for Pitch
    R_Pitch=np.array([[np.cos(Pitch),
     0, np.sin(Pitch)],[0,1,0],
     [-np.sin(Pitch), 0, np.cos(Pitch)]])

    #Rotational matrix for Roll
    R_Yaw= np.array([[np.cos(Yaw),-np.sin(Yaw),0],
    [np.sin(Yaw),np.cos(Yaw),0],
    [0,0,1]])

    #Total Rotational Matrix
    return R_Roll.dot(R_Pitch.dot(R_Yaw))
```

Listing A.1: Rotation matrix

A.2 Blender visualisation check

```
import bpy
import numpy as np
import pickle

#Be careful the object used has for a rotational reference frame and NED

#deletes all objects already present
#bpy.ops.object.delete(use_global=False)

#Structure of data:
#[time,elevation,azimuth,kite_distance,kite_roll,kite_yaw,kite_pitch,
    side_slip,AOA]
#[time_real,kite_elevation,kite_azimuth,kite_distance,kite_roll,kite_yaw,
    kite_pitch,side_slip,AOA]
[time,x,y,z,kite_roll,kite_yaw,kite_pitch,side_slip,AOA,kite_elevation,
    kite_azimuth,kite_distance]=pickle.load(open("C:/Users/Arthur/Documents/
    EPFL/Projet_Master/Code/Blender_Animation/data_blender_animation.pckl","rb
    "))

#Loading the pickle file of data
file_path='C://Users//Arthur//Documents//EPFL//Projet_Master//Code//
    Blender_Animation//Kite_3D_Model//model.stl'
```

```
17
18 #Smoothening function for the data usgin windowing functions
19 def smooth(x,window_len=11,window='hanning'):
20     if window_len<3:
21         return x
22     s=np.r_[x[window_len-1:0:-1],x,x[-2:-window_len-1:-1]]
23     if window == 'flat': #moving average
24         w=np.ones(window_len,'d')
25     else:
26         w=eval('np.'+window+'(window_len)')
27     y=np.convolve(w/w.sum(),s,mode='valid')
28     return y
29
30 #Definition of a function for a change of reference frame
31 def R_EG_Body(Pitch,Yaw):#!!In radians!!
32     #Rotational matrix for Pitch
33     R_Pitch=np.array([[np.cos(Pitch), 0, np.sin(Pitch)],[0,1,0],[-np.sin(
       Pitch), 0, np.cos(Pitch)]])
34
35     #Rotational matrix for Roll
36     R_Yaw= np.array([[np.cos(Yaw),-np.sin(Yaw),0],[np.sin(Yaw),np.cos(Yaw)
       ,0],[0,0,1]])
37
38     #Total Rotational Matrix
39     return R_Pitch.dot(R_Yaw)
40
41 #Import of the stl mesh of the kite
42 bpy.ops.import_mesh.stl(filepath=file_path)
43 ops=bpy.ops
44 ctx=bpy.context
45
46 # Variable for currently active object
47 myboj=bpy.context.object
48
49 #Choice of the starting and ending point as well as the total time of the
       flight
50
51 l=len(x)-116500
52 #start(which step should the visualization start?)
53 start=0
54 #end (which step should the visualization end?)
55 end=l
56 #step
57 step=4
58
59 #Tangent vector estimation
60 tx=np.diff(smooth(x,8,'hanning')[start:end:step])
61 ty=np.diff(smooth(y,8,'hanning')[start:end:step])
62 tz=np.diff(smooth(z,8,'hanning')[start:end:step])
63
64 #Position vectors
65 x=x[start:end:step]
66 y=y[start:end:step]
67 z=z[start:end:step]
68
69 x0=x[0]
70 y0=y[0]
71 z0=z[0]
72
73 #Conversion to radians of the measured data
74 kite_roll=kite_roll[start:end:step]/180*np.pi
75 kite_pitch=kite_pitch[start:end:step]/180*np.pi
76 kite_yaw=kite_yaw[start:end:step]/180*np.pi-90/180*np.pi
```

```
77
78 #computation of the estimated pitch yaw and roll from the tangential vector
       for verification and comparison
79 theta_0=np.arctan(y[0]/x[0])
80
81 theta=np.arctan2(tz,np.sqrt(tx*tx+ty*ty))
82 phi=np.arctan2(ty,tx)
83
84 theta_tether=np.arctan2(z,np.sqrt(x*x+y*y))
85 phi_tether=np.arctan2(y,x)
86
87
88
89 for i in range(0,l-5):
90     #Cration of the animation
91     bpy.ops.import_mesh.stl(filepath=file_path)
92     ops=bpy.ops
93     ctx=bpy.context
94
95     mat_name='Material'+str(i)
96     mat = bpy.data.materials.new(mat_name)
97     blue_color= (0.00812156, 0.0287431, 0.8, 1)
98     red_color= (0.8, 0.0240705, 0.0340232, 1)
99
100    #Choice of the color of the kite
101    mat.diffuse_color = blue_color
102
103    # Variable for currently active object
104    myboj=bpy.context.object
105    me = myboj.data
106    me.materials.append(mat)
107
108    #Orient the imported stl the right way: heading vetor = x-axis
109    ops.transform.rotate(value=-np.pi/2,orient_axis='Z',orient_type='LOCAL')#
       Set the kite into the right position and orientation
110
111    #1st the yawing motion
112    #Because of the reference frame of the stl file it is the z axis
113    #ops.transform.rotate(value=-phi[i+1],orient_axis='Z',orient_type='LOCAL
       ') #for the theoretical yaw angle
114    ops.transform.rotate(value=kite_yaw[i],orient_axis='Z',orient_type='LOCAL
       ') #for the measured yaw angle
115
116    #2nd the pitch motion
117    #Because of the reference frame of the stl file it is the x axis
118    #ops.transform.rotate(value=theta[i+1],orient_axis='X',orient_type='LOCAL
       ') #for the theoretical pitch angle
119    ops.transform.rotate(value=kite_pitch[i],orient_axis='X',orient_type='
       LOCAL') #for the measured pitch angle
120
121
122    #Projection into the body reference frame for aligning the kite with the
       ground station and finding the theoretical roll component
123    tether_position=np.array([np.cos(theta_tether[i])*np.cos(phi_tether[i]),
       np.cos(theta_tether[i])*np.sin(phi_tether[i]),np.sin(theta_tether[i])])
124    Transition_Matrix=R_EG_Body(theta[i+1],phi[i+1])
125    Projection=Transition_Matrix.dot(tether_position)
126    roll=np.arctan2(Projection[1],Projection[2])
127
128    #Rolling of the kite for aligning the kite with the ground station
129    #ops.transform.rotate(value=roll,orient_axis='Y',orient_type='LOCAL') #
       for the theoretical roll angle
```

```
130     ops.transform.rotate(value=kite_roll[i],orient_axis='Y',orient_type='
        LOCAL') # for the measured roll angle
131
132     #Translation
133     ops.transform.translate(value=(x[i],y[i],z[i]),orient_type='GLOBAL')
```

Listing A.2: Blender visualisation code

A.3 Angular velocity

```
1  #%%Angular velocity computation ind the object's reference frame
2  def Angular_Velocity(kite_roll,kite_pitch,kite_yaw,roll_rate,pitch_rate,
       yaw_rate):#Acthung: negative sign for pitch and yaw + think to convert the
        angles into radians
3
4      kite_roll=kite_roll*np.pi/180
5      kite_pitch=-kite_pitch*np.pi/180
6      kite_yaw=-(kite_yaw-90)/180*np.pi
7
8      #Computation of the angular speed vector
9      M=np.array([[1,0,-np.sin(kite_pitch)],[0,np.cos(kite_roll),np.cos(
       kite_pitch)*np.sin(kite_roll)],[0,-np.sin(kite_roll),np.cos(kite_pitch)*np
       .cos(kite_roll)]])
10     d=np.array([roll_rate,-pitch_rate,-yaw_rate])
11     return M.dot(d)
```

Listing A.3: Angular velocity computation

Bibliography

[1] I. Argatov, P. Rautakorpi, and R. Silvennoinen. "Apparent wind load effects on the tether of a kite power generator". In: *Journal of Wind Engineering and Industrial Aerodynamics* 99.10 (2011), pp. 1079 –1088. ISSN: 0167-6105. DOI: https://doi.org/10.1016/j.jweia.2011.07.010. URL: http://www.sciencedirect.com/science/article/pii/S0167610511001449.

[2] J.H. Baayen. *Modeling a kite on a variable length flexible tether*. Tech. rep. TU Delft, 2011.

[3] Nedeleg Bigi et al. "Analytical Tether Model for Static Kite Flight". In: Apr. 2018, pp. 57–78. ISBN: 978-981-10-1946-3. DOI: 10.1007/978-981-10-1947-0_3.

[4] Ricardo Borobia-Moreno et al. "Flight Path Reconstruction and Flight Test of Four-line Power Kites". In: (Feb. 2018).

[5] Allert Bosch et al. "Nonlinear Aeroelasticity, Flight Dynamics and Control of a Flexible Membrane Traction Kite". In: Sept. 2013, pp. 307–323. DOI: 10.1007/978-3-642-39965-7_17.

[6] Lukas Carl Braun. "Systematic Approach for a Redesign of a Kite Control Unit". MA thesis. TU Delft, 2015.

[7] Jeroen Breukels. "An Engineering Methodology for Kite Design." PhD thesis. TU Delft, 2011.

[8] Joeren Breukels. *Kite launch using an aerostat*. Tech. rep. Delft University of Technology, 2007.

[9] Patrick Demkowicz. "Numerical analysis of the flow past a leading edge inflatable kite wing using a correlation-based transition model". MA thesis. TU-Delft, 2019.

[10] Michael Erhard and Hans Strauch. "Control of Towing Kites for Seagoing Vessels." In: *IEEE Transactions on ControlSystemsTechnology,21(5)* (2012).

[11] Lorenzo Fagiano. "Contril of Tethered Airfoils for High-Altitude Wind Energy Generation". PhD thesis. Politecnico di Torino, 2009.

[12] Uwe Fechner and Roland Schmehl. "Flight Path Planning in a Turbulent Wind Environment". In: Apr. 2018, pp. 361–390. ISBN: 978-981-10-1946-3. DOI: 10.1007/978-981-10-1947-0_15.

[13] Uwe Fechner et al. "Dynamic Model of a Pumping Kite Power System". In: *Renewable Energy* (Sept. 2015). DOI: 10.1016/j.renene.2015.04.028.

[14] Xander Gerrman. "The effect of kite control unit mass and drag on the flight behavior of an airborne wind energy system kite". MA thesis. TU Delft, 2019.

[15] Sebastien Gros and Moritz Diehl. "Modeling of Airborne Wind Energy Systems in Natural Coordinates". In: *Green Energy and Technology* (Oct. 2013), pp. 181–203. DOI: 10.1007/978-3-642-39965-7_10.

[16] B. Houska and M. Diehl. "Optimal Control of Towing Kites". In: *Proceedings of the 45th IEEE Conference on Decision and Control*. 2006, pp. 2693–2697. DOI: 10.1109/CDC.2006.377210.

[17] Jan Hummel, Dietmar Göhlich, and Roland Schmehl. "Automatic measurement and characterization of the dynamic properties of tethered membrane wings". In: *Wind Energy Science* 4 (Jan. 2019), pp. 41–55. DOI: 10.5194/wes-4-41-2019.

[18] Thomas Jann and Michael B. Ward. "Combining Distributed Measurements of Air Data, IMU and GPS for Gliding Parachute Applications". In: *AIAA Aviation 2019 Forum*. DOI: 10.2514/6.2019-3283. eprint: https://arc.aiaa.org/doi/pdf/10.2514/6.2019-3283. URL: https://arc.aiaa.org/doi/abs/10.2514/6.2019-3283.

[19] M. Khammash L. Fagiano A.U. Zgraggen and M. Morari. "Automatic control of tethered wings for airborne wind energy: Design and experimental results". In: *2013 European Control Conference, ECC 2013, 22 (4):992–997,2013. ISSN07431619.* (2013).

[20] Johannes Oehler and Roland Schmehl. "Aerodynamic characterization of a soft kite by in situ flow measurement". In: 4 (July 2018), pp. 1–21. DOI: 10.5194/wes-4-1-2019.

[21] Benoit Python. "Methodology Improvement for Performance Assessment of Pumping Kite Power Wing". MA thesis. EPFL, 2017.

[22] Marc van Reijen. "The turning of kite - a quantification of known theories". MA thesis. TU Delft, 2018.

[23] M.B. Ruppert. "The turning of kites: A quantification of known theories". MA thesis. TU Delft, 2018.

[24] Roland Schmehl. *Airborne Wind Energy : Advances in Technology Development and Research*. eng. Green energy and technology. Singapore: Springer, 2018. ISBN: 978-981-10-1946-3.

[25] Roland SCHMEHL. "Frishce Brise - Serie Energie, Teil 2". In: *Spektrum der Wissenschaft* (2012).

[26] E. Schmidt et al. "In-Flight Estimation of the Aerodynamics of Tethered Wings for Airborne Wind Energy". In: *IEEE Transactions on Control Systems Technology* (2019), pp. 1–14. ISSN: 2374-0159. DOI: 10.1109/TCST.2019.2907663.

[27] E. J. Terink et al. "Flight Dynamics and Stability of a Tethered Inflatable Kiteplane". In: *Journal of Aircraft* 48.2 (2011), pp. 503–513. DOI: 10.2514/1.C031108. eprint: https://doi.org/10.2514/1.C031108. URL: https://doi.org/10.2514/1.C031108.

[28] Rolf van der Vlugt et al. "Quasi-steady model of a pumping kite power system". In: *Renewable Energy* 131 (2019), pp. 83 –99. ISSN: 0960-1481. DOI: https://doi.org/10.1016/j.renene.2018.07.023. URL: http://www.sciencedirect.com/science/article/pii/S0960148118308206.

[29] Paul Williams, Bas Lansdorp, and Wuboo Ockels. "Modeling and Control of a Kite on a Variable Length Flexible Inelastic Tether". In: *Collection of Technical Papers - 2007 AIAA Modeling and Simulation Technologies Conference* 2 (Aug. 2007). DOI: 10.2514/6.2007-6705.